HYBRID QUANTUM SYSTEMS: RESONATOR STATE PREPARATION WITH RYDBERG ATOM BEAMS

Robert Jirschik

Supervisor: Prof. Stephen Hogan

Co-supervisor: Prof. Sougato Bose

Department of Physics and Astronomy

University College London

20.05.2019

A dissertation submitted to **University College London**

for the degree of **Doctor of Philosophy**

Declaration

I, Robert Jirschik, confirm that the work presented in this thesis is my own. Where information has been derived from other sources, I confirm that this has been indicated in the thesis.

Date: . . . . . Signature: . . . . . .

Abstract

In this thesis theoretical studies of hybrid quantum systems composed of solid-state superconducting microwave resonators, mechanical oscillators, and gas-phase Rydberg atoms are described. The thesis begins with an overview of the current state of the field of hybrid quantum information processing. An introduction to the physics of Rydberg atoms and the preparation processes of circular Rydberg states follows, including a review of the associated literature. Three main new research results are then presented. These include (1) numerical studies of static electric dipole interactions in strongly polarized gases of Rydberg atoms. The understanding and characterization of these interactions is essential to maximize the quantum-state preparation procedures required for the hybrid systems studied in the thesis; (2) analytical and numerical studies of quantum-state preparation and cooling in coplanar superconducting microwave resonators using beams of atoms in circular Rydberg states; and (3) studies of coupled Rydberg-atom—mechanical-oscillator systems. The results presented in each of these areas are of interest for hybrid quantum information processing and quantum computation, and optical-to-microwave photon conversion for quantum communication.

Impact Statement

The research reported in this thesis is of interest in several research areas. Approaches to the preparation of quantum states of resonator systems in a controlled manner as presented here have applications in several quantum technologies. For example, the selective preparation of the vacuum state of the resonator can be used to increase the fidelity of quantum state transfer protocols and thus be applied in the context of quantum communication. The study of electrostatic dipole-dipole interactions within ensembles of Rydberg atoms described in this thesis further the understanding of many-body physics in strongly polarized gases. The combination of this study and the resonator state preparation results could lead to new quantum measurement techniques to characterize atomic ensembles, as well as the realization of quantum non-demolition measurements of gas-phase atoms and molecules, including exotic species such as antihydrogen and positronium. In the long term, the results presented here constitute a stepping stone in the development of a hybrid quantum information processing architecture with transmission-line microwave resonators controlled and manipulated using Rydberg atoms. This could lead to the development of new, robust quantum simulators for studying complex condensed matter problems that cannot be solved using classical computation technology.

Acknowledgements

There are too many people to thank for all the support I received during my time as a PhD student. I shall give it a try here.
First and foremost I would like to thank my supervisor, Prof. Stephen Hogan, for giving me the opportunity to work with him. His passion for science, his dedication, interest and enthusiasm with which he approaches his work all have been a great motivation for me. I could not have finished this thesis without his support, ideas, suggestions and discussions.
I would also like to thank my Co-supervisor, Prof. Sougato Bose, for his creative input and help. Another thank you to my Diplomarbeit-supervisor Prof. Michael Hartmann. My overwhelmingly positive experience during my research year changed my perspective on physics, and encouraged me to pursue a PhD.
A special thanks to my parents, Kathrin and Dirk, who have been encouraging me to follow my passions without a worry. They are amazing role models. I cannot thank them enough for their advice and moral support.
I would also like to thank a few PhD students and Postdocs who have passed through our office over the years, or with whom I had the pleasure of discussing our work: Hoda Hossein-Nejad, Patrick Lancuba, Edward O'Reilly, David Holdaway, Richard Stones, Valentina Zhelyazkova,

Valentina Notararigo, Stefan Siwiak-Jaszek, Adam Deller, James Palmer and Alex Morgan. My apologies to everyone else I have interacted with at UCL and did not mention here, your contributions are all appreciated.
And finally, a big thank you to all my close friends. It seems unfair to mention only some of them by name, but a special thank you to my closest friend Felix for his unrivaled reliability, and the two people with the biggest influence on me during my time in London, Renaud and Olivier. Without their distractions this endeavour would not have been even half as fun.

Contents

List of Figures

List of Tables

"He helps you to understand

He does everything he can

Doctor Robert"

- The Beatles

Chapter 1

Introduction

In recent years the development of quantum technologies has made considerable progress. The ability to control the quantum dynamics in experiments with atoms and trapped ions has been greatly enhanced and culminated in the award of the Nobel Prize in Physics to Serge Haroche and David J. Wineland in 2012 for their work in cavity quantum electrodynamics [47, 119]. In addition to this discipline within quantum optics, the development of superconducting quantum electrical circuits [124, 31, 113] in the last two decades and the proposal to, i.e., employ such systems as quantum simulators for light-matter interactions [12], has further been aiding the progress of the field of quantum information processing because of their scalability and control. Other systems have also been emerging as promising candidates as quantum bits for quantum information processing due to their long coherence times, such as ensembles of electron spins [120], nitrogen-vacancies (NV) in diamonds [7], and quantum dots in semiconductors [90]. Additionally, the use of micro- and nanomechanical oscillators, i.e., in the form of microtoroidal resonators, carbon

nanotubes or membranes, and the ability to reach the quantized regime of their mechanical motion have been offering new possibilities for tests of fundamental quantum physics [15, 74, 25], and for quantum information processing [96]. All of these individual quantum systems, that contain qubits and resonators, offer distinct advantages and disadvantages, as outlined in Table 1.1 and Table 1.2.

	$n = 70$ Rydberg atom	Optical Ion	Electronic spin ensembles	SC Transmon qubit
Energy gap f	~ 20 GHz	10^5 GHz – 10^6 GHz	$\sim 1 - 10$ GHz	$\sim 5 - 10$ GHz
Coherence time T_2	~ 600 μs	$\sim 1 - 35$ s	~ 1 ms $- 1$ s	$\sim 5 - 20$ μs
Coupling rate $g/2\pi$	~ 25 MHz	~ 10 kHz	~ 100 Hz – 1 MHz	~ 150 MHz

Table 1.1: Important properties for different systems that can be used as qubits [49, 57, 80, 81, 83, 121].

At present there is considerable interest in the development of hybrid approaches to quantum information processing.

These involve combining two or more distinct quantum systems, where, for example, one is being employed as the quantum memory, i.e. a quibit, and coupled to another quantum system, i.e. a resonator, to perform gate operations, in order to take advantage of the most favorable aspects of

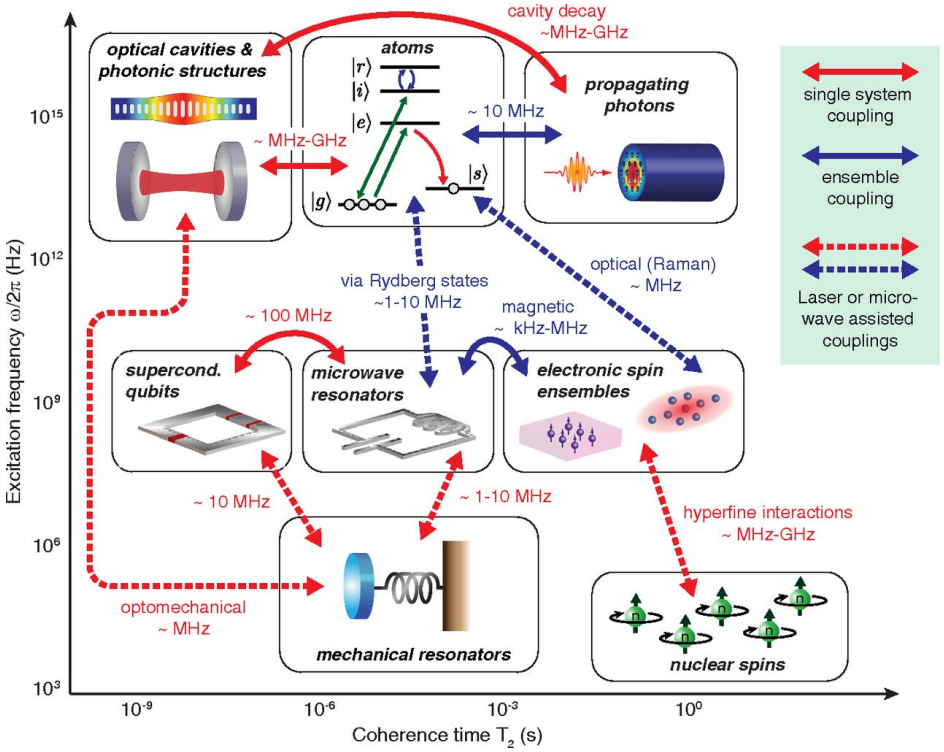

Figure 1.1: Overview of hybrid quantum systems. Each individual system is positioned according to its excitation frequency and coherence time, with possible couplings between them indicated by arrows. From [65].

each. These may include, for example, coherence times, scalability or the timescales on which states can be prepared or manipulated. Within the last decade, hybrid approaches to quantum information processing have been proposed and realized in various ways. One such proposal is the use of ensembles of cold polar molecules acting as a long-lived quantum memory coupled to a circuit QED setup consisting of a superconducting cooper pair box strongly coupled to a stripline resonator [94]. Another proposal is the magnetic coupling of a Bose-Einstein condensate of rubidium atoms to the nanomechanical motion of a cantilever [110]. Examples

for the experimental realization of strongly coupled hybrid quantum systems are the coupling of electron spin ensembles to a superconducting transmission-line [100] as well as the emergence of circuit quantum acoustodynamics where a superconducting qubit has been coupled to trapped on-chip acoustic wavepackets [76].

	Optical cavity	Coplanar waveguide resonator	Si Nanobeam Mechanical oscillator
Frequency range	$\sim 10^5$ GHz	$\sim 2 - 8$ GHz	~ 4 GHz
Coupling strength $g/2\pi$	~ 100 MHz	> 300 MHz	~ 1 MHz
Quality factor Q	$> 10^6$	$\sim 10^5 - 10^8$	$\sim 10^5$

Table 1.2: Important properties for different types of resonators [57, 42, 81, 63, 25].

In this context the work described in this thesis is related to the investigation of chip-based approaches to exploiting Rydberg atoms in hybrid quantum information processing [122, 98, 72, 89, 88]. The long-term objetives of this work are to coherently couple gas-phase atoms in highly excited Rydberg states to solid-state superconducting qubits. The coupling between the two systems will be mediated, resonantly or near-resonantly through coplanar superconducting microwave resonators. Because of the possibil-

ity of implementing fast quantum gates ($g/2\pi \approx 100$ MHz) when using superconducting qubits and the inherent scalability of chip-based structures [58], superconducting microwave circuits appear to be ideal solid-state candidates for the realization of quantum approaches to computation and simulation. However, superconducting qubits suffer from comparitively short coherence times ($\tau \approx 10$ μs). They are therefore not ideally suited as long coherence-time quantum memories. With this in mind efforts are being directed toward the development of hybrid approaches to quantum information processing in which rapid state manipulation could be performed in these solid-state circuits while a gas-phase sample of atoms, molecules or ions is used as a long coherence-time memory [94]. From this perspective, atoms in highly excited Rydberg states are well suited to act as the gas-phase component of such a hybrid system. Rydberg states can exhibit comparitively long coherence times (≈ 100 ms) and because of their large electric dipole moments for transitions at microwave frequencies they are compatible with coupling to microwave circuits. A realization of such a hybrid system would open up possibilities for several new applications such as long-coherence-time quantum memories [104], or enabling the coupling between optical and microwave photons [13] in a controllable medium for microwave-to-optical conversion [38]. Other possiblities include using Rydberg atoms coupled to superconducting circuits for photon number state preparation as has been done in large three-dimensional cavities [111], and long distance quantum entanglement distribution [27] in spatially separated quantum circuits coupled via transmission lines. In approaching the goal of strongly coupling gas-phase Rydberg atoms to

superconducting microwave circuits, a chip-based architecture for comprehensive control of the translational motion and internal quantum states of Rydberg atoms has recently been developed [66, 67, 51]. This architecture allows ensembles of Rydberg atoms to be accelerated, decelerated and transported in travelling electric traps located directly above coplanar electrode structures that are suitable for microwave transmission. The same electrode structures can act as coplanar microwave resonators and electrostatic traps for Rydberg atoms located above them [68].

In this thesis, theoretical studies are reported upon which those experimental developments will build. They include (1) studies of static electric dipole interactions within ensembles of Rydberg atoms which play an important role in the preservation of coherence over long timescales in these samples, (2) analysis of a scheme to use beams of Rydberg atoms to cool selected resonator modes, and (3) the extension of this cooling scheme to cool selected modes of other solid-state systems, such as nanomechanical oscillators.

In Chapter 2 the theoretical description of hydrogen atoms in Rydberg states and its extension to helium atoms is reviewed. Then, the properties of Rydberg atoms in circular states are discussed, the general method to prepare atoms in such circular states is reviewed, and extended to the preparation of helium atoms in circular Rydberg states. In Chapter 3 the role of static electric dipole-dipole interactions between helium Rydberg atoms, which lead to mean-field energy shifts in an atomic ensemble, is investigated. The general quantization procedure of superconducting transmission line resonators is then discussed in Chapter 4, and the open

quantum systems approach to quantifying the dissipation within these architectures when coupled to a thermal bath such as a coplanar waveguide used for measurements is then outlined. Chapter 5 deals with the general theory of quantum reservoir engineering and how it is applied to a beam of Rydberg atoms interacting with a transmission line resonator. Within this context an original cooling scheme for hybrid quantum systems with Rydberg atoms is presented and an analytic solution is given for the diagonal elements of the resonator density matrix. Chapter 6 improves upon this idea by introducing a numerical method that provides an even more effective cooling mechanism as well as more insights due to the calculation of the full density matrix of the resonator. Chapter 7 introduces an additional hybrid quantum system including a nanomechanical oscillator, whose quantum states are controlled via quantum reservoir engineering by an atomic beam. Finally, in Chapter 8 open problems and the outlook of this research are discussed.

Chapter 2

Rydberg Atoms

Rydberg atoms are atoms excited to states with very high principal quantum number n. They have been of importance in the derivation of Bohr's quantum mechanical orbital model of the electronic structure of atoms, and have played a key role in the development of quantum optics, quantum information and many-body physics due to the possibility of realizing strong electric dipole coupling to single microwave photons [18] and strong dipole-dipole interactions [6] between pairs of Rydberg atoms. In this chapter some of the properties of Rydberg atoms, and methods of Rydberg state preparation relevant to the topic of this thesis are described.

2.1 Hydrogen atoms in Rydberg States

The simplest atoms to be theoretically described are the hydrogen and hydrogen-like atoms. These are two-particle quantum systems, which can be approximately described as consisting of a positively charged nucleus and one electron. The electrostatic interaction between these two particles

is expressed by the Coloumb potential

$$V(r) = -\frac{Ze^2}{4\pi\epsilon_0 r}, \tag{2.1}$$

where the charge of the nucleus is Ze, e is the charge of the electron, ϵ_0 is the electric permittivity of the vacuum, and r is the distance between the electron and the nucleus. The wavefunction of the electron Ψ can be described via the Schrödinger equation [28]

$$\left(-\frac{\hbar^2}{2\mu}\nabla^2 - \frac{Ze^2}{4\pi\epsilon_0 r}\right)\Psi = E\Psi, \tag{2.2}$$

where $\hbar$ is the reduced Planck constant, and $\mu = \frac{m_e M}{m_e + M}$ is the reduced mass of the electron-nucleus system with m_e and M being the mass of the electron and nucleus, respectively. The energy of the electronic eigenstates is denoted by E. Switching from Cartesian coordinates (x, y, z) to spherical coordinates

$$r = \sqrt{x^2 + y^2 + z^2}, \tag{2.3}$$

$$\theta = \arccos\frac{z}{r}, \tag{2.4}$$

$$\phi = \arctan\frac{y}{x}, \tag{2.5}$$

Eq.(2.2) can be seperated[1] into radial and angular components. Hence, the wavefunction is factorizable as [11]

$$\Psi(r, \theta, \phi) = R(r) \cdot Y(\theta, \phi). \tag{2.6}$$

If both the radial and angular parts of the Schrödinger equation are equal but with opposite signs, they cancel each other, leading to a nontrivial

[1]The Laplace operator transforms as $\nabla^2 = \frac{1}{r^2}\frac{\partial}{\partial r}\left(r^2\frac{\partial}{\partial r}\right) + \frac{1}{r^2\sin\theta}\frac{\partial}{\partial\theta}\left(\sin\theta\frac{\partial}{\partial\theta}\right) + \frac{1}{r^2\sin^2\theta}\frac{\partial^2}{\partial\varphi^2}$

solution. By defining this separation constant [45] as $\ell(\ell+1)$, two self-consistent eigensystems follow:

- Angular equation

$$\left[\frac{1}{Y(\theta,\phi)\sin\theta}\frac{\partial}{\partial\theta}\left(\sin\theta\frac{\partial}{\partial\theta}\right)+\frac{1}{Y(\theta,\phi)\sin^2\theta}\frac{\partial^2}{\partial\phi^2}\right]Y(\theta,\phi)=-\ell(\ell+1). \tag{2.7}$$

  The solutions to this equation are the fatorizable normalized spherical harmonic functions $Y_{\ell,m}(\theta,\phi) = f_{\ell,m}(\theta)g_m(\phi)$, where the azimuthal quantum number m is introduced as another separation constant analogous to the factorization of the electron wavefuntion above. The generating function for the spherical harmonics is

$$\begin{aligned} Y_{\ell,m}(\theta,\phi) &= (-1)^m\sqrt{\frac{(2\ell+1)(\ell-m)!}{4\pi(\ell+m)!}}P_{\ell,m}(\cos\theta)e^{im\phi} \\ &= Y^*_{\ell,-m}(\theta,\phi), \end{aligned} \tag{2.8}$$

  with $m \geq 0$, and where $P_{\ell,m}(\cos\theta)$ are the associated Legendre polynomials.

- Radial equation

$$\left[\frac{d}{dr}\left(r^2\frac{d}{dr}\right)+\frac{2\mu r^2}{\hbar^2}\left(E+\frac{Ze^2}{4\pi\epsilon_0 r}\right)-\ell(\ell+1)\right]R(r)=0. \tag{2.9}$$

  By substituting $y(r) = rR(r)$, one arrives at a form of a well known equation whose orthonormal set of analytical solutions is related to the associated Laguerre functions $L^a_b(x)$. The solution for the eigenstates is [44]

$$R_{n,\ell}(r) = \sqrt{\left(\frac{2Z\mu}{nm_e a_0}\right)^3\frac{(n-\ell-1)!}{2n[(n+\ell)!]^3}}e^{-\frac{Z\mu r}{nm_e a_0}}\left(\frac{2Z\mu r}{nm_e a_0}\right)^\ell L^{2\ell+1}_{n-\ell-1}\left(\frac{2Z\mu r}{nm_e a_0}\right) \tag{2.10}$$

where $a_0 = 4\pi\epsilon_0\hbar^2/(m_e e^2)$ is the Bohr radius and the bound states are categorized by the principal quantum number $n = 1, 2, 3, \ldots$ and the angular momentum quantum number $0 \leq \ell \leq n - 1$.

The eigenenergies follow from the solution to the radial equation and give the Rydberg formula

$$E_n = -\frac{R_{hc}}{n^2} = \frac{-13.6 \text{ eV}}{n^2} \tag{2.11}$$

where the Rydberg constant for an electron bound to an infinitely heavy positive point charge can be expressed in terms of the fundamental constants

$$R_{hc} = \frac{Z^2 e^4 m_e}{16\pi^2\epsilon_0^2\hbar^2} = \frac{Z^2\hbar^2}{a_0^2 m_e} \tag{2.12}$$

Several properties of low-ℓ Rydberg states follow from this treatment of the structure of the hydrogen atom. Especially interesting are the scaling laws of the atomic properties with the principal quantum number n. For higher Rydberg states, i.e., large n, the binding energy of the electron decreases with n^{-2}. The energy difference between adjacent eigenstates decreases by n^{-3}. Hence, the radiative lifetime of such transitions increases with n^3. The large electric dipole transition moments, $\vec{p}$, for transitions where $\Delta n = n' - n = \pm 1$, scale as $p \propto \langle n'\ell'|e \cdot \hat{z}|n\ell\rangle \propto n^2$. This is a consequence of the large orbital radius of Rydberg states, which scales with n^2. All these properties mean that atoms in high-n Rydberg states are well suited to applications in quantum information processing [36].

2.2 Helium atoms in Rydberg states

For helium atoms where one electron is excited to a high energy state the Rydberg formula Eq. (2.11) needs to be adjusted by introducing the quantum defect $\delta_{n\ell}$. This empirical parameter accounts for the fact that the electron excited to a Rydberg state interacts with what can be viewed as an ion core whose nuclear charge is screened by the surrounding second electron, as can be seen in Fig. 2.1. Consequently, the Coloumb potential of the ion core is perturbed as it is no longer spherically symmetric. It is also possible that the inner electron is polarized by the outer electron in the Rydberg state. Therefore, the difference in binding energy for the hydrogen case can be accounted for by replacing the principal quantum number n by an effective quantum number [36] $n^* = n - \delta_{n\ell}$. The adjusted Rydberg formula for helium is

$$E_n = -\frac{R_{\mathrm{He}}\, hc}{(n - \delta_{n\ell})^2} \tag{2.13}$$

where $R_{\mathrm{He}} = \frac{R_\infty \mu_{\mathrm{He}}}{m_e}$ is the Rydberg constant for the helium atom. As can be inferred from Fig. (2.2), the deviation from our model of the ion core and the inner electron as one composite ion core with charge $Z = +1$ is bigger for the outer electron in Rydberg states closer to the positive core. Thus, the quantum defect, $\delta_{n\ell}$, decreases for Rydberg states with higher quantum numbers n and ℓ.

2.3 Atoms in Circular Rydberg States

Rydberg states which are of particular interest as qubit states in hybrid cavity QED are those which possess maximum angular momentum and

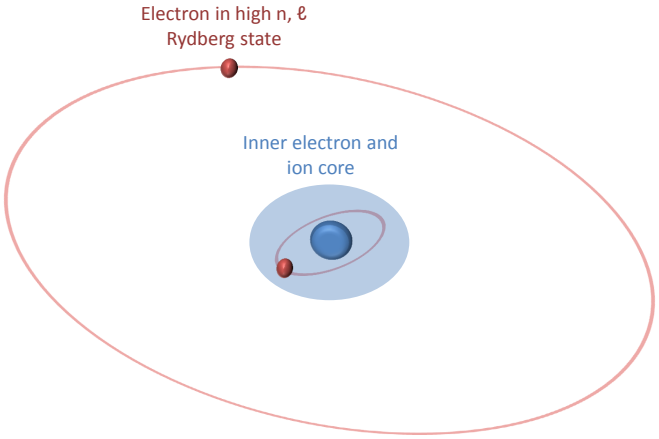

Figure 2.1: The helium atom in a high n Rydberg state. The outer electron "sees" the ion core and inner electron as one central field with charge $Z = +1$. The Coloumb potential associated with the He^{2+} nucleus is screened by the inner electron.

magnetic quantum numbers ℓ and m_ℓ, respectively, for a particular value of n. Such states are called circular Rydberg states and exhibit unique properties. The first of these are their long radiative lifetimes. Since the Einstein A coefficients describing the transition rate from an initial state i to a final state f, i.e., the decay rate of an excited state, can be written as a sum of the Einstein A coefficients of the decay into all possible final states. The lifetime of the excited state is then the inverse of this decay rate, and

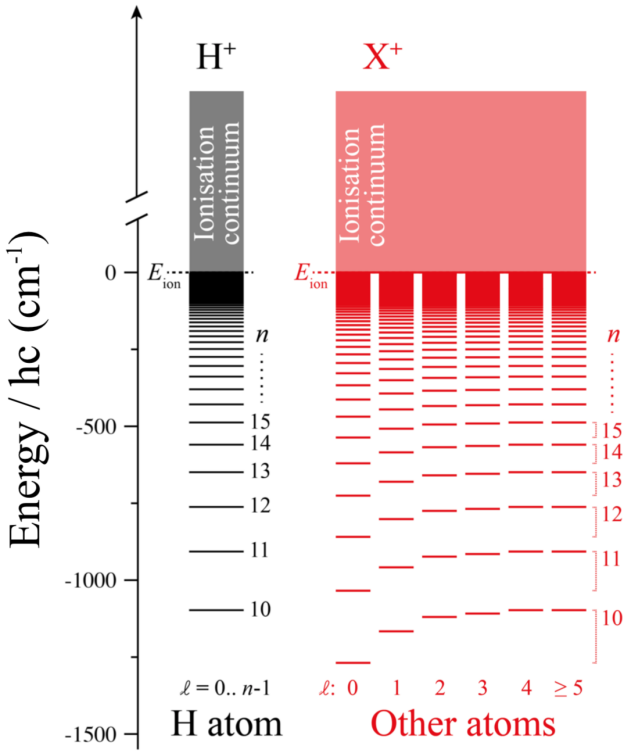

Figure 2.2: The effect of the quantum defects $\delta_{n,\ell}$ on the binding energy of the atomic states for non-hydrogenic atoms compared to the hydrogen atom. From [53].

thus

$$\tau = \frac{1}{\sum_f A_{fi}} = \left(\sum_f \frac{2\omega_{if}^3}{3\epsilon_0 \hbar c^3} \frac{\ell_{\max}}{2\ell_i + 1} |\vec{p}_{fi}|^2 \right)^{-1}, \tag{2.14}$$

where A_{fi} is proportional to the cube of the energy (frequency) difference between the initial and final states, and the square of the transition dipole moment [33].

In the case of circular Rydberg states, the excited state has $\ell = m_\ell = n - 1$. Due to the electric dipole selection rules allowing up to first order only transitions satisfying $\ell' = \ell - 1$ and $m'_\ell = m_\ell$ or $m'_\ell = m_\ell \pm 1$, it follows that

decay can only occur to final states $\ell' = n - 2$. Consequently, the initial excited circular state can only decay to one unique final state, $n' = n - 1$, $\ell' = n - 2$, $|m'_\ell| = |m_\ell| - 1$. Therefore, circular Rydberg states are a very good approximation to 2-level systems. Within the dipole approximation this quasi two-level characterization only breaks down on long timescales since the lower $n' = n - 1$ circular state can itself decay to the next higher-lying circular state with $n'' = n - 2$. However, in an electromagnetic environment that is appropriately engineered such that no vacuum mode exists at the frequency of the $n - 1 \rightarrow n - 2$ circular-state to circular-state transition, this additional decay channel can be eliminated [59]. The transition energy between the two states making up the quasi two-level system is $E_{n,n-1} \propto n^{-3}$, while their electron dipole transition moment scales as $\langle n-1, n-2|\vec{r}|n, n-1\rangle \sim n^2$. Therefore, it follows for the radiative lifetime of circular Rydberg states

$$\tau_{fi} \propto \frac{1}{(n^{-3})^3 (n^2)^2} = n^5. \tag{2.15}$$

Hence, circular Rydberg states exhibit greatly enhanced radiative lifetimes compared to low-ℓ states with the same values of n. The properties discussed above are listed in Tab. (2.1) for two examples of Rydberg states of Helium, showing an increased fluorescence lifetime in the case of circular Rydberg states when compared to states with low orbital angular momentum.

Circular Rydberg states cannot be directly photoexcited from an atomic ground state because of the selection rules for electric dipole transitions. However, two methods have been developed and implemented experi-

	$30\ ^3$S	$30\ ^3(L=29)$	$60\ ^3$S	$60\ ^3(L=59)$
$\|1\rangle$	$\|n=30, l=0, m=0\rangle$	$\|n=30, l=29, m=29\rangle$	$\|n=60, l=0, m=0\rangle$	$\|n=60, l=59, m=59\rangle$
$\|2\rangle$	$\|n=30, l=1, m=1\rangle$	$\|n=31, l=30, m=30\rangle$	$\|n=60, l=1, m=1\rangle$	$\|n=61, l=60, m=60\rangle$
Ionization energy / h	3728 GHz	3655 GHz	923 GHz	914 GHz
Transition frequency	57 GHz	232 GHz	7 GHz	30 GHz
Fluorescence lifetime	21 μs	2.2 ms	168 μs	71 ms
Transition dipole moment $\langle 2\|\hat{\mu}\|1\rangle$	729 ea_0	641 ea_0	2924 ea_0	2556 ea_0

Table 2.1: Comparison between some of the properties of low- and high-angular-momentum Rydberg states.

mentally to prepare them. The first of these involves adiabatic microwave transfer from an initially laser photoexcited low-ℓ (low-m_ℓ) Rydberg state with the absorption of approximately n microwave photons [60, 69].

The second method to produce circular Rydberg states is known as the crossed-fields method, and was first proposed by Delande and Gay [29]. By applying a constant magnetic field crossed perpendicularly with an adjustable electric field, one is able to very efficiently prepare atoms in circular Rydberg states by laser photoexcitation to appropppriate ℓ- and m_ℓ-mixed states which then evolve into circular states when the electric field strength is adiabatically reduced towards zero. The Hamiltonian associated with a single Rydberg electron in weak crossed electric $\vec{F} = (F_x, 0, 0)$ and magnetic $\vec{B} = (0, 0, B_z)$ fields can be written in atomic units to first order as

$$\mathcal{H} = \underbrace{-\frac{p^2}{2} - \frac{1}{r}}_{\mathcal{H}_c} + \underbrace{\frac{B_z\, m_\ell}{2} + F_x\, x}_{W}, \tag{2.16}$$

where $\mathcal{H}_c$ is the Coulomb-interaction Hamiltonian and W the pertubation due to the applied fields. The crossed-fields approach to the preparation of

circular states is based on the SO(4) symmetry of the Coulomb interaction, $\mathcal{H}_c$, with the generators Ł$_{ij}$ [87], where

$$\begin{aligned} \text{Ł}_{ij} &= \varepsilon_{ijk} \cdot L_k, \\ \text{Ł}_{i4} &= A_i. \end{aligned} \tag{2.17}$$

Here ε_{ijk} is the fully antisymmetric tensor, $\vec{L}$ is the angular momentum vector and $\vec{A}$ is the Runge-Lenz vector. One suitable choice of eigenbasis for this Hamiltonian is the subgroup chain SO(4) $\supset$ SO(3)$_\lambda$ $\supset$ SO(2)$_m$, which preserves the rotational invariance in real space. Their associated eigenfunctions $\left(\vec{\lambda}\right)^2$ and λ_z, derived from the operator $\vec{\lambda} = (\text{Ł}_{14}, \text{Ł}_{24}, \text{Ł}_{12})$, are solutions to the Coulomb problem. The corresponding energy eigenvalues of the hydrogen atom in atomic units are

$$E_n^{(0)} = -\frac{1}{2n^2} \tag{2.18}$$

The perturbation due to the applied fields W can be diagonalized for each n atomic shell. After replacing the operator $x = -(3/2)n \cdot A_x$ [87], one obtains

$$\begin{aligned} W_n &= \omega_\text{L} L_z + \omega_\text{S} A_x \\ &= \sqrt{\omega_\text{L}^2 + \omega_\text{S}^2}\,\vec{\lambda} \cdot \vec{u}, \end{aligned} \tag{2.19}$$

Here $\omega_\text{L} = B_z m_\ell/2$ and $\omega_\text{S} = (-3/2)nF_x$ are the Larmor and Stark frequencies in atomic units, and $\vec{u} = (\sin\alpha, 0, \cos\alpha)$ can be interpreted as a rotation of the operator $\vec{\lambda}$ in the xz-plane by the angle $\alpha = \tan^{-1}(\omega_\text{S}/\omega_\text{L})$.

From Eq. (2.18) and Eq. (2.19) it can be seen that the eigenfunctions of $\mathcal{H}_c$, $(\vec{\lambda})^2$, and W commute, so they can be chosen as the eigenfunctions of the total Hamiltonian, whose eigenenergies are

$$E_n = -\frac{1}{2n^2} + k\sqrt{\omega_\text{L}^2 + \omega_\text{S}^2}, \tag{2.20}$$

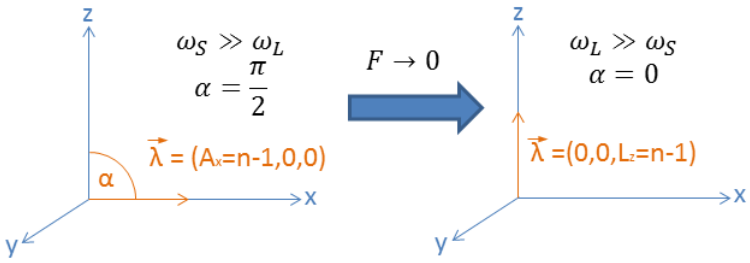

Figure 2.3: Adiabatically switching off the electric field, $\vec{F}$, leads to a rotation of the vector operator $\vec{\lambda}$. This is equivalent to the evolution of the upper state's parabolic ellipse, with angular momentum $m = 0$, to a circular trajectory with $m = L_z = n - 1$.

where k is the eigenvalue of the $(\lambda \cdot \vec{u})$-operator. Circular Rydberg states can therefore be prepared by starting out in the Stark limit $\omega_S \gg \omega_L$, optically exciting the outermost Stark state with maximum eccentricity $k_{\max} = n - 1 = \lambda_x = A_x$, as illustrated in Fig. (2.3). This is possible because the projection of the angular momentum vector in the direction of the applied electric field is $L_x = 0 = m$. In this case the vector $\vec{\lambda}$ is directed along the x-axis (electric field axis), because $\alpha \approx \frac{\pi}{2}$, which is the angle between the z-axis and $\vec{\lambda}$. By slowly switching off the electric field, the system evolves adiabatically to the limit in which $\omega_L \gg \omega_S$, i.e., $\alpha \approx 0$, and a circular Rydberg state $\lambda = L_z = n - 1 = m_{\max}$, while remaining in the upper sublevel, $k_{\max} = n - 1$, because the magnitude of the vector operator $|\vec{\lambda} = n - 1\rangle$ is conserved since the upper sublevel is a coherent state of the $SO(3)_\lambda$ subgroup.

Using this crossed-fields method a circular Rydberg state results, as the electron evolves into the state with $|k_{\max}, m_{\max}\rangle$. Even though this method is described here for the case of the hydrogen atom, as long as the upper

state $L_x = 0$ can be selectively prepared by either laser photoexcitation from the ground state or by optical-microwave double resonance methods, it can be used to efficiently produce circular Rydberg states of any atomic species, such as helium [127]. It has also been applied in the preparation of Rydberg states in hydrogen [73], rubidium [16], cesium [59], and other atoms [82, 26, 5].

2.3.1 Helium Atoms in Circular Rydberg States

Helium atoms are well suited to hybrid quantum information processing with Rydberg atoms and transmission line resonators because of their low adsorption rates onto cryogenic chip surfaces which in turn minimizes the build-up of time-varying stray electric fields [109]. In these experiments it is desirable to operate the superconducting circuits at frequencies below ~20 GHz. At such frequencies resonators with higher quality factors can be realized. To achieve this therefore requires atoms in circular Rydberg states with $n \geq 70$. However, the preparation of circular Rydberg states with these high values of n is particular challenging due to the high sensitivity of the photoexcitation phase of the crossed-fields method to stray electric fields. For non-hydrogenic atoms such as helium the standard approach to circular state preparation using the crossed-fields method is to initially excite the outermost positively shifted Stark state with $m_\ell = 0$, with respect to the electron field quantization axis, at the first avoided crossing of this state with a low-ℓ state at the Inglis-Teller limit. The advantage of this approach is that at this avoided crossing the target outer Stark state can possess a significant fraction of the character of the low-ℓ state, mak-

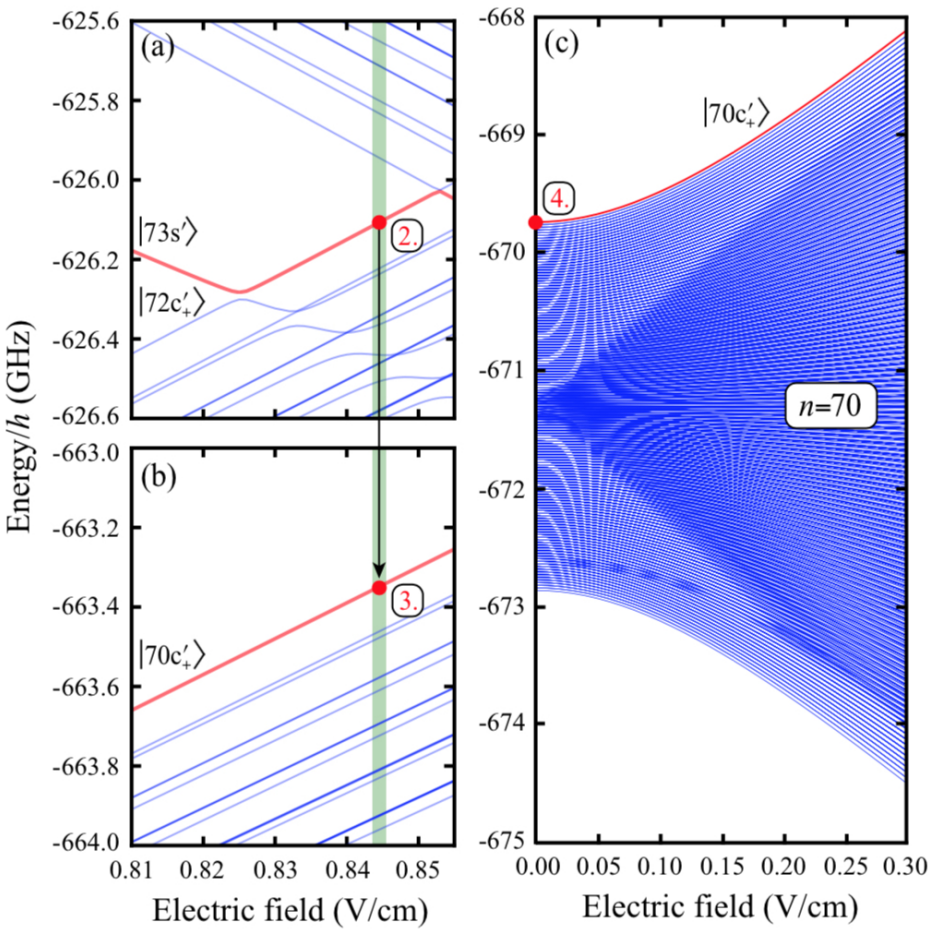

Figure 2.4: The energy level diagrams for steps 2-4 in the preparation process of circular Rydberg states for $n = 70$ in Helium as described in the text. From [80].

ing laser photoexcitation more efficient. However, for high values of n, the avoided crossings of these sublevels can be so small that the transitions to the individual states are not resolvable during the laser photoexcitation. To overcome this problem, the usual crossed-fields method, introduced in the previous section, can be modified [80].

Regarding notation, the circular states for specific values of n are denoted

here by $|nc_{\pm}\rangle$ for values of $m_\ell = \pm(n-1)$. To prepare the helium atoms in high-n circular Rydberg states, e.g. the $|70c_{+}\rangle$ circular state, a resonant two-photon laser excitation via an intermediate level is first performed in a weak electric field to transfer atoms from the metastable triplet $|2s\rangle$ state to the $|73s\rangle$ Rydberg state. In the second step of the process illustrated in Fig. (2.4) the electric field strength is adiabatically increased to polarize the $|73s'\rangle$ atoms, where the prime indicates an ℓ-mixed Stark state with in a nonzero electric field, such that they have a static electric dipole moment of similar magnitude and orientation as the target outer Stark state with $n = 70$, i.e., the $|70c'_{+}\rangle$ state. This is achieved in a field just beyond the first avoided crossing of the $|73s\rangle$ state in the Stark map of the triplet Rydberg states of He. Due to the large overlap of the wavefunctions of this state and the $|70c'_{+}\rangle$ state, the corresponding large electric dipole transition moment allows for fast and efficient population transfer to the $|70c'_{+}\rangle$ state by applying a resonant microwave pulse. Once the $|70c'_{+}\rangle$ state has been prepared, the fourth and last step of the circular state preparation process is to slowly reduce the electric field strength so that the atoms evolve adiabatically in the presence of the magnetic field into the final $|70c_{+}\rangle$ circular state. The transition between the $|70c_{+}\rangle$ and $|71c_{+}\rangle$ circular Rydberg states possesses an electric dipole transition moment of $3477ea_0$, allowing for single photon coupling strengths on the order of $g/(2\pi) \approx 5\,\text{MHz}$ [80] to two-dimensional superconducting microwave resonators.

Circular states, such as these, are particularly well suited for hybrid cavity QED because they possess long coherence times ($\sim$ 100 ms), low sensitivity to stray electric fields and possess large electric dipole transition

moments and transition frequencies in the microwave regime. Therefore, in the theoretical studies of involving Rydberg-atom–resonator coupling in Chapters 5, 6 and 7 of this thesis, the interaction of these high-n circular Rydberg states will be considered.

Chapter 3

Electrostatic Dipole Interactions in Polarized Rydberg Gases

The preparation of circular Rydberg states using the crossed fields method described in Chapter 2 requires the initial laser photoexcitation of Rydberg states with strong linear Stark shifts, and hence large static electric dipole moments. These states are then adiabatically converted into circular states in a zero electric field. To achieve quantum-state–selective preparation of a large number of circular Rydberg atoms the applied fields must be carefully controlled and interactions between the excited atoms in each phase of the preparation process must be minimized. When the circular preparation process is complete the dominant type of interaction between pairs of excited atoms is the van der Waals interaction that scales with R^{-6}, where R is the distance between the atoms. However, the large static electric dipole moments of the Rydberg-Stark states initially laser photoexcited interact through the stronger static electric dipole-dipole interactions, which depend on R^{-3}. A wide range of studies, both theoretical and experimen-

tal, have been carried out on van der Waals and resonant dipole-dipole interactions between Rydberg atoms [35, 9, 34]. These interactions, and the associated excitation blockade mechanisms, are exploited in, e.g., the entanglement of pairs of atoms [91, 118], and in applications of Rydberg atoms in quantum simulation [61, 79]. However, there has been little comparable study on the large static electric dipole interactions relevant to the circular state preparation processes discussed in Chapter 2. For this reason, and with the aim of elucidating the role of such interactions in Rydberg-Stark deceleration and trapping experiments, described in this chapter are the results of experiments and calculations of effects of static electric dipole interactions in dense gases of strongly polarized helium Rydberg atoms. The work described in this chapter was published in Zhelyazkova, Jirschik, and Hogan, *Physical Review A* 94.5: 053418 (2016) [128]. The text here follows closely the content of the published article, with adaptations to fit the structure of this thesis. The experiments described in Sections 3.1 and 3.2 were performed by Dr. Valentina Zhelyazkova while I carried out the calculations described in Section 3.3. Dr. Valentina Zhelyazkova and I both contributed to the preparation of the text of the published article.

The static electric dipole moments of Rydberg atoms and molecules can exceed 10000 D for states with values of $n \geq 50$ and scale with n^2. These dipole moments give rise to strong linear Stark shifts in external electric fields [36], and allow for control of the translational motion of a wide range of neutral atoms and molecules [54], composed of matter [123, 114, 52, 55] and antimatter [30], using inhomogeneous electric fields. When prepared

in states with these large dipole moments, gases of Rydberg atoms can also exhibit strong electrostatic dipole-dipole interactions [37, 125, 117]. These inter-particle interactions cause energy shifts of the Rydberg states, and, as demonstrated here, can modify the dielectric properties of the gases. The observation, and spectroscopic characterization, of the effects of these electrostatic interactions opens opportunities for using beams of Rydberg atoms or molecules as model systems with which to study many-body processes [23], including, e.g., resonant energy transfer [103], or surface ionization [50, 70, 40]. It is also of importance in the elucidation of effects of dipole interactions in Rydberg-Stark deceleration and trapping experiments [101], in experiments involving long-range Rydberg molecules [43, 10] possessing large static electric dipole moments [14], and in applications of Rydberg states as microscopic antennas for the detection of low-frequency electric fields [125, 78].

Microwave spectroscopy of the effects of van der Waals interactions [95, 86, 106], and resonant dipole-dipole interactions [2, 85] in cold Rydberg gases have been reported previously and provided important insights into these interacting few-particle systems. The electrostatic interactions that occur between Rydberg atoms in the outermost Stark states with the largest electric dipole moments, $\mu_{\rm max} \simeq (3/2)n^2 e a_0$, represent the extreme case of the dipole-dipole interaction for each value of n. The interaction potential, $V_{\rm dd}$, between a pair of atoms with electric dipole moments, $\mu_1 = |\vec{\mu}_1|$ and $\mu_2 = |\vec{\mu}_2|$, aligned with an electric field, $\vec{F}$, can be expressed as [37]

$$V_{\rm dd} \;=\; \frac{\mu_1\mu_2}{4\pi\epsilon_0 R^3}\left(1-3\cos^2\theta\right), \tag{3.1}$$

where $R = |\vec{R}|$ is the inter-atomic distance, θ is the angle between $\vec{R}$ and $\vec{F}$,

and ϵ_0 is the vacuum permittivity. For an isotropic, aligned ensemble of dipoles the average interaction energy is non zero, and leads to mean-field energy-level shifts within the ensemble.

The microwave spectroscopic studies reported here represent a direct measurement of these mean-field shifts in gases of helium (He) excited to Rydberg states with $n = 70$ and electric dipole moments up to $\mu_1 = \mu_{70} = 12\,250$ D. In the highest density regions of these gases, the dielectric properties differ from those in free space and give rise to changes in the microwave spectra which reflect the emergence of macroscopic electrical properties of the medium. This work is complimentary to recent studies of effects of electrostatic dipole interactions on particle motion in laser cooled samples of rubidium [108], and observations of optical bistability arising from mean-field shifts in gases of Rydberg atoms interacting via resonant dipole interactions [22].

3.1 Experiment

The experiments were performed in pulsed supersonic beams of metastable helium. The He atoms in these beams had a mean longitudinal speed of ~ 2000 m s^{-1} with a spread of ± 50 m s^{-1} [126]. The atoms were prepared in the metastable 1s2s ^{3}S$_1$ level in an electric discharge at the exit of a pulsed valve. This valve has operated at a repetition rate of 50 Hz [46]. After collimation by a 2 mm diameter skimmer and the deflection of stray ions produced in the discharge, the beam entered between a parallel pair of 70 mm $\times$ 70 mm copper electrodes. The electrodes were separated by 8.4 mm in the z dimension, as indicated in Fig. 3.1(a). At the mid-point between

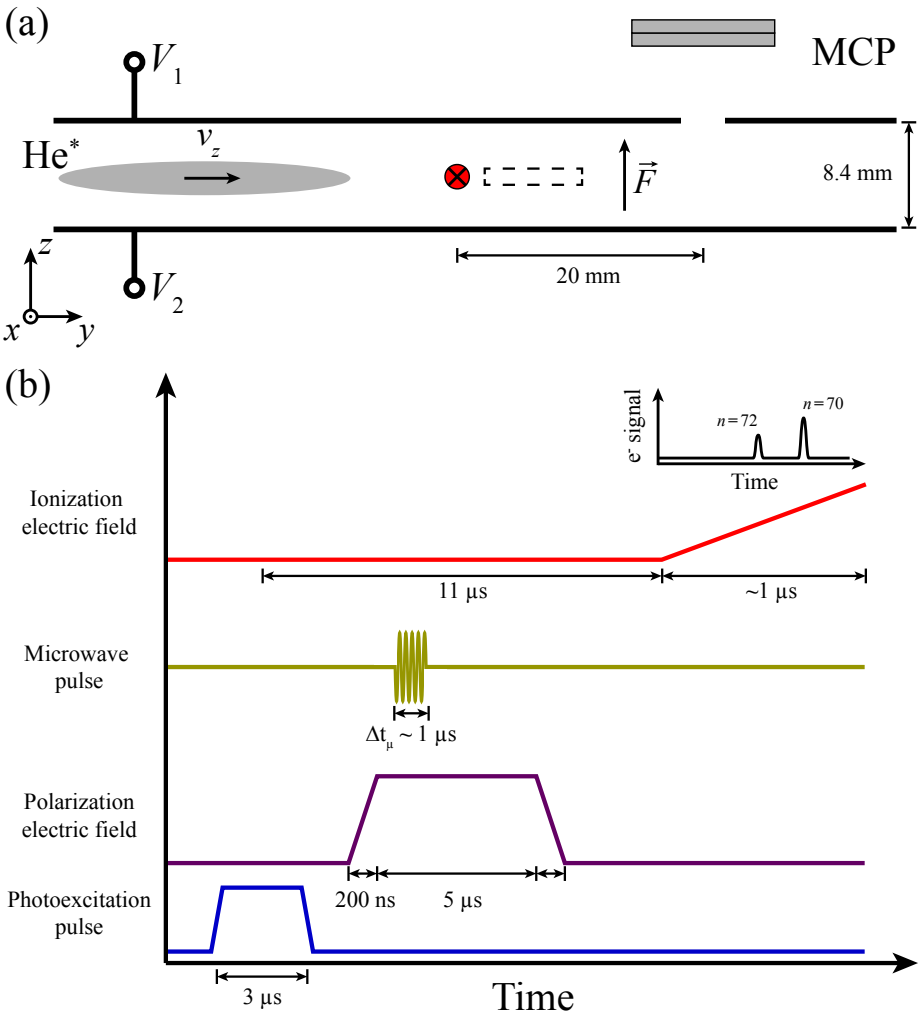

Figure 3.1: (a) Schematic diagram of the photoexcitation and detection region of the experimental apparatus. The position of laser photoexcitation and the approximate spatial extent of the Rydberg atom ensemble in the y dimension during microwave interrogation are indicated by the red circle and dashed rectangle, respectively. (b) Sequence of events in each experimental cycle, including laser photoexcitation, Rydberg state polarization, microwave interrogation, and state-selective electric field ionization (not to scale). From [128].

these electrodes the atomic beam was crossed at right-angles by two co-propagating, frequency stabilized, cw laser beams. These lasers were operated at wavelengths of $\lambda_{\rm UV} = 388.975$ nm and $\lambda_{\rm IR} = 785.946$ nm to excite the metastable atoms to Rydberg states by the $1s2s\,^3S_1 \rightarrow 1s3p\,^3P_2 \rightarrow 1s70s\,^3S_1$ two-photon excitation scheme. The laser beams were focussed to full-width-at-half-maximum (FWHM) beam waists of ~ 100 μm. By applying a pulsed potential, V_1, to the upper electrode in Fig. 3.1(a) to bring the atoms in the photoexcitation region into resonance with the lasers for 3 μs [see Fig. 3.1(b)], 6 mm-long ensembles of Rydberg atoms were generated in each cycle of the experiment.

After photoexcitation, the electric field was switched again to polarize the $1s70s\,^3S_1$ atoms [see Fig. 3.1(b)]. Interactions within the excited ensemble were then probed by microwave spectroscopy on the single photon transition at ~ 37 GHz between the states that evolve adiabatically to the $1s70s\,^3S_1$ and $1s72s\,^3S_1$ levels in zero electric field. These states have quantum defects of $\delta_{70s} \simeq \delta_{72s} \simeq 0.296\,664$ [32] and exhibit quadratic Stark energy shifts in weak electric fields. Because the laser photoexcitation process was separated in time from microwave interrogation, the Rydberg atom number density, $n_{\rm Ry}$, could be adjusted by controlling the IR laser intensity, without affecting any other experimental parameters. After traveling 20 mm from the position of laser photoexcitation, the Rydberg atoms were detected by state-selective ramped-electric-field ionization beneath a 3 mm-diameter aperture in the upper electrode [see Fig. 3.1(a)]. This ionization step in the experiments was carried out by applying a slowly-rising ionization potential, V_2, to the lower electrode. The electrons from

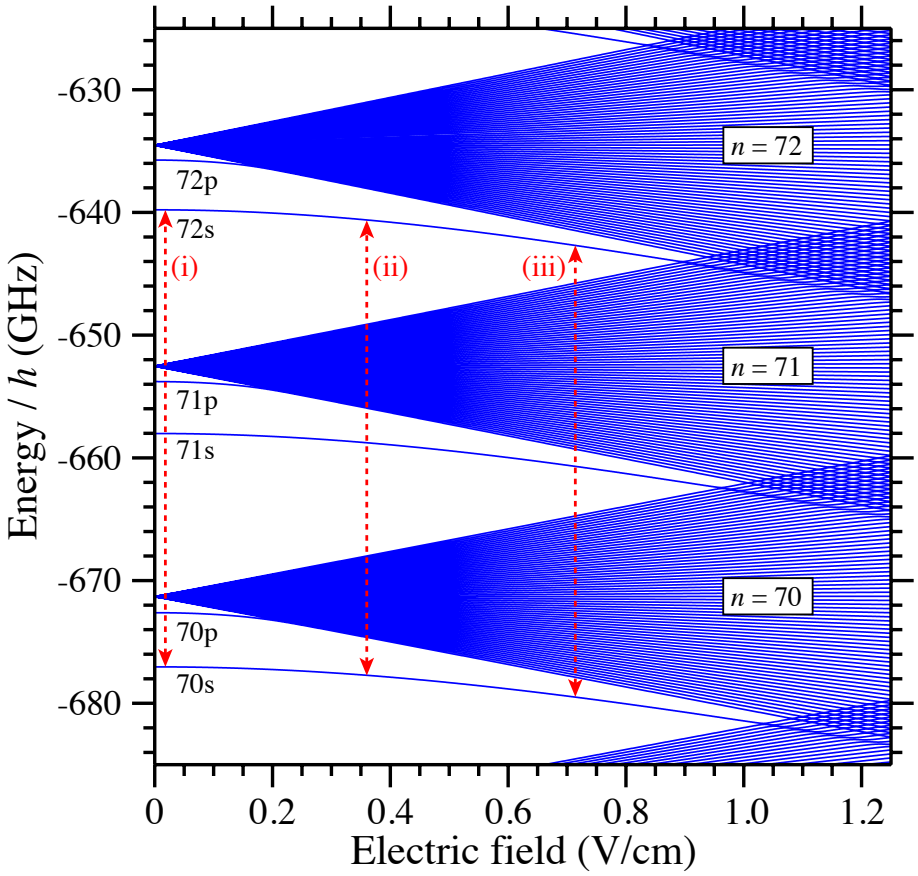

Figure 3.2: Stark structure of the triplet $m_\ell = 0$ Rydberg states of He with values of n ranging from 70 to 72. Experiments were performed following laser photoexcitation of the 70s state in zero electric field and the subsequent polarization of the excited ensemble of atoms in fields of (i) 18 mV cm^{-1}, (ii) 358 mV cm^{-1}, and (iii) 714 mV cm^{-1} as indicated. From [128].

the ionized Rydberg atoms were detected on a microchannel plate (MCP) detector located above this electrode. The rise time of the pulsed ionization electric field was selected to separate in time the electron signal from the $n = 70$ and $n = 72$ states.

3.2 Results

The mean-field energy-level shifts in the ensembles of polarized Rydberg gases were observed directly by microwave spectroscopy. To achieve this, reference measurements were first made in which the polarizing electric field was switched after photoexcitation from $0 \pm 1\,\mathrm{mV\,cm^{-1}}$ to $18\,\mathrm{mV\,cm^{-1}}$, inducing electric dipole moments of $\mu_{70} = 380$ D in the $1s70s\,{}^3S_1$ atoms. Here, and in the following, the dipole moments referred to represent the absolute value of the first derivative of the Stark energy shift with respect to the electric field. The $n = 70 \rightarrow n = 72$ transition ($\mu_{72} = 470$ D), indicated by the dashed line labelled (i) in Fig. 3.2, was then driven by a 1 μs-long microwave pulse [see Fig. 3.1(b)]. The corresponding Fourier-transform-limited spectrum of the integrated electron signal associated with the $n = 72$ state is displayed in Fig. 3.3(a-i) (continuous curves). In order to identify and characterize the mean-field energy-level shifts in the ensembles of excited atoms measurements were performed at two Rydberg atom densities. The low (high) density data were recorded following the excitation of N_{Ry} ($16\,N_{\mathrm{Ry}}$) Rydberg atoms, and are displayed in blue (red) in the figure. For the small electric dipole moments induced in this case, no density-dependent energy-level shifts were observed.

To enhance the effects of electrostatic dipole interactions within the

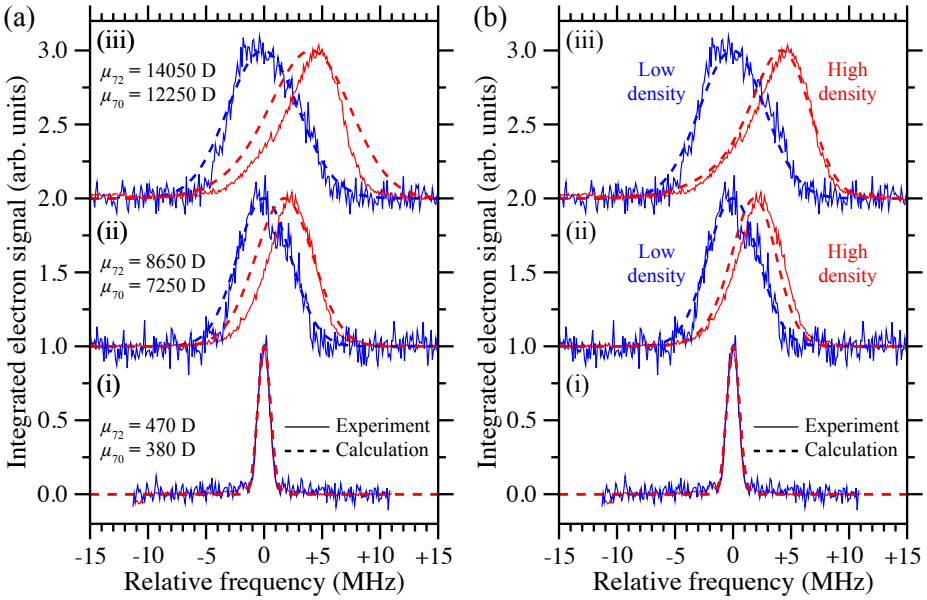

Figure 3.3: Experimentally recorded (continuous curves) and calculated (dashed curves) spectra of transitions between the Stark states that evolve adiabatically to the 1s70s $^3S_1$ and 1s72s $^3S_1$ levels in zero electric field. The experiments were performed at low (blue curves) and high (red curves) Rydberg atom number densities, and spectra were recorded in polarizing electric fields of (i) 18 mV cm^{-1}, (ii) 358 mV cm^{-1}, and (iii) 714 mV cm^{-1}, for which μ_{70} = 380 D, 7250 D, and 12250 D (μ_{72} = 470 D, 8650 D, and 14050 D), respectively. The calculated spectra are presented (a) without, and (b) with effects of the local polarization of the medium on the macroscopic dielectric properties accounted for. The relative microwave frequencies on the horizontal axes are displayed with respect to the transition frequencies [(i) 37.2413 GHz, (ii) 37.1068 GHz, and (iii) 36.8094 GHz] recorded at low Rydberg atom number density. From [128].

Rydberg gases, subsequent spectra were recorded with further polarization. Increasing the electric field to 358 mV cm^{-1} (714 mV cm^{-1}) resulted in induced electric dipole moments of μ_{70} = 7250 D (μ_{70} = 12250 D), and μ_{72} = 8650 D (μ_{72} = 14050 D). In the spectra recorded in these fields, and displayed in Fig. 3.3(a-ii) and (a-iii), respectively, a significant dependence on the Rydberg atom density was observed. Comparison of the spectra in Fig. 3.3(a-ii) and (a-iii) with those in Fig. 3.3(a-i) reveals four notable features. When the atoms are more strongly polarized the spectral profiles: (1) become significantly broader than those in Fig. 3.3(a-i), even at low density; (2) exhibit density-dependent frequency shifts; (3) become asymmetric at high density with a sharp cut-off in intensity at higher microwave transition frequencies; and (4) display signatures of spectral narrowing at high density, in particular in Fig. 3.3(a-iii).

3.3 Simulations

To aid in the interpretation of the spectra, Monte Carlo calculations were performed in which the electrostatic dipole-dipole interactions within the many-particle system were treated. In these calculations, ensembles of Rydberg atoms were generated with randomly assigned positions. These ensembles had Gaussian spatial distributions with a FWHM of 100 μm (50 μm) in the x (z) dimension, and flat top distributions with a length of 3 mm in the y dimension. These distributions represent the spatial intensity profile of the laser beams in the z dimension, the spatial distribution of atoms with Doppler shifts within the spectral width ($\Delta\nu_{\mathrm{FWHM}} \simeq 15$ MHz) of the $1s2s\,{}^3S_1 \rightarrow 1s3p\,{}^3P_2$ transition in the x dimension, and half of the

length of the ensemble of atoms excited in the y dimension.

For each atom in the calculation the difference between the sum of the dipole-dipole interaction energies with all other atoms when it was (1) in the $n = 70$ state, i.e., $\mu_1 = \mu_2 = \mu_{70}$, and (2) in the $n = 72$ state, i.e., $\mu_1 = \mu_{72}$, and $\mu_2 = \mu_{70}$, was determined. To account for the sharp cut-off in the spectral profiles at high transition frequencies in the data recorded at high density in Fig. 3.3(a-ii) and (a-iii), it was necessary to impose a lower limit, $R_{\rm min}$, on the nearest-neighbor spacing between pairs of Rydberg atoms in the calculations. This minimum inter-atomic spacing is a consequence of the expansion of the pulsed supersonic beams as they propagate from the valve to the photoexcitation region in the experiments, a distance of 210 mm, and reflects the collision-free environment characteristic of these beams [102, 71]. From a global fit to all of the experimental data in Fig. 3.3, carried out by calculating and subsequently minimizing the root mean-squared error between the experimental data and the models obtained for different values of $R_{\rm min}$, the most appropriate value of $R_{\rm min}$ was found to be 11.5 μm.

We note that because the C_6, van der Waals coefficient of the 1s70s ^{3}S$_1$ level in He is $\sim$ 9.9 GHz μm^6, blockade at laser photoexcitation does not play a major role at the laser resolution in the experiments for atoms separated by more then $\sim$ 3.5 μm and therefore does not dominate this value of $R_{\rm min}$. Under these conditions, the distribution of $n = 70 \rightarrow n = 72$ transition frequencies was determined for each set of electric dipole moments (i.e., for each electric field strength) for atoms located within $\pm$0.75 mm of the center of the ensemble in the y-dimension to avoid edge effects. The

resulting data were convoluted with a Gaussian spectral function with a FWHM of 1 MHz corresponding approximately to the Fourier transform of the microwave pulses.

When the polarization of the individual atoms is increased they become more sensitive to low-frequency electrical noise [126]. This sensitivity led to the broadening of the resonances in the low-density regime in Fig. 3.3(a-ii) and (a-iii). The effect of this spectral broadening was introduced in the calculations as a perturbing electric field which caused a relative shift in the energy of the $n = 70$ and $n = 72$ Stark states, proportional to their electric dipole moments. The spectra calculated following the generation of low density samples containing $N_{\mathrm{Ry}} = 2\,813$ atoms and including the contributions from this electric field noise are displayed in Fig. 3.3(a) (blue dashed curves). Comparing the experimental data with the results of these calculations indicates that the broadening observed was commensurate with white noise with a root-mean-square amplitude of $F_{\mathrm{noise}} = 2\,\mathrm{mV\,cm^{-1}}$.

In the more polarized gases, increasing the Rydberg atom density is seen to shift the resonant microwave transition frequencies by $\sim +3$ MHz and $\sim +5$ MHz in Fig. 3.3(a-ii) and (a-iii), respectively, from those recorded at low density. These density-dependent changes indicate that atom-atom interactions dominate the spectral broadening caused by F_{noise}. The mean-field shifts in transition frequency were found to agree with those seen in the results of the calculations upon increasing the number of excited atoms by a factor of 16, matching the experiments, to $N_{\mathrm{Ry}} = 45\,000$ [red dashed curves in Fig. 3.3(a)]. The positive shifts in transition frequency with increasing density are a consequence of the predominantly repulsive

electrostatic dipole interactions within the elongated ensemble of Rydberg atoms in the experiments, and the larger energy shift of the more polar, $n = 72$ state under these conditions.

However, the spectral narrowing observed at high density in the experimental data is not seen in the calculations in Fig. 3.3(a). To account for this it was necessary to consider the contribution of the local polarization of the Rydberg gases on their dielectric properties [84]. In a simple model of the dielectric Rydberg gas, the local polarization $P_{\text{loc}} = n_{\text{loc}}\,\mu_{70}$ (n_{loc} is the Rydberg atom number density obtained in the numerical calculation within a sphere of radius 25 μm surrounding each atom) can be considered to shield each atom from the laboratory electrical noise, reducing it to $F_{\text{loc}} = \max(\{0, F_{\text{noise}} - S_\kappa P_{\text{loc}}/\epsilon_0\})$, where S_κ is a constant factor that accounts for the geometry of the ensemble of atoms in the experiments. This shape factor is a fitting parameter associated with the proportion of local Rydberg atoms affected by the dielectric screening of the noise, which varies with R_{min} and accounts for the arbitrary choice of the radius of the sphere in which the local atom density is calculated. For $S_\kappa = 0.1$, there is excellent agreement between the results of the calculations and the experimental data as can be seen in Fig. 3.3(b). This indicates the emergence of macroscopic electrical properties of the Rydberg gas when strongly polarized. In the experiments, free He^+ ions, generated by photoionization of Rydberg atoms, would give rise to spectral broadening, or, if they increase the strength of the local electric fields within the ensembles of atoms, shifts of the spectral features toward lower transition frequencies (see Fig. 3.2). They are not expected to contribute to spectral narrowing such as that

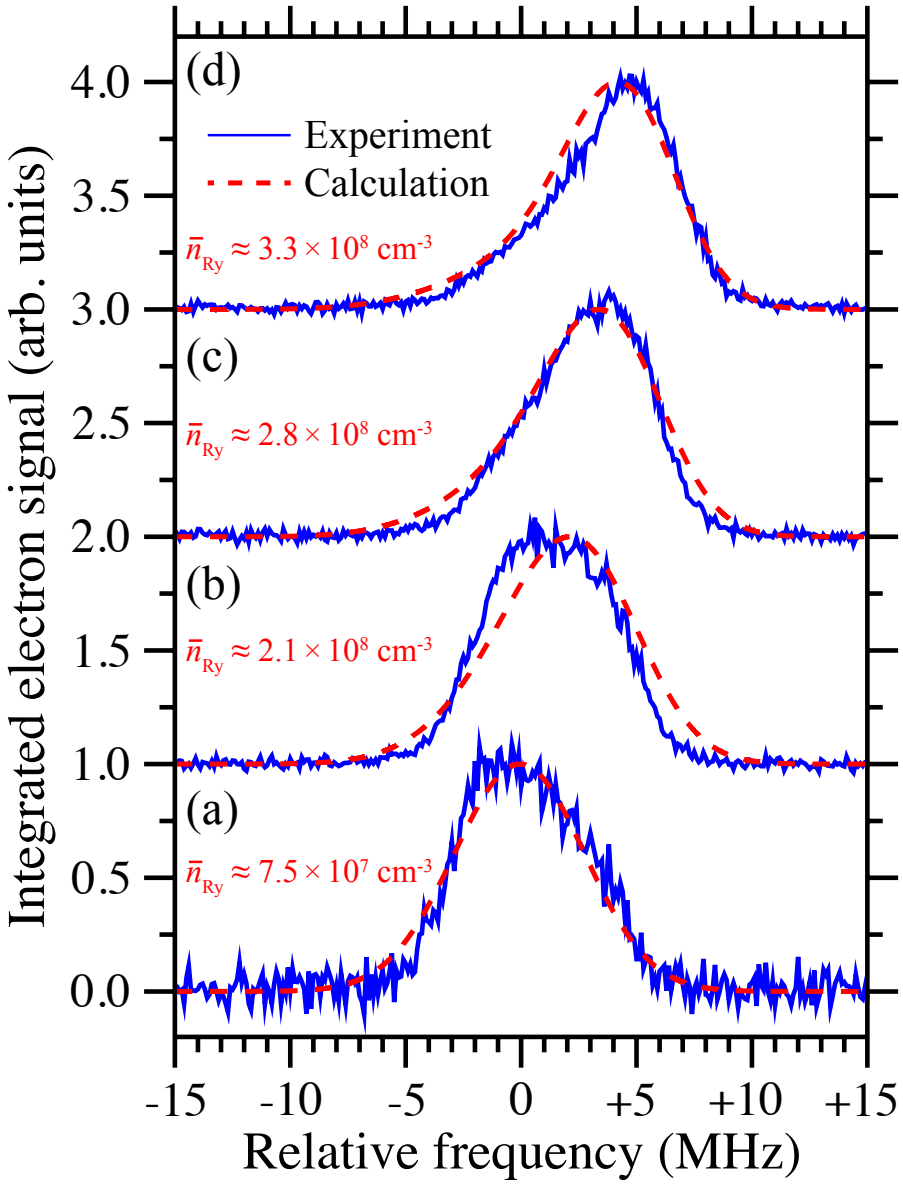

Figure 3.4: Experimentally recorded (continuous curves) and calculated (dashed curves) dependence of the $n = 70 \rightarrow n = 72$ spectra of the most strongly polarized ensemble of atoms, for which $\mu_{70} = 12\,250$ D and $\mu_{72} = 14050$ D, on the Rydberg atom density. From [128].

observed in Fig. 3.3(a,ii-iii) and (b,ii-iii). For these reasons, and because we do not observe free ions or electrons in the process of ionization of the Rydberg atoms, we conclude that they do not contribute significantly to the experimental observations.

Further comparisons of experimental and calculated spectra of the most polarized atoms [Fig. 3.3(b,iii)] over a range of Rydberg atom densities are presented in Fig. 3.4. From these data, it can be seen that the experimental spectra, recorded upon increasing N_{Ry} by factors of 5, 9.5 and 16 [Fig. 3.4(b), (c) and (d), respectively] from the initial low density case [Fig. 3.4(a)], agree well with the calculated spectra containing equivalent proportions of atoms, i.e., $N_{\mathrm{Ry}} = 2\,813,\ 14\,063,\ 26\,719$, and $45\,000$. From the results of the calculations the mean Rydberg atom number densities, $\overline{n}_{\mathrm{Ry}}$, within the samples could be determined to range from $\overline{n}_{\mathrm{Ry}} = 7.5 \times 10^7$ cm^{-3} to 3.3×10^8 cm^{-3}, as indicated. In these strongly polarized gases the laboratory electric field noise, F_{noise}, is completely screened when $S_\kappa P_{\mathrm{loc}}/\epsilon_0 \geq 2$ mV cm^{-1}, i.e., when $n_{\mathrm{loc}} \geq 4.5 \times 10^8$ cm^{-3}, and the absolute energy-level shift of each atom is ~ 20 MHz.

3.4 Conclusions

In conclusion, we have carried out spectroscopic studies of mean-field energy-level shifts in strongly polarized Rydberg gases by driving microwave transitions between Rydberg-Stark states with similar electric dipole moments. The resulting spectra yield detailed information on the spatial distributions of the atoms. Spectral narrowing observed at high number density is attributed to changes in the local dielectric properties

within the medium from those in free space, and reflects the macroscopic electrical properties of the atomic samples that emerge under these conditions. From these results, it is seen that for atoms prepared in states with static electric dipole moments on the order of 10000 D dipole-dipole interactions result in frequency shifts in excess of 10 MHz for atom-atom separations of $\lessapprox 10$ μm. To ensure that such frequency shifts remain below this value, and hence, are not detrimental to quantum-state–selective circular state preparation the number densities of excited atoms in experiments must be maintained below 10^8 cm^{-1}.

Chapter 4

Superconducting Transmission Line Resonator

In the development of hybrid approaches to quantum optics and quantum information processing superconducting circuits and qubits are uniquely scalable systems with high gate operation rates but short coherence times [115]. On the other hand, atoms in Rydberg states offer lower gate operation rates for similar transition frequencies but, being in the gas phase, can possess significantly longer coherence times [97]. The key component required for coupling these two qubits is a high quality microwave resonator. To maintain scalability, transmission line resonators offer particular advantages in such hybrid system setups.

In this chapter the characteristic properties of superconducting transmission line resonators are described. These properties are then employed in the theoretical studies in the following chapters.

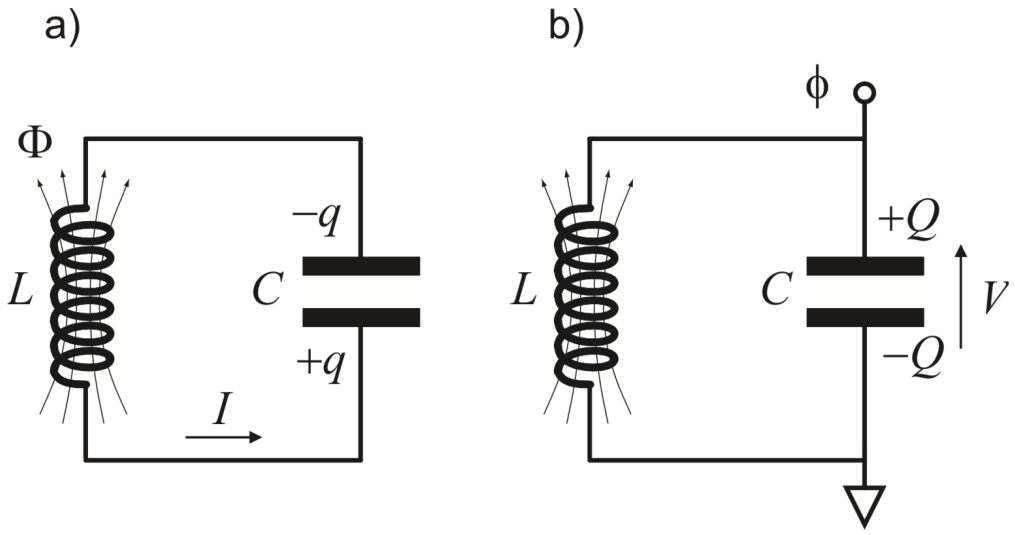

Figure 4.1: Simple *LC*-circuit electrical oscillator: (a) In order to derive a Lagrangian where the single degree of freedom is the charge, q, the usual sign convention for the flow of the current, I, from $-q$ to q can be used. (b) The sign convention in the text, where the positive and negative signs of the charge, Q, have been flipped with respect to the current, leads to the magnetic flow as the single degree of freedom in the Lagrangian describing the *LC*-circuit. From [41].

4.1 Quantization of a 1D Transmission Line Resonator

A one-dimensional transmission line resonator can be modelled as a series of harmonic *LC*-circuits. This electric circuit element consists of an inductor with inductance L and a capacitor with capacitance C. The resonant circuit is described by the potential energy, E_C, stored in the capacitor

$$E_C = \frac{CV^2}{2}, \tag{4.1}$$

where V is the voltage across the capacitor, and the kinetic energy stored in the magnetic field, E_L, which is induced by the current I, flowing through the inductor

$$E_L = \frac{1}{2} L I^2. \tag{4.2}$$

The inductor current $I = \dot{Q}$ is the rate of change of capacitor charge with time. The magnetic flux Φ can be expressed in terms of the applied voltage using Faraday's law of inductance,

$$\Phi(x,t) = \int_0^t d\tau \; V(x,\tau). \tag{4.3}$$

Considering the definition of the inductance, i.e., $L = \Phi/I$, the energy stored in the capacitor has the form of a kinetic energy and the energy stored in the inductor is analogous to the potential energy of a particle in one-dimensional space. Consequently, the Lagrangian for the LC-circuit can be written in terms of the magnetic flow as

$$\mathcal{L}_{LC} = \frac{1}{2} C \dot{\Phi}^2 - \frac{1}{2L} \Phi^2. \tag{4.4}$$

The conjugate momentum to this single degree of freedom, Φ, is therefore

$$\frac{\partial \mathcal{L}}{\partial \dot{\Phi}} = C\dot{\Phi} \tag{4.5}$$

$$= Q, \tag{4.6}$$

and hence the capacitator charge Q. Thus, the Hamiltonian for the LC-circuit is derived as

$$\begin{aligned} H_{LC} &= Q\dot{\Phi} - \mathcal{L} \\ &= \frac{C}{2}\left(\frac{d\Phi}{dt}\right)^2 + \frac{1}{2L}\Phi^2, \end{aligned} \tag{4.7}$$

which is the electronic version of a single-mode harmonic oscillator.

The analogous lumped circuit element model of a 1D transmission line is a series of linearly coupled *LC*-circuits. The Hamiltonian associated with the transmission line can therefore be written as a discretized sum of N inductively coupled *LC*-circuits

$$H_{TL} = \sum_{j=1}^{N} \frac{C}{2}\left(\frac{d\Phi}{dt}\right)^2 + \sum_{j=2}^{N} \frac{1}{2L}\left(\Phi_j - \Phi_{j-1}\right)^2. \tag{4.8}$$

This expression has the same form as a harmonic chain. In the continuum limit, a capacitance per unit length, c, and inductance per unit length, l, can be defined. For a transmission line of length d, the Lagrangian can then be written as [12]

$$\mathcal{L}_{TL} = \int_0^d dx \left[\frac{c}{2}(\partial_t \Phi)^2 - \frac{1}{2l}(\partial_x \Phi)^2\right], \tag{4.9}$$

which leads to the Euler-Lagrange equation

$$\left(\frac{d^2}{dt^2} - \frac{1}{lc}\frac{\partial^2}{\partial x^2}\right)\Phi = 0. \tag{4.10}$$

This is the equivalent of a wave equation with velocity $v = \frac{1}{\sqrt{lc}}$. In order that the transmission line acts as a resonator which stores an electromagnetic field in form of standing waves, series capacitances are implemented at each end of the transmission line to impose open-circuit boundary conditions such that

$$\left.\frac{\partial \Phi}{\partial x}\right|_{x=0} = \left.\frac{\partial \Phi}{\partial x}\right|_{x=d} = 0. \tag{4.11}$$

The boundary conditions are time-independent. Hence, the magnetic flux field can be factorized

$$\Phi(x,t) = \sum_{n=0}^{\infty} f_n(t)\phi_n(x) \tag{4.12}$$

where the amplitude $f_n(t)$ of each field mode n depends only on time and $\phi_n(x)$ are the normalized spatial eigenfunctions, whose derivatives vanish at the boundaries. These normal modes are expressed as

$$\phi_n(x) = \sqrt{\frac{2}{L}} \cos(k_n x) \tag{4.13}$$

where $k_n = \frac{n\pi}{L}$ with $n \in \mathbb{N}$. The properties of these normal modes, i.e., that

$$\int^L dx \phi_n(x) \phi_m(x) = \delta_{nm}, \tag{4.14}$$

and hence

$$\int^L dx \partial_x \phi_n(x) \partial_x \phi_m(x) = k_n^2 \delta_{nm}, \tag{4.15}$$

permit their use as an orthonormal basis in which to diagonalize the Lagrangian in Eq. (4.9),

$$\mathcal{L}_{\mathrm{TL}} = \frac{c}{2} \sum_{n=0}^{\infty} \left[(\partial_t f_n)^2 - \omega_n f_n^2 \right], \tag{4.16}$$

where the wavevector is defined as $k_n = \omega_n / v$. This Lagrangian, and subsequently the Hamiltonian, constitute a sum of independent simple harmonic oscillator normal modes, where the momentum conjugate to the amplitude $f_n(t)$ is

$$q_n = \frac{\partial \mathcal{L}}{\partial(\partial_t f_n)} = c \partial_t f_n. \tag{4.17}$$

This set of independent normal modes can be promoted to quantum operators by imposing the commutation relation $\left[\hat{q}_n, \hat{f_m}\right] = -i\hbar\delta_{n,m}$. Since the classical Hamiltonian, which follows from Eq. (4.16),

$$H_{\mathrm{TL}} = \sum_{n=0}^{\infty} \left\{ \frac{1}{2c} q_n + \frac{c}{2} \omega_n^2 f_n^2 \right\}, \tag{4.18}$$

has a form that resembles the free electromagnetic field, and its quantization can be performed in a similar fashion [116]. The quantum operators $\hat{q}_n$, $\hat{f_m}$ are expressed in terms of creation and annihilation operators

$$\hat{f_n} = \sqrt{\frac{\hbar}{2\omega_n c}}\left(\hat{a}_n^\dagger + \hat{a}_n\right), \tag{4.19}$$

and

$$\hat{q}_n = i\sqrt{\frac{\hbar\omega_n c}{2}}\left(\hat{a}_n^\dagger - \hat{a}_n\right), \tag{4.20}$$

lead to the quantization of the magnetic flux and charge density via Eq. (4.12) and (4.17). These operators obey the standard field commutation relation

$$\begin{aligned}\left[\hat{q}(x), \hat{\Phi}(x')\right] &= -i\hbar\sum_n^\infty \phi(x)\phi(x') \\ &= -i\hbar\delta(x-x').\end{aligned} \tag{4.21}$$

Ultimately, the quantum Hamiltonian for the transmission line resonator with finite length d is

$$H_{TL} = \int_0^d dx\left\{\frac{1}{2c}\hat{q}^2 + \frac{1}{2l}(\partial_x\hat{\phi})^2\right\}, \tag{4.22}$$

and can therefore be simplified by expressing it in terms of the ladder operators, taking the familiar form,

$$\hat{H}_{TL} = \sum_{n=0}^\infty \hbar\omega_n\left(\hat{a}^\dagger\hat{a} + \frac{1}{2}\right). \tag{4.23}$$

4.2 Dissipation from a 1D Transmission Line Resonator

Consider a circuit quantum electrodynamic system composed of a superconducting transmission-line resonator coupled to a co-planar waveguide

which acts as an input/output channel. We aim to derive an expression for the quality factor of the transmission line resonator using a full quantum treatment of the coupled resonator-waveguide system. The classical

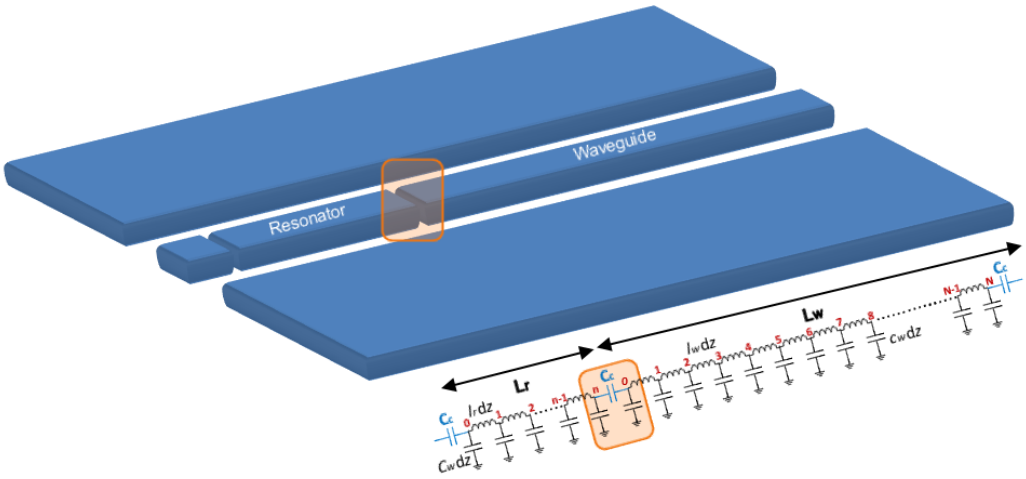

Figure 4.2: The resonator-waveguide system and its lumped circuit analogue. The resonator and waveguide can be considered as a sum of harmonic *LC*-circuits, where coupling capactiances at each end impose boundary conditions.

Lagrangian of this system can be written as a sum of the resonator and waveguide Lagrangians, with the addition of the capacitive coupling between them [64], i.e.,

$$\mathcal{L}_{\text{Tot}} = \text{L}_{\text{Res}} + \mathcal{L}_{\text{WG}} + \mathcal{L}_{\text{C}}, \tag{4.24}$$

where

$$\mathcal{L}_{\text{Res}} = \frac{1}{2}C_{\text{c}}\dot{\phi}_0^2 + \frac{1}{2}\sum_{\nu=1}^{n}\left[c_{\text{r}}dz\dot{\phi}_\nu^2 - \frac{\left(\phi_\nu - \phi_{\nu-1}\right)^2}{l_{\text{r}}dz}\right] + \frac{1}{2}C_{\text{c}}\dot{\phi}_n^2, \tag{4.25}$$

$$\mathcal{L}_{\text{WG}} = \frac{1}{2}C_{\text{c}}\dot{\Phi}_0^2 + \frac{1}{2}\sum_{\mu=1}^{N}\left[c_{\text{w}}dz\dot{\Phi}_\mu^2 - \frac{\left(\Phi_\mu - \Phi_{\mu-1}\right)^2}{l_{\text{w}}dz}\right] + \frac{1}{2}C_{\text{c}}\dot{\Phi}_N^2, \tag{4.26}$$

and

$$\mathcal{L}_{\mathrm{C}} = -C_{\mathrm{c}} \cdot \dot{\phi}_n \cdot \dot{\Phi}_0. \tag{4.27}$$

Here C_{c} is the coupling capacitance at each end of the resonator denoted by the subscript r, $c_{\mathrm{r,w}}$ and $l_{\mathrm{r,w}}$ are the capacitance and inductance per unit length of the resonator, c_{r} and l_{r}, and waveguide, c_{w} and l_{w}, respectively, and ϕ_n (Φ_n) is the magnetic flux at each point n in the respective lumped circuit element sequences associated with the resonator (waveguide), as indicated in Fig. 4.2. These expressions can be significantly simplified following diagonalization. An important approximation in the derivation of the corresponding Hamiltonian is the assumption that

$$\frac{C_{\mathrm{c}}}{c_{\mathrm{r,w}} L_{\mathrm{r,w}}} \ll 1. \tag{4.28}$$

This criterion is generally fulfilled since the coupling capacitances must be small to allow for an appropriate build-up and storage of an electromagnetic field inside the resonator. Writing the conjugate momenta ξ_n, Ξ_n of the variables q_n, Q_n leads to the Hamiltonian

$$\mathcal{H}_{\mathrm{Tot}} = \frac{1}{2} \sum_{n=0} \left[q_n^2 + \omega_n^2 \xi_n^2 \right] + \frac{1}{2} \sum_{m=0} \left[Q_m^2 + \Omega_m^2 \Xi_n^2 \right] + C_{\mathrm{c}} \cdot \sum_{n=0} \varphi_n(0) q_n \sum_{m=0} \psi_m(0) Q_m. \tag{4.29}$$

This expression describes two harmonic oscillators capacitively coupled at each end. Using the standard quantization procedure of a harmonic oscillator as shown in the previous section and by selectively exciting a single resonator mode, one obtains

$$\hat{\mathcal{H}} = \hbar\omega \hat{a}^\dagger \hat{a} + \hbar \sum_n \Omega_n \hat{b}_n^\dagger \hat{b}_n - \hbar \sum_{k=0} g_k \left(\hat{b}_k^\dagger - \hat{b}_k \right) \left(\hat{a}^\dagger - \hat{a} \right), \tag{4.30}$$

where the coupling strength g_k can be expressed in terms of experimental parameters only, such that

$$g_k = C_\mathrm{c}\sqrt{\frac{1}{c_\mathrm{r}L_\mathrm{r}}}\frac{1}{\sqrt{1+2\frac{C_\mathrm{c}}{c_\mathrm{r}L_\mathrm{r}}+C_\mathrm{c}^2Z_\mathrm{r}^2\omega^2}}\sqrt{\frac{1}{c_\mathrm{w}L_\mathrm{w}}}\frac{1}{\sqrt{1+2\frac{C_\mathrm{c}}{c_\mathrm{w}L_\mathrm{w}}+C_\mathrm{c}^2Z_\mathrm{w}^2\Omega_k^2}}\sqrt{\omega\Omega_k}, \tag{4.31}$$

where $Z_{\mathrm{r,w}}$ is the impedence of the resonator and waveguide, respectively. It is known that the coupling strength should be proportional to the coupling capacitance and the impedance of the waveguide, since the influence of the transmission line on the resonator is generally due to its impedance [56]. In addition, the higher the energy of the mode excited/supported by the resonator and waveguide, the higher the strength with which they couple to each other. Assuming they are made from the same material, and that all terms $\propto C_\mathrm{c}^2$ are negligible, the coupling constant in Eq.(4.31) then simplifies significantly to

$$g_k \approx \frac{C_\mathrm{c}^2}{\omega_\mathrm{r}}Z_0\pi\sqrt{k}, \tag{4.32}$$

with the the characteristic impedence of the transmission line Z_0. This approximation of the coupling strength g_k has the correct dimension of a frequency, i.e., Hz, and is in accordance with what we would expect for the simplified case described here.

Following the standard quantum Langevin approach for a harmonic osciallator coupled to a collection of electromagnetic reservior oscillators, i.e., the waveguide taken to be in thermal equilibrium, under the RWA, one arrives at a decay rate [39]

$$\gamma = 2\pi\sum_n g_n^2\delta\left(\omega-\Omega_n\right) \to 2\pi\int\frac{dn}{\Delta n}\,g_n^2\delta\left(\omega-\Omega_n\right). \tag{4.33}$$

The frequency modes of the waveguide are defined by a transcendental equation that follows from the wave-equation and boundary conditions of the Euler-Lagrange equations of motion. The solution of these equations can be obtained by a Taylor expansion up to first order, under the previous assumption Eq.(4.28), such that

$$\Omega_n = \frac{\pi \cdot n}{\left(2\frac{C_c}{c_w L_w} + 1\right) L_w \sqrt{c_w l_w}}. \tag{4.34}$$

If the waveguide and resonator are considered to be composed of the same material, $c_r = c_w = c$ and $l_r = l_w = l$, and the waveguide is a semi-infinite transmission line, $L_w \to \infty$, for example, acting as a measurement channel, the resonator's quality factor, $Q_{ext} = \omega/\gamma$, can be written as

$$Q_{ext} = \frac{2C_c\left(1 + C_c^2 Z^2 \omega^2\right) + cL\left(1 + C_c^2 Z^2 \omega^2\right)^2}{C_c^2 Z \omega}. \tag{4.35}$$

where $Z = \sqrt{l/c}$ is the characteristic impedance. This quality factor is idealized and therefore tends to infinity as the coupling capacitances approaches zero. However, if one wants to precisely match the true experimental parameters, an intrinsic saturation of the resonator's quality factor towards which the idealized Q-factor tends [42] must be considered. A saturation occurs because of the presence of additional input (drive) and ouput (measurement) decay channels not considered in the theoretical treatment so far, which is phenomenologically accounted for via

$$\frac{1}{Q} = \frac{1}{Q_{int}} + \frac{1}{Q_{ext}}, \tag{4.36}$$

by introducing an empirical quality factor saturation limit Q_{int}.

(a) The calculated Q-Factor

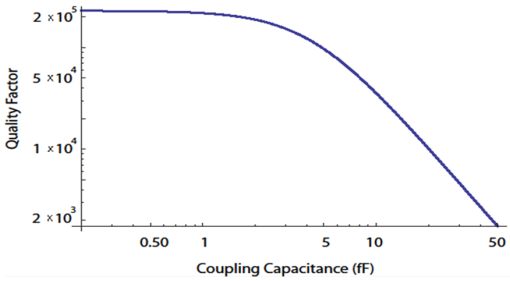

(b) The measured Q-Factor. From [42].

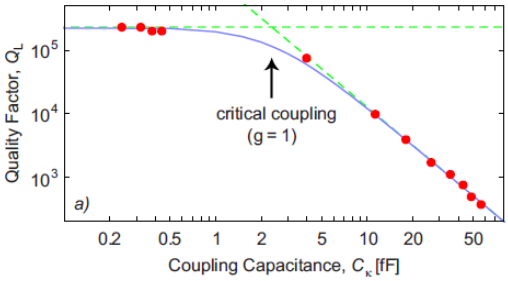

Figure 4.3: Comparison of the here calculated Q-factor and the measurement by Goeppl et al. Both curves show qualitatively similar behavior, whereas the precise values differ because the details of the experimental parameters of the waveguide could only be estimated from the published information.

ω_0	resonator fundamental angular frequency	14.7215 GHz
L_r	length of the resonator	28.449 mm
$c_\mathrm{r}, c_\mathrm{w}$	capacitance per unit length	$1.27 \cdot 10^{-10}$ F/m
$l_\mathrm{r}, l_\mathrm{w}$	inductance per unit length	$4.53 \cdot 10^{-7}$ H/m
Q_int	intrinsic quality factor	$2.3 \cdot 10^5$

Table 4.1: The values used for the theoretical calculation of the Q-factor as published by Goeppl et al. [42].

Taking this into account and using the values listed in the table above for the waveguide and resonator parameters, the dependence of the resonator quality factor, Q, on the coupling capacitances, C_c, are obtained and dis-

played in Fig. 4.3 (a). This result is in excellent qualitative agreement with the experimental data and calculation by Goeppl et al. [42] as shown in Fig. 4.3 (b). The discrepencies between the calculation and experimental findings can be explained by the fact that it was necessary to estimate some of the parameters of the waveguide that were not explicitely stated in the article.

Chapter 5

Cooling a transmission-line resonator with a beam of Rydberg atoms

A hybrid quantum system composed of atoms prepared in circular Rydberg states coupled to a transmission line resonator offers new opportunities for processing and storing quantum information. However, it also offers possibilities for exploiting the Rydberg atoms or the resonator to engineer particular quantum states of interest of the other partner system. For example, the Rydberg atoms can be employed to add or remove photons from a complementary resonator mode on, or near, resonance with the Rydberg transition frequency in order to prepare particular Fock states of the resonator. Another possibility is to generate entanglement by exploiting a sequential interaction of multiple atoms with a selected resonator mode.

In this, and the following chapter, the first of these schemes is studied. First by using an analytical method and then using a numerial approach in order to improve the scheme's efficiency.

5.1 The atomic beam as an engineered quantum reservoir

Recently, one particular focus of hybrid quantum system research has been the quantum state preparation of an individual system with the help of another quantum system [1].

To investigate the extent to which Rydberg atom beams can be employed to manipulate, and in particular cool, a selected mode of a transmission-line resonator, we now consider a beam of atoms prepared in circular Rydberg states crossing the resonator and thus interacting with its thermal electromagnetic field via their electric dipole transition moments. In this treatment we consider two selected circular Rydberg states with values of n differing by 1 in each atom. The lower selected state is considered as the ground state $|g\rangle$, while the higher state is the excited state $|e\rangle$.

First we consider the internal dynamics of the atom-resonator system, in an analogous way implemented by Pielawa *et al.* [92]. Additionally, we include an open quantum system approach by accounting for thermal heating and dissipation of the resonator due to its coupling to a thermal bath. The problem will be studied on a coarse-grained time scale, Δt, where Δt is significantly longer than the average atom-resonator interaction time τ. If the arrival rate of atoms in state $|g\rangle$ in the resonator is defined as

r, then in order to ensure that at most one atom at a time interacts with the resonator, we must assume that $r\tau \ll 1$. The product $r\Delta t \ll 1$ gives the average number of atoms flying over the resonator during the time-interval studied. To characterize and analyze the dynamics of this system, we need to distinguish between two cases:

1) In the case of an atom being present above the resonator, the internal dynamics of the resonator-atom system is governed by the Jaynes-Cummings Hamiltonian [62]

$$\hat{\mathcal{H}} = \underbrace{\hbar\omega_c\left(\frac{\hat{\sigma}_z}{2} + \hat{a}^\dagger\hat{a}\right)}_{\hat{\mathcal{H}}_0} + \underbrace{\hbar\frac{\Delta}{2}\hat{\sigma}_z + \hbar g\left(\hat{\sigma}^\dagger\hat{a} + \hat{a}^\dagger\hat{\sigma}\right)}_{\hat{\mathcal{H}}_1}, \tag{5.1}$$

where the population difference operator is $\hat{\sigma}_z = |\mathrm{e}\rangle\langle\mathrm{e}| - |\mathrm{g}\rangle\langle\mathrm{g}|$, and $\hat{\sigma} \equiv |\mathrm{g}\rangle\langle\mathrm{e}|$ and $\hat{\sigma}^\dagger \equiv |\mathrm{e}\rangle\langle\mathrm{g}|$ are the pseudo-spin operators of the two-level atom – its lowering and raising operator, respectively. The field mode creation and annihilation operators are $\hat{a}^\dagger$, $\hat{a}$. The average interaction strength mediated by the electric dipole coupling is g, and $\Delta = \omega_0 - \omega_c$ describes the detuning between the transition frequency of the atom and the fundamental frequency of the resonator. We define the system and interaction Hamiltonian as above so that the commutator between them vanishes, i.e.,

$$\left[\hat{\mathcal{H}}_0, \hat{\mathcal{H}}_1\right] = 0. \tag{5.2}$$

Taking advantage of a vanishing commutator simplifies the Baker-Campbell-Hausdorff formula [24], $e^{\hat{Z}} = e^{\hat{\mathcal{H}}_0}e^{\hat{\mathcal{H}}_1}$, with

$$\hat{Z} = \ln\left(e^{\hat{\mathcal{H}}_0}e^{\hat{\mathcal{H}}_1}\right) \tag{5.3}$$

$$= \hat{\mathcal{H}}_0 + \hat{\mathcal{H}}_1 + \sum_{m=2}^{\infty} Z_m(\hat{\mathcal{H}}_0, \hat{\mathcal{H}}_1), \tag{5.4}$$

where the $Z_m(\hat{\mathcal{H}}_0, \hat{\mathcal{H}}_1)$ are homogeneous Lie polynomials, which are linear combinations of nested commutators of $\hat{\mathcal{H}}_0$ and $\hat{\mathcal{H}}_1$, and equal zero in this case. This allows us to write the unitary time-evolution operator as

$$\begin{aligned} \hat{U}(t) &= \mathrm{e}^{-\mathrm{i}\hat{\mathcal{H}}t/\hbar} \\ &= \mathrm{e}^{-\mathrm{i}\hat{\mathcal{H}}_0 t/\hbar}\mathrm{e}^{-\mathrm{i}\hat{\mathcal{H}}_1 t/\hbar}. \end{aligned} \tag{5.5}$$

2) The second case of interest is that which arises if no atom is present above the resonator. In this situation the interaction between atom and transmission line resonator can be considered "switched off". Both the resonator and atom evolve independently according to the system Hamiltonian

$$\hat{U}(t) = \exp\left(-i\hat{H}_0 t\right). \tag{5.6}$$

Taking both cases into account, we can quantify the evolution of the density matrix on a coarse-grained timescale, Δt, without an atom present as

$$\hat{\rho}_0(t + \Delta t) = e^{-i\hat{H}_0(\Delta t)}\hat{\rho}(t)e^{i\hat{H}_0(\Delta t)}, \tag{5.7}$$

and with an atom interacting with the resonator for a time $\tau \ll \Delta t$ as

$$\hat{\rho}_1(t + \Delta t) = e^{(-i\hat{H}_0\Delta t)}\left[\exp\left(-i\hat{H}_1\tau\right)\hat{\rho}(t)\exp\left(i\hat{H}_1\tau\right)\right]e^{(i\hat{H}_0\Delta t)}. \tag{5.8}$$

Given the density matrix at time t, the total system evolves under the Hamiltonian $\hat{H}_0$ over a time step Δt. The probability of this situation occuring is $(1 - r\Delta t)$, and corresponds to the situation in which there is no atom interacting with the resonator. On the other hand, the probability $r\Delta t$

of an atom being above, and thus interacting with, the resonator marks the situation where the density matrix undergoes a change described by the Hamiltonian $\hat{H}_1$ during the interaction time τ. Therefore, transforming the problem into an interaction picture with respect to the system Hamiltonian $\hat{H}_0$, the change in the internal evolution of the density matrix due to the interaction with an atom during time step Δt may be expressed as

$$\hat{\rho}_{\mathrm{tot}}(t+\Delta t) = \hat{\rho}_{\mathrm{tot}}(t)\cdot(1-r\Delta t) + r\Delta t \int d\tau P(\tau)\, \mathrm{e}^{-\mathrm{i}\hat{\mathcal{H}}_1\tau/\hbar}\hat{\rho}_{\mathrm{tot}}(t)\mathrm{e}^{\mathrm{i}\hat{\mathcal{H}}_1\tau/\hbar}, \quad (5.9)$$

where $\hat{\rho}_{\mathrm{tot}}(t)$ is the evolution of the density matrix up to a time t, which represents the beginning of the time step to be evaluated . The probability distribution $P(\tau)$ in Eq. (5.9) represents the distribution of interaction times that arise because in a realistic experimental setting a typical ensemble of circular Rydberg atoms do not all move with the same velocity across the resonator. Therefore we have to integrate over all possible interaction times weighted by their probility of occurance, $P(\tau)$.

Equ. (5.9) can be rearranged to yield an expression for the evolution of the total density matrix during each time interval Δt

$$\frac{\hat{\rho}_{\mathrm{tot}}(t+\Delta t)-\hat{\rho}_{\mathrm{tot}}(t)}{\Delta t} = r\int d\tau P(\tau)\, \mathrm{e}^{-\mathrm{i}\hat{\mathcal{H}}_1\tau/\hbar}\hat{\rho}_{\mathrm{tot}}(t)\mathrm{e}^{\mathrm{i}\hat{\mathcal{H}}_1\tau/\hbar} - r\hat{\rho}_{\mathrm{tot}}(t). \quad (5.10)$$

This resembles the discrete form of the derivative of the reduced density matrix, giving its equation of motion on a coarse-grained time scale Δt during which the interaction with a beam of atoms can occur. Since the atom is initially prepared in the ground state and both Hilbert-spaces are uncorrelated before the atom-resonator interaction, the initial density matrix can be factorized as a product of the reduced density matrix of the resonator, $\rho_{\mathrm{c}}(t)$, and the initial density matrix of the atom when entering

the resonator, which can be assumed to be in the ground state, $\rho_{\mathrm{tot}}(0) = \rho_{\mathrm{c}}(0) \otimes |g\rangle\langle g|$. Provided no atom is present above the resonator, the total density matrix of the system evolves as $\rho_{\mathrm{tot}}(t) = \rho_{\mathrm{c}}(t) \otimes |g\rangle\langle g|$.

However, if there is an atom present, the time-evolution operator takes on the form given in Eq. (5.5). Therefore we need to evaluate the effect of the interaction Hamiltonian on the time-evolution of the atomic ground state $|g\rangle$ to obtain an expression for the evolution of total density matrix in terms of the reduced density matrix $\rho_{\mathrm{c}}(t)$ when an atom is present. In order to evaluate the time-evolution operator in the interaction picture, the series expansion of the exponential function needs to be applied,

$$\exp\left(-ig\hat{H}_1\tau\right)|g\rangle \;=\; \sum_{k=0}^{\infty} \frac{(-ig\hat{H}_1\tau)^k}{k!}|g\rangle, \tag{5.11}$$

which requires the individual calculation of all higher-order terms of the interaction Hamiltonian, $\hat{H}_1^n$. The first six orders of the expansion are

$$\hat{H}_1 = \hat{a}\hat{\sigma}^\dagger + \hat{a}^\dagger\hat{\sigma} + \frac{\Delta}{2g}\hat{\sigma}_z, \tag{5.12}$$

$$\hat{H}_1^3 = (\hat{a}\hat{a}^\dagger)\hat{a}\hat{\sigma}^\dagger + (\hat{a}^\dagger\hat{a})\hat{a}^\dagger\hat{\sigma} + \left(\frac{\Delta}{2g}\right)^2\hat{H}_1 + \frac{\Delta}{2g}\left(\hat{a}\hat{a}^\dagger|e\rangle\langle e| - \hat{a}^\dagger\hat{a}|g\rangle\langle g|\right), \tag{5.13}$$

$$\begin{aligned}\hat{H}_1^5 = {} & \left(\hat{a}\hat{a}^\dagger\right)^2\hat{a}\hat{\sigma}^\dagger + \left(\hat{a}^\dagger\hat{a}\right)^2\hat{a}^\dagger\hat{\sigma} - \left(\frac{\Delta}{2g}\right)^4\hat{H}_1 + 2\left(\frac{\Delta}{2g}\right)^2\hat{H}_1^3 \\ & + \frac{\Delta}{2g}\left(\left(\hat{a}\hat{a}^\dagger\right)^2|e\rangle\langle e| - \left(\hat{a}^\dagger\hat{a}\right)^2|g\rangle\langle g|\right),\end{aligned} \tag{5.14}$$

$$\hat{H}_1^2 = \hat{a}\hat{a}^\dagger|e\rangle\langle e| + \hat{a}^\dagger\hat{a}|g\rangle\langle g| + \left(\frac{\Delta}{2g}\right)^2, \tag{5.15}$$

$$\hat{H}_1^4 = \left(\hat{a}\hat{a}^\dagger\right)^2|e\rangle\langle e| + \left(\hat{a}^\dagger\hat{a}\right)^2|g\rangle\langle g| + 2\left(\frac{\Delta}{2g}\right)^2\hat{H}_1^2 - \left(\frac{\Delta}{2g}\right)^4, \tag{5.16}$$

$$\hat{H}_1^6 = \left(\hat{a}\hat{a}^\dagger\right)^3|e\rangle\langle e| + \left(\hat{a}^\dagger\hat{a}\right)^3|g\rangle\langle g| + 3\left(\frac{\Delta}{2g}\right)^2\hat{H}_1^4 - 3\left(\frac{\Delta}{2g}\right)^4\hat{H}_1^2 + \left(\frac{\Delta}{2g}\right)^6. \tag{5.17}$$

For the expressions in Eq. (5.12) to (5.17) a re-occuring pattern for all the equations with even exponents can be identified, yielding a generating function in terms of a binomial series

$$\hat{H}_1^{2n} = \sum_{k=0}^{n} \binom{n}{k} \left(\frac{\Delta}{2g}\right)^{2k} \left[\left(\hat{a}\hat{a}^\dagger\right)^{n-k} |e\rangle\langle e| + \left(\hat{a}^\dagger\hat{a}\right)^{n-k} |g\rangle\langle g|\right]. \tag{5.18}$$

Using this expression, we can also determine a generating function for the interaction Hamiltonian with odd exponents via the matrix product $\hat{H}_1^{2n+1} = \hat{H}_1^{2n}\hat{H}_1$, which leads to

$$\hat{H}_1^{2n+1} = \sum_{k=0}^{n} \binom{n}{k} \left(\frac{\Delta}{2g}\right)^{2k} \left[\left(\hat{a}\hat{a}^\dagger\right)^{n-k} \left(\hat{a}\hat{\sigma}^\dagger + \frac{\Delta}{2g}|e\rangle\langle e|\right) + \left(\hat{a}^\dagger\hat{a}\right)^{n-k} \left(\hat{a}^\dagger\hat{\sigma} - \frac{\Delta}{2g}|g\rangle\langle g|\right)\right]. \tag{5.19}$$

To further simplify the expressions in Eq.(5.18) and (5.19), the binomial expansion $(x+y)^n = \sum_{k=0}^{n} \binom{n}{k} x^{n-k}y^k$ can be used, leading to,

$$H_1^{2n} = \left[\hat{a}\hat{a}^\dagger + \left(\frac{\Delta}{2g}\right)^2\right]^n |e\rangle\langle e| + \left[\hat{a}^\dagger\hat{a} + \left(\frac{\Delta}{2g}\right)^2\right]^n |g\rangle\langle g|, \tag{5.20}$$

$$\hat{H}_1^{2n+1} = \left[\hat{a}\hat{a}^\dagger + \left(\frac{\Delta}{2g}\right)^2\right]^n \left(\hat{a}\hat{\sigma}^\dagger + \frac{\Delta}{2g}|e\rangle\langle e|\right) + \left[\hat{a}^\dagger\hat{a} + \left(\frac{\Delta}{2g}\right)^2\right]^n \left(\hat{a}^\dagger\hat{\sigma} - \frac{\Delta}{2g}|g\rangle\langle g|\right). \tag{5.21}$$

Ultimately, we obtain for the series expansion of the time-evolution operator

$$\exp\left(-ig_{ac}\hat{H}_1\tau\right)|g\rangle = \sum_{k=0}^{\infty} \frac{(-ig\hat{H}_1\tau)^k}{k!}|g\rangle, \tag{5.22}$$

$$\begin{aligned} &= \sum_{k=0}^{\infty} \frac{(-ig\tau)^{2k}}{(2k)!} \left(\hat{a}^\dagger\hat{a} + \left(\frac{\Delta}{2g}\right)^2\right)^k |g\rangle \\ &\quad - \sum_{k=0}^{\infty} \frac{(-ig\tau)^{2k+1}}{(2k+1)!} \left(\hat{a}^\dagger\hat{a} + \left(\frac{\Delta}{2g}\right)^2\right)^k \frac{\Delta}{2g}|g\rangle \\ &\quad + \sum_{k=0}^{\infty} \frac{(-ig\tau)^{2k+1}}{(2k+1)!} \left(\hat{a}\hat{a}^\dagger + \left(\frac{\Delta}{2g}\right)^2\right)^k \hat{a}|e\rangle. \end{aligned} \tag{5.23}$$

Using the series expansion for $\sin x = \sum \frac{(-1)^n}{(2n+1)!} x^{2n+1}$ and $\cos x = \sum \frac{(-1)^n}{(2n)!} x^{2n}$, this can be further simplified to

$$\begin{aligned}\exp\left(-ig\hat{H}_1\tau\right)|g\rangle \;=\; & \cos\left(g\tau\sqrt{\hat{a}^\dagger\hat{a}+\left(\frac{\Delta}{2g}\right)^2}\right)|g\rangle \\ & -i\frac{\Delta}{2g}\frac{\sin\left(g\tau\sqrt{\hat{a}^\dagger\hat{a}+\left(\frac{\Delta}{2g}\right)^2}\right)}{\sqrt{\hat{a}^\dagger\hat{a}+\left(\frac{\Delta}{2g}\right)^2}}|g\rangle \\ & -i\frac{\sin\left(g\tau\sqrt{\hat{a}\hat{a}^\dagger+\left(\frac{\Delta}{2g}\right)^2}\right)}{\sqrt{\hat{a}\hat{a}^\dagger+\left(\frac{\Delta}{2g}\right)^2}}\hat{a}|e\rangle. \end{aligned} \tag{5.24}$$

After taking the effect of the interaction Hamiltonian on the factorized total density matrix into account, we calculate the partial trace of the total density matrix with respect to the atomic degrees of freedom $\hat{\rho}_\mathrm{c}(t) = \mathrm{Tr}_\mathrm{a}\{\hat{\rho}_\mathrm{tot}(t)\}$. In the limit of small discrete time steps, this yields a differential equation, $\partial\hat{\rho}_c/\partial t$, from Eq. (5.10).

In addition to the resonant/near-resonant interaction with the atoms, the transmission-line resonator is also subject to dissipation. However, because of the small decay rate of the resonator with typical Q-factors of $\sim 10^6$ as has been shown in Chapter 4, this can be neglected if a comparitively short interaction time between a single atom and the resonator is considered. In this limit we can linearly add [20] the contribution of the resonator-dissipation due to its coupling to a thermal bath with temperature T,

$$\begin{aligned} D_\mathrm{th} =& \frac{\gamma}{2}\left[\bar{n}_\mathrm{r}(\omega_\mathrm{c},T)+1\right]\left(2\hat{a}\hat{\rho}_\mathrm{c}\hat{a}^\dagger-\hat{a}^\dagger\hat{a}\hat{\rho}_\mathrm{c}-\hat{\rho}_\mathrm{c}\hat{a}^\dagger\hat{a}\right) \\ & +\frac{\gamma}{2}\bar{n}_\mathrm{r}(\omega_\mathrm{c},T)\left(2\hat{a}^\dagger\hat{\rho}_\mathrm{c}\hat{a}-\hat{a}\hat{a}^\dagger\hat{\rho}_\mathrm{c}-\hat{\rho}_\mathrm{c}\hat{a}\hat{a}^\dagger\right), \end{aligned} \tag{5.25}$$

where γ is the photon dissipation rate of the resonator, to the equation of motion of the internal dynamics. This yields the master equation of the reduced density matrix of the resonator coupled to a beam of Rydberg atoms initially prepared in the circular ground state $|g\rangle$, and a thermal bath, which obtained to be

$$\begin{aligned}
\frac{d\hat{\rho}_{\mathrm{c}}}{dt} =& r\int d\tau P(\tau)\Big\{\cos\left(\frac{\tau}{2}\sqrt{4g^2\hat{a}^\dagger\hat{a}+\Delta^2}\right)\hat{\rho}_{\mathrm{c}}(t)\cos\left(\frac{\tau}{2}\sqrt{4g^2\hat{a}^\dagger\hat{a}+\Delta^2}\right)\\
&+\Delta^2\frac{\sin\left(\frac{\tau}{2}\sqrt{4g^2\hat{a}^\dagger\hat{a}+\Delta^2}\right)}{\sqrt{4g^2\hat{a}^\dagger\hat{a}+\Delta^2}}\hat{\rho}_{\mathrm{c}}(t)\frac{\sin\left(\frac{\tau}{2}\sqrt{4g^2\hat{a}^\dagger\hat{a}+\Delta^2}\right)}{\sqrt{4g^2\hat{a}^\dagger\hat{a}+\Delta^2}}\\
&+\mathrm{i}\Delta\frac{\sin\left(\frac{\tau}{2}\sqrt{4g^2\hat{a}^\dagger\hat{a}+\Delta^2}\right)}{\sqrt{4g^2\hat{a}^\dagger\hat{a}+\Delta^2}}\hat{\rho}_{\mathrm{c}}(t)\cos\left(\frac{\tau}{2}\sqrt{4g^2\hat{a}^\dagger\hat{a}+\Delta^2}\right)\\
&-\mathrm{i}\Delta\cos\left(\frac{\tau}{2}\sqrt{4g^2\hat{a}^\dagger\hat{a}+\Delta^2}\right)\hat{\rho}_{\mathrm{c}}(t)\frac{\sin\left(\frac{\tau}{2}\sqrt{4g^2\hat{a}^\dagger\hat{a}+\Delta^2}\right)}{\sqrt{4g^2\hat{a}^\dagger\hat{a}+\Delta^2}}\\
&+4g^2\frac{\sin\left(\frac{\tau}{2}\sqrt{4g^2\hat{a}\hat{a}^\dagger+\Delta^2}\right)}{\sqrt{4g^2\hat{a}\hat{a}^\dagger+\Delta^2}}\hat{a}\hat{\rho}_{\mathrm{c}}(t)\hat{a}^\dagger\frac{\sin\left(\frac{\tau}{2}\sqrt{4g^2\hat{a}\hat{a}^\dagger+\Delta^2}\right)}{\sqrt{4g^2\hat{a}\hat{a}^\dagger+\Delta^2}}\Big\}-r\hat{\rho}_{\mathrm{c}}(t)\\
&+\frac{\gamma}{2}\left[\bar{n}_{\mathrm{r}}(\omega_{\mathrm{c}},T)+1\right]\left(2\hat{a}\hat{\rho}_{\mathrm{c}}\hat{a}^\dagger-\hat{a}^\dagger\hat{a}\hat{\rho}_{\mathrm{c}}-\hat{\rho}_{\mathrm{c}}\hat{a}^\dagger\hat{a}\right)\\
&+\frac{\gamma}{2}\bar{n}_{\mathrm{r}}(\omega_{\mathrm{c}},T)\left(2\hat{a}^\dagger\hat{\rho}_{\mathrm{c}}\hat{a}-\hat{a}\hat{a}^\dagger\hat{\rho}_{\mathrm{c}}-\hat{\rho}_{\mathrm{c}}\hat{a}\hat{a}^\dagger\right).
\end{aligned} \tag{5.26}$$

The probability distribution $P(\tau)$ represents the disitribution of interaction times that arise because the atoms do not all move with the same velocity across the resonator. Therefore we have to integrate over all possible interaction times weighted by their probility of occurance, $P(\tau)$.

While the first two terms in the integral kernel describe the excitation of the resonator state due to the interaction with the atomic beam, the third and fourth part show the effect of the accumulation of phase differences between each resonator state resulting from this interaction. The fifth, and last, term describes the coherent decay of the resonator state $|n+1\rangle$ to $|n\rangle$ as the atoms in their ground state are excited and subsequently carry away the excitation. This coherent atom-resonator interaction can be exploited to remove photons from a selected resonator mode, effectively cooling the resonator. The factors in the last two lines in Eq. (5.26) are the Lindblad operators accounting for the thermal decay and heating processes affecting the resonator because of its coupling to the environment, e.g. a waveguide to connect the resonator to a measurement device, as described in Chapter 4.

5.2 Resonator De-Excitation

In the hybrid quantum electrodynamics experiments with gas-phase Rydberg atoms and microwave circuits pertaining to the work here, it is of interest to de-populate a selected resonator mode and consequently lower the resonator's effective temperature. The goal of such a cooling process is to establish a non-equilibrium steady-state between the atomic beam carrying away excitations from the resonator and the heating due to the coupling to the local environment via a waveguide. This method of resonator cooling is expected to be achievable experimentally because many of the individual components necessary to realize this proposed scheme are already in place [66, 67, 51].

To investigate this approach to resonator cooling it is necessary to characterize the probability of the population of each Fock state in the resonator, $p(n)$. This is done by considering the diagonal elements of the reduced density matrix in the photon number basis, $p(n) = \rho_{nn} = \langle n|\hat{\rho}|n\rangle$. For this treatment, and without loss if generality, we assume that interaction times of the individual atoms in the beam with the resonator mode of interest follow a Gaussian distribution, $P(\tau)$, centered on an average interaction time $\bar{\tau}$, such that

$$P(\tau) = \frac{1}{\sqrt{2\pi\sigma^2}} e^{-\frac{(\tau-\bar{\tau})^2}{2\sigma^2}}. \tag{5.27}$$

The time-evolution of these probabilities in the combined atom-resonator system is described by a set of coupled differential equations of the form

$$\dot{p}(n) = A_n p(n) + B_{n+1} p(n+1) + C_{n-1} p(n-1), \tag{5.28}$$

where the prefactors are evaluated [17] to be

$$A_n = \underbrace{r\left[\frac{2g^2 n + \Delta^2 + 2g^2 n\, \mathrm{e}^{-\frac{1}{2}\sigma^2\left(4g^2 n+\Delta^2\right)} \cos\left(\bar{\tau}\sqrt{4g^2 n+\Delta^2}\right)}{4g^2 n + \Delta^2} - 1\right]}_{A_n(r)} - \underbrace{\gamma\Big[(2\bar{n}_T + 1)\, n + \bar{n}_T\Big]}_{A_n(\gamma)}, \tag{5.29}$$

$$B_n = r\,\frac{2g^2 n\left(1 - \mathrm{e}^{-\frac{1}{2}\sigma^2\left(\Delta^2+4g^2 n\right)} \cos\left(\bar{\tau}\sqrt{4g^2 n+\Delta^2}\right)\right)}{4g^2 n + \Delta^2} + \gamma\,(\bar{n}_T + 1)\, n, \tag{5.30}$$

$$C_n = \gamma \bar{n}_T (n+1). \tag{5.31}$$

These prefactors can be interpreted as rates describing the transitions between different Fock states of the resonator. As depicted in Fig. 5.1, B_n corresponds to the rate of depopulation of the selected resonator mode because of the interaction with the atomic beam, i.e., $B_n \propto r$, and the decay

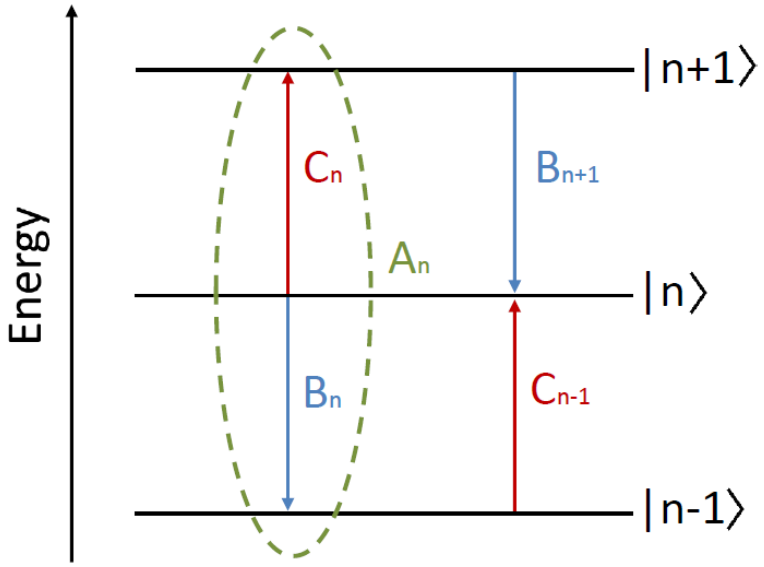

Figure 5.1: The population transfer rates A_n, B_n and C_n among three consecutive Fock states in the resonator. It can be seen that B_n corresponds to a de-excitation of the resonator from the Fock state $|n\rangle$ to the Fock state $|n-1\rangle$, whereas C_n describes an excitation from the state $|n\rangle$ to the state $|n+1\rangle$. The total rate of de-population of the Fock state $|n\rangle$ is therefore $A_n = B_n + C_n$. Together with the competing transfer rates B_{n+1} and C_{n-1} populating the $|n\rangle$ Fock state, the rate of change of the population of that state $|n\rangle$ can be calculated according to Eq. (5.28).

of the resonator photons into the waveguide, i.e., $B_n \propto \gamma$. The effective resonator cooling rate results from the competition between B_n and C_n, which represents the excitation of the resonator by thermal photons entering it from the waveguide. The set of coupled differential equations described in Eq.(5.28) can be written in matrix form as

$$\dot{\mathbf{p}}(t) = \mathbf{M}\mathbf{p}(t), \tag{5.32}$$

where $\mathbf{p}(t)$ is a vector, the elements of which correspond to the occupation probability of the respective Fock state, and $\mathbf{M}$ is the corresponding matrix containing the transfer rates, i.e.,

$$\mathbf{p}(t) = \begin{pmatrix} p_0(t) \\ p_1(t) \\ p_2(t) \\ p_3(t) \\ \vdots \\ p_{n-2}(t) \\ p_{n-1}(t) \\ p_n(t) \end{pmatrix}, \quad \mathbf{M} = \begin{pmatrix} A_0 & B_1 & & & & & & \\ C_0 & A_1 & B_2 & & & & & \\ & C_1 & A_2 & B_3 & & & 0 & \\ & & C_2 & A_3 & B_4 & & & \\ & & & & \ddots & & & \\ & 0 & & & C_{n-3} & A_{n-2} & B_{n-1} & \\ & & & & & C_{n-2} & A_{n-1} & B_n \\ & & & & & & C_{n-1} & A_n \end{pmatrix}, \tag{5.33}$$

with the general solution

$$\mathbf{p}(t) = \mathbf{p}_{ss} + \mathrm{e}^{\mathbf{M}t} \left[\mathbf{p}(0) - \mathbf{p}_{ss} \right]. \tag{5.34}$$

This depends on the non-equilibrium steady state solution $\mathbf{p}_{ss}$, which is the state the system ends up in as $t \to \infty$, and on the initial state of the resonator $\mathbf{p}(0)$, which is generally assumed to be the thermal state of the system under consideration being in thermal equilibrium with the local environment.

5.2.1 Steady State Solution

We first solve for the steady state, i.e., the resonator mode of interest in dynamic equilibrium resulting from the competing processes of the introduction of photons from the thermal bath, and excitations being carried away by the atoms. The probability of zero photons in the resonator can be obtained analytically

$$p_0 = \left(\sum_{n=1}^{\infty} \prod_{x=1}^{n} \frac{\gamma \bar{n}_T \left(4g^2 x + \Delta^2\right)}{2g^2 r \left(1 - \mathrm{e}^{-\frac{1}{2}\sigma^2\left(\Delta^2 + 4g^2 x\right)} \cos\left(\bar{\tau}\sqrt{4g^2 x + \Delta^2}\right)\right) + \gamma\left(\bar{n}_T + 1\right)\left(4g^2 x + \Delta^2\right)} + 1 \right)^{-1}. \tag{5.35}$$

The steady state photon number distribution in the transmission line resonator can be calculated via the recursive relation

$$p_n = p_0 \prod_{j=1}^{n} \frac{C_{j-1}}{B_j}. \tag{5.36}$$

Considering the $|n = 70\rangle \leftrightarrow |n = 71\rangle$ transition between the circular Rydberg states, which occurs at a transition frequency of $\nu = 18.78$ GHz, a resonator coupling strength of $g/(2\pi) = 4.25$ MHz is assumed. This is experimentally achievable for Rydberg atoms positioned at a distance of 10 μm above the center conductor [80].

The assumed resonator's quality factor of $Q \leq 10^6$ leads to a dissipation rate of $\gamma \geq 20$ kHz. Note that currently experimentally achievable quality factors for the here given initial temperature $T = 4$ K of the resonator are on the order of $Q \lesssim 10^5$ [8] because the condition for the resonator material to be fully superconducting, $T_c \ll T$, is not fulfilled at this temperature.

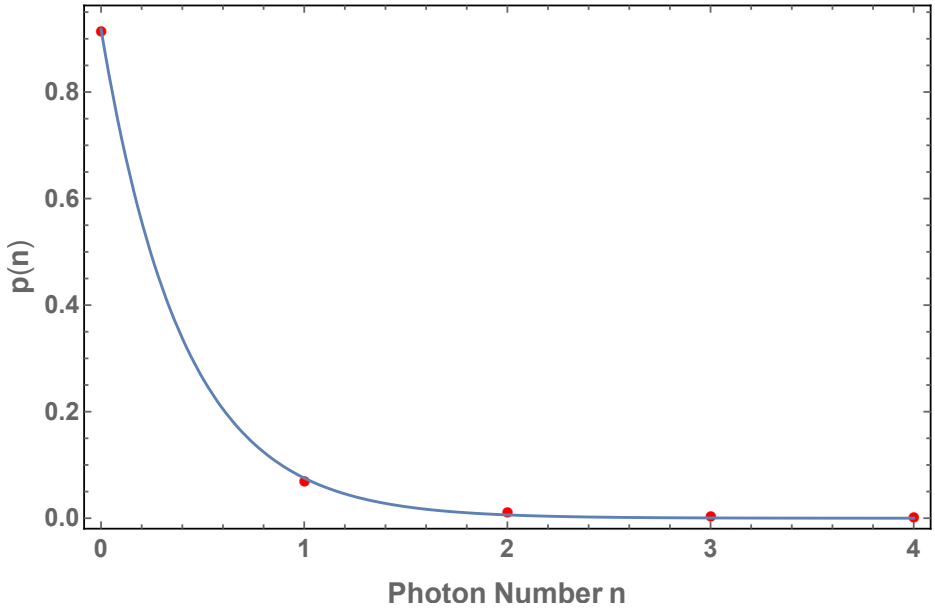

Figure 5.2: Distribution of the photon occupation number for a fundamental frequency of $\nu = 18.78$ GHz. The red dots mark the occupation probability of the Fock state $|n\rangle$ of the resonator in the non-equilibrium steady state. The Planck distribution for an effective temperature $T_{\text{eff}} = 360$ mK is plotted (blue line), showing the qualitative fit with the steady state photon distribution.

Assuming an average interaction time of the atoms with the resonator of $\bar{\tau} = 50$ns, there are two distinct cases to be considered. First a coherent beam of atoms is considered, where the atomic velocities are all equal, and therefore their interaction time distribution can be modelled by a dirac delta function $P(\tau) = \delta(\tau - \bar{\tau})$ with

$$\delta(\tau - \bar{\tau}) = \begin{cases} +\infty, & \tau = \bar{\tau} \\ 0, & \tau \neq \bar{\tau}. \end{cases} \tag{5.37}$$

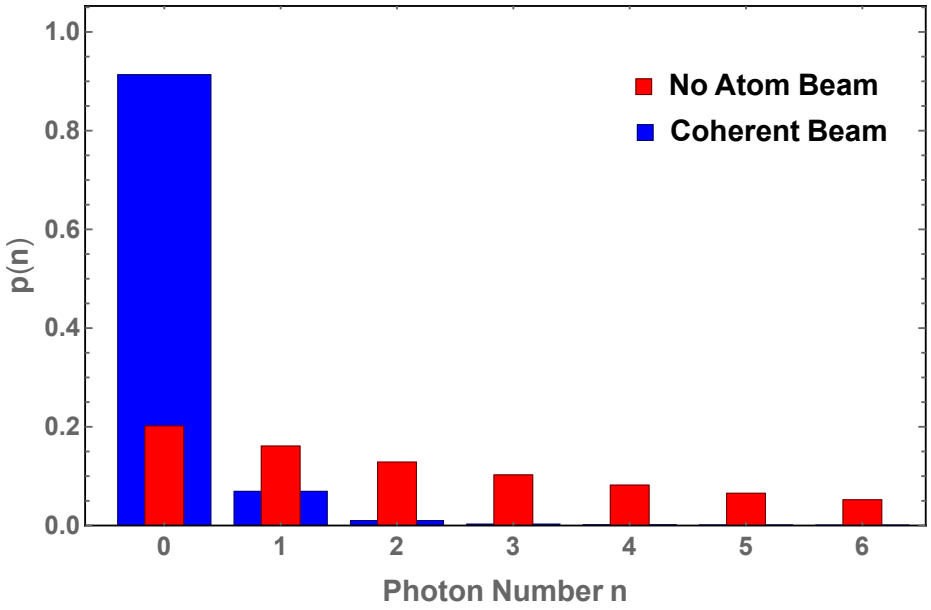

Figure 5.3: Depletion of the fundamental mode of the resonator. The thinner red bars represent the occupation probability distribution of the Fock states $|n\rangle$ at $T = 4$ K. This results in an average photon occupation number of $\langle n\rangle_{\text{th}} = 3.96$. The thicker blue bars represent the photon number distribution after the interaction with an atomic beam with a fixed atom-resonator interaction time $\bar{\tau}$, leading to a thermal photon number distribution with an average number of photons $\langle n\rangle_{\text{ss}} = 0.122$.

For the case in which the atomic transition frequency is resonant with the fundamental mode of the resonator, i.e. $\Delta = 0$, we calculate the photon number probability distribution in the nonequilibrium steady state. Assuming an atomic rate of $r = 10^6$ atoms per second, the Fock state occupation probability follows a thermal photon number disitribution for this selected mode, as can be seen in Fig. 5.2. Therefore, a fitted parameter

representing the effective temperature of the resonator T_{eff} [93]

$$p_{\text{th}}(n) = \frac{1}{\langle n\rangle_{\text{th}} + 1}\left(\frac{\langle n\rangle_{\text{th}}}{\langle n\rangle_{\text{th}} + 1}\right)^{n}, \tag{5.38}$$

where

$$\langle n\rangle_{th} = \frac{1}{\exp\left(\frac{h\nu}{k_{\text{B}}T_{\text{eff}}}\right) - 1}. \tag{5.39}$$

is introduced. From this calculation, it can be seen in Fig. 5.3 that the average number of photons, and thus the effective temperature, of a selected resonator mode can be reduced significantly by coupling the resonator to a continuous beam of flying atoms. The initial state of the resonator when cooled cryogenically using liquid helium may be described by the thermal photon number distribution at $T = 4$ K, as indicated by the red bars in Fig. 5.3. The average number of photons contained in the resonator is therefore $\langle n\rangle_{\text{th}} = 3.96$. After allowing atoms, prepared in the lower circular Rydberg state, to cross the resonator at a rate $r = 10^6$ s^{-1}, this average photon number can be reduced since the atoms will continuously carry away excitations. Assuming a coherent atomic beam with a constant interaction time τ, the average number of photons in the non-equilibrium steady state can be reduced to $\langle n\rangle_{\text{ss}} = 0.122$, corresponding to an effective temperature of the resonator of $T_{\text{eff}} = 0.36$ K. This method of cooling a selected resonator mode depends on several experimental parameters that affect its efficiency. These are studied here to identify optimal experimental conditions under which to implement this cooling process. In doing this, the fidelity of the vacuum state of the resonator, $\mathcal{F}_0 = \langle 0|\hat{\rho}|0\rangle$, is calculated. This fidelity is assumed to be a valid measure of the resonator de-excitation.

First, the dependence of the ground state fidelity on the detuning of the atomic transition frequency from the frequency of the fundamental mode

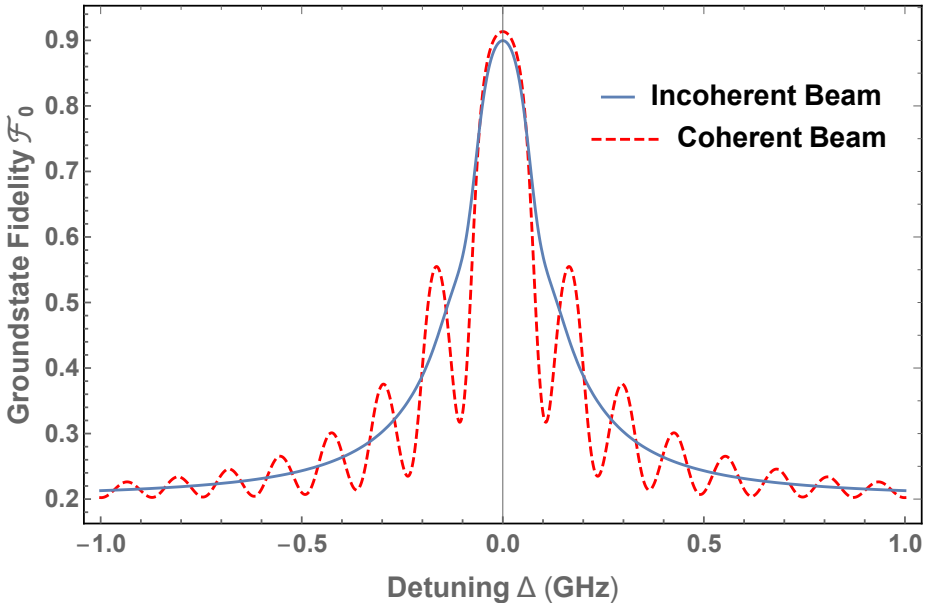

Figure 5.4: The dependence of the $|0\rangle$ Fock state fidelity on the detuning of the atomic transition frequency and the resonator resonance frequency of the selected fundamental mode.

of the resonator is investigated. The observed behavior, which can be seen in Fig. 5.4, is strongly dependent on the velocity distribution of the atomic beam. As can be seen in the figure, for the case of a coherent beam of atoms that has been considered up to now, for which the interaction time of the atoms with the resonator is assumed to be constant, the dependence of the ground state fidelity on the detuning is described by the Fourier transform of a square signal pulse.

The alternative case, also considered in Fig. 5.4, is that of an incoherent beam of atoms, in which the interaction times follow a normal distribution with a broad width, chosen here to be $\sigma = \bar{\tau}/3$. Since 99.7% of all values lie within three times the standard deviation, this assumption ensures that only 0.15% of all possible values for the individual interaction time

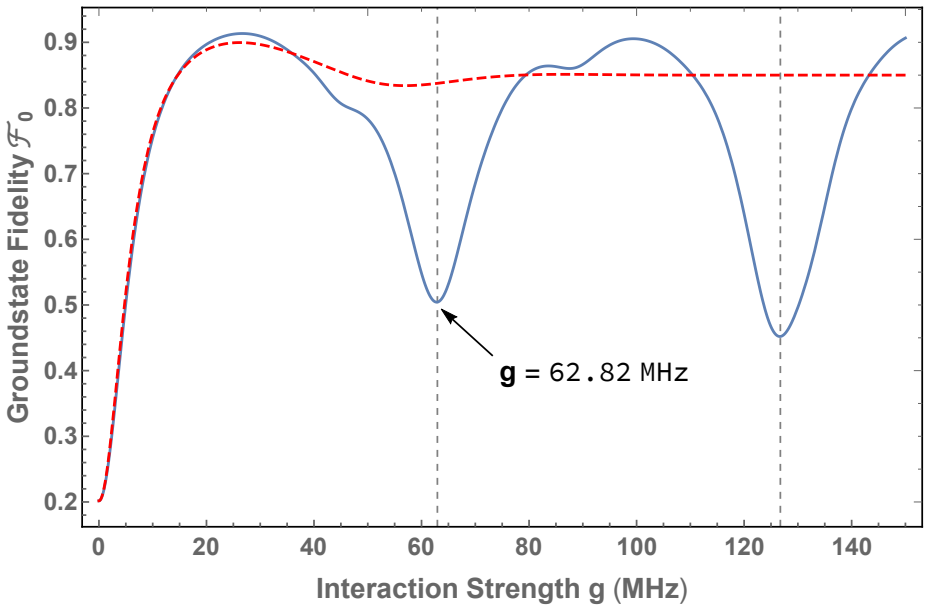

Figure 5.5: The dependence of the resonator ground state fidelity on the atom-resonator coupling strength. A coherent beam (solid blue line) reaches local minima for specific values of the interaction strength, one being at $g = 62.82$ MHz. The minima represent trapping states. The incoherent atomic beam (dashed red line) does not exhibit such behavior, with a roughly constant fidelity of $\mathcal{F}_0 \approx 0.85$ for values of $g \geq 80$ MHz.

of each atom with the resonator are mathematically $\tau \leq 0$, and hence not physical, justifying the assumption of such a probability distribution. The corresponding calculation for this case shows that the dependence of the ground state fidelity on the atom-resonator detuning follows a Lorentzian function. This is the Fourier transform of an exponential signal. One can therefore postulate that measuring the dependence of the ground state fidelity on the detuning can, for example, provide information on the interactions between the atoms and the resonator and thus about the velocity distribution of a given beam of atoms.

Second, the ground state occupation probability of the resonator is investigated as the coupling strength between the Rydberg atoms and the microwave resonator is adjusted. In this case the observed behavior shows a fundamental difference between a coherent and incoherent beam of atoms. The former exhibits the existence of trapping states [77], because the constant interaction time leads to situations in which the average photon number in the resonator approximately fulfills the condition for a full Rabi cycle for all atoms,

$$g\tau\sqrt{\langle n\rangle} \approx 2\pi \cdot k, \tag{5.40}$$

where $k \in \mathbb{N}$. This renders the preparation of the vacuum state of the resonator highly inefficient because ground state atoms entering the resonator will leave the resonator again when being close to the ground state, and thus do not carry away any significant amount of resonator excitations. The photon number distribution of this anomalous steady state for an atom-resonator coupling value of $g = 62.82$ MHz is compared to that for a thermal state with the same average photon number $\langle n\rangle$ in Fig. 5.6. The non-equilibrium steady state achieved in this way is almost entirely an even statistical mixture between the $|0\rangle$ and $|1\rangle$ Fock states, where $p(n = 0) \approx 0.5$ and $p(n = 1) \approx 0.4$, with the occupation probability of other states being $\sum_{n=2} p(n) \lesssim 10\%$. This shows the possibility of controlled state preparation of the resonator by choosing appropriate experimental parameters. In the latter case of an incoherent atomic beam, however, such trapping states are not observed. Due to the wide spread, $\sigma = \bar{\tau}/3$, in interaction times, instances for which the average number of photons enhancing the interaction strength leads to a full Rabi oscillation do not occur for a consid-

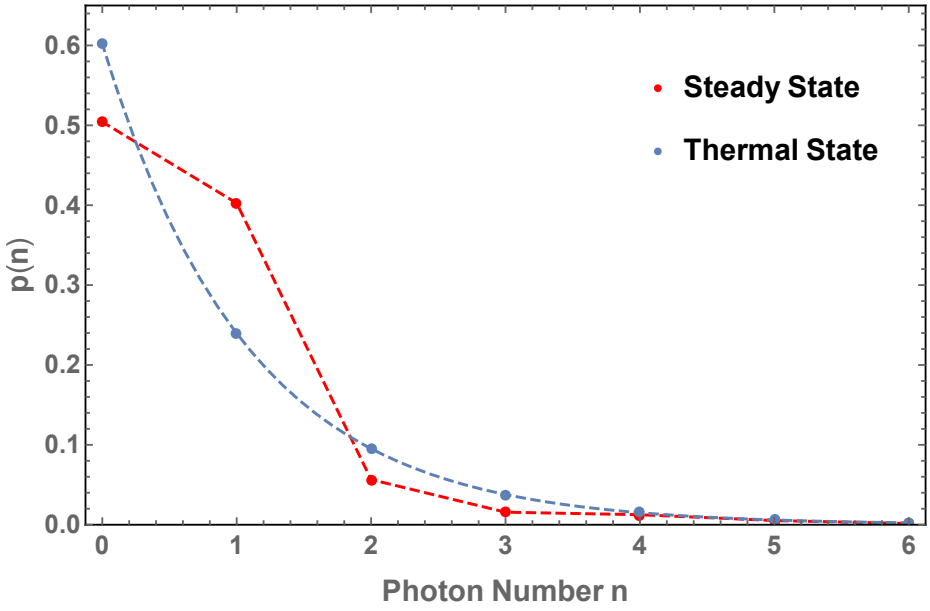

Figure 5.6: Photon number distribution corresponding to the annomalous trapping state that arrises for an atom-resonator coupling strength of $g = 62.82$ MHz.

erable amount of atoms whose interaction times differ significantly from the mean value $\bar{\tau} = 50$ ns. The interactions of these atoms eventually carry away excitations leading to a dephasing of these trapping states. It should be mentioned here that the observation of such trapping states would require experimtal developments beyond those currently realized for hybrid cavity QED with circular Rydberg states coupling to transmission line resonators.

As previously mentioned, another important experimental factor affecting the efficiency of the de-excitation of the resonator is its quality factor. The dependence of the average number of photons in the non-equilibrium steady state is plotted in Fig. 5.7. It illustrates the high sensitivity of the average steady state photon number on the change in quality factors between

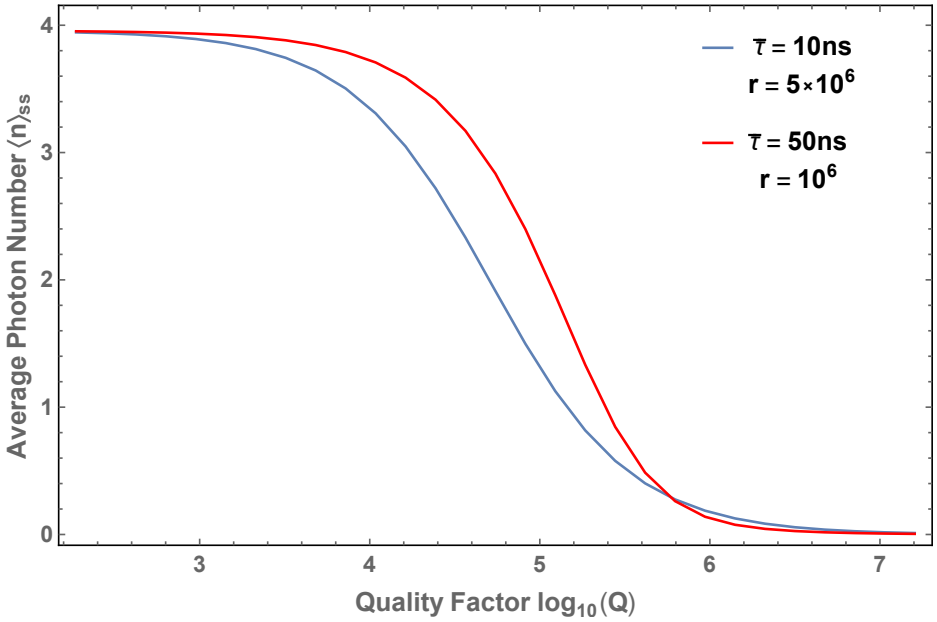

Figure 5.7: The dependence of the steady state average photon number ,$\langle n \rangle_{ss}$, on the resonator quality factor, Q. The product $r\tau \ll 1$ ensures the approximation of at most one atom interacting with the resonator is fulfilled.

$Q = 10^4$ and $Q = 10^6$. Significant de-excitation to a steady state average photon number of $\langle n \rangle_{ss} \leq 0.5$ can be achieved with the here proposed method for a quality factor of $Q \geq 5 \cdot 10^5$.

The final state of the resonator after the interaction with the atomic beam is a non-equilibrium steady state which is determined by the competing processes between the thermal heating of the resonator, which is caused by the introduction of photons from the thermal bath at $T = 4$K, and the rate at which atoms carry away excitations. This leads to a detailed balance for a specific average photon number $\langle n \rangle$ in the resonator. Therefore, the rate at which atoms cross the resonator, r, is the main experimentally controllable

parameter that has to be studied in order to optimize the efficiency of populating the vaccuum state of the resonator. Phenomenologically, the more excitations that can be carried away before a thermal photon re-enters into the resonator due to its coupling to the environment, the lower the final effective temperature that can be achieved. Fig. 5.8 shows the exponential relationship between the average photon number in the steady state, $\langle n \rangle_{ss}$, and the rate at which the atoms cross the resonator. From this figure it can be seen that the higher the atomic beam rate, the more efficient the cooling process. This behavior is qualitatively similar for different average interaction times $\bar{\tau}$. However, the region in Fig. 5.8 in which the results are indicated by the dashed curves are beyond the limits of the approximation made in the calculation. These graphs therefore only give an indication of the powerful effective cooling that may be studied if the calculations are extended beyond the one-atom approximation made in this chapter.

If the atomic beam is replaced with a dense pulsed beam for which the calcuations need to allow for more than one atom interacting with the resonator at the same time, we expect that it will be possible to prepare the resonator at much lower effective temperatures which will persist for a sufficient period of time to allow strong coupling experiments with much less than 1 thermal photon present in the resonator. This is the case that will be considered numerically in Chapter 6.

5.2.2 Time-Resolved Solution

In order to obtain a realistic estimate of how long it takes for a system being cooled by an atomic beam to reach its steady state using this approach,

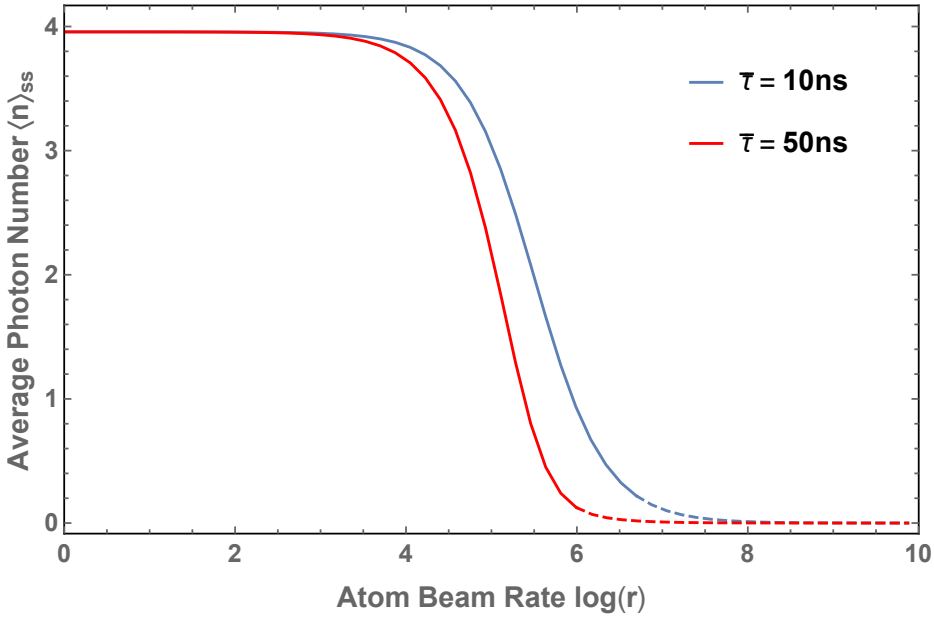

Figure 5.8: Dependence of the average photon number $\langle n \rangle$ of the nonequilibrium steady state of the resonator on the rate of atoms crossing the resonator with different average interaction times $\bar{\tau}$ as indicated. The continuous curves represent the values for r that fulfill the approximation $r\tau \ll 1$, where the probability of having two or more atoms interact with the resonator at the same is less than 0.25%. The dashed curves represent the region in which this approximation breaks down because the probability that two or more atoms interact with the resonator at the same time is not negligible anymore.

we obtain a time-dependent solution of Eq. (5.34). The matrix $\mathbf{M}$ in this equation is a tridiagonal matrix. A useful property of such matrices is that

$$\mathbf{M}_{n,n+1}\mathbf{M}_{n+1,n} = B_{n+1}C_n \geq 0, \tag{5.41}$$

which guarantees their eigenvalues to be real.

The elements of $\mathbf{M}$ in Eq.(5.33) can be expressed as

$$\mathbf{M}_{n,m} = \delta_{n,m} A_n + \delta_{n,m+1} C_{n-1} + \delta_{n,m-1} B_{n+1}. \tag{5.42}$$

Since the steady-state of a system is defined as being unchanged under the evolution over time, the application of the matrix generating the dynamics of the system in the steady-state is $\mathbf{M}\mathbf{p}_{ss} = \mathbf{0}$, which we can use to obtain

$$\begin{aligned} \dot{\mathbf{p}}(t) &= \mathbf{M}\mathbf{p}(t) \\ &= \mathbf{M}\mathbf{p}(t) - \mathbf{M}\mathbf{p_{ss}}, \end{aligned} \tag{5.43}$$

or equivalently

$$\dot{\mathbf{p}}(t) = \mathbf{M}\left(\mathbf{p}(t) - \mathbf{p}_{ss}\right). \tag{5.44}$$

This leads to the solution

$$\mathbf{p}(t) = \mathbf{p}_{ss} + \mathrm{e}^{\mathbf{M}t}\left[\mathbf{p}(0) - \mathbf{p}_{ss}\right], \tag{5.45}$$

where the matrix exponential must be calculated using $\mathrm{e}^X = \sum_{k=0}^{\infty} \frac{1}{k!} X^k$. This calulation can be carried out by diagonalizing the matrix $\mathbf{M}$ according to $\mathbf{D} = \mathbf{U}\mathbf{M}\mathbf{U}^{-1} \rightarrow \mathrm{e}^{\mathbf{D}} = \mathbf{U}\mathrm{e}^{\mathbf{M}}\mathbf{U}^{-1}$, where $\mathbf{U}$ is a block matrix containing the eigenvectors of $\mathbf{M}$, allowing for a unitary transformation of the matrix, and $\mathbf{D}$ is a diagonal matrix containing the corresponding (negative) eigenvalues.

It can be shown that the solution obtained in this way is valid, since the derivative of Eq. (5.34) is

$$\begin{aligned} \dot{\mathbf{p}}(t) &= \mathbf{M}\underbrace{\left(\mathrm{e}^{\mathbf{M}t}\left[\mathbf{p}(0) - \mathbf{p}_{ss}\right] + \mathbf{p}_{ss}\right)}_{=\mathbf{p}(t)} - \underbrace{\mathbf{M}\mathbf{p}_{ss}}_{=\mathbf{0}} \\ &= \mathbf{M}\mathbf{p}(t), \end{aligned} \tag{5.46}$$

and therefore a solution to Eq. (6.1).

The reason to incorporate $\mathbf{p}_{ss}$ into this solution, even though in the problem it simply means adding a zero vector, $\mathbf{0}$, is that it is necessary to ensure that a non-trivial steady-state solution exists. Without including the steady-state vector, any solution generated is going to produce a trivial steady-state solution $\mathbf{p}_{ss} = \mathbf{0}$. However, because all the eigenvalues of $\mathbf{M}$ are real and negative, as shown above, a unique and stable solution of the system's state must exist [105]. Hence, by finding any solution by solving the equation of motion, given its initial state at $t = 0$ and resproducing its steady-state for $t \to \infty$, we have found the unique solution to the problem. Since we assume that the initial state $\mathbf{p}(0)$ respresents the thermal distribution of the resonator mode at time $t = 0$, and the steady-state solution $\mathbf{p}_{ss}$ is readily calculated as seen in the previous section, the full solution of $\mathbf{p}(t)$ at all times t can be obtained.

As can be seen from the previous investigation of the experimental parameters, the most effective cooling is achieved for zero detuning, i.e., $\Delta = 0$, and a coherent beam of atoms, so that

$$A_n = \frac{r}{2}\left[\cos\left(2g\bar{\tau}\sqrt{n}\right) - 1\right] - \gamma\left[(2\bar{n}_T + 1)\, n + \bar{n}_T\right], \tag{5.47}$$

$$B_n = -\frac{r}{2}\left[\cos\left(2g\bar{\tau}\sqrt{n}\right) - 1\right] + \gamma\,(\bar{n}_T + 1)\, n, \tag{5.48}$$

$$C_n = \gamma\bar{n}_T(n + 1). \tag{5.49}$$

The time evolution of the average photon number of the resonator is plotted in Fig. 5.9. The non-equilibrium steady state with $\langle n\rangle_{\mathrm{ss}} = 0.122$ is reached within approximately 100 μs.

After having cooled the system close to its steady-state, it is also of interest

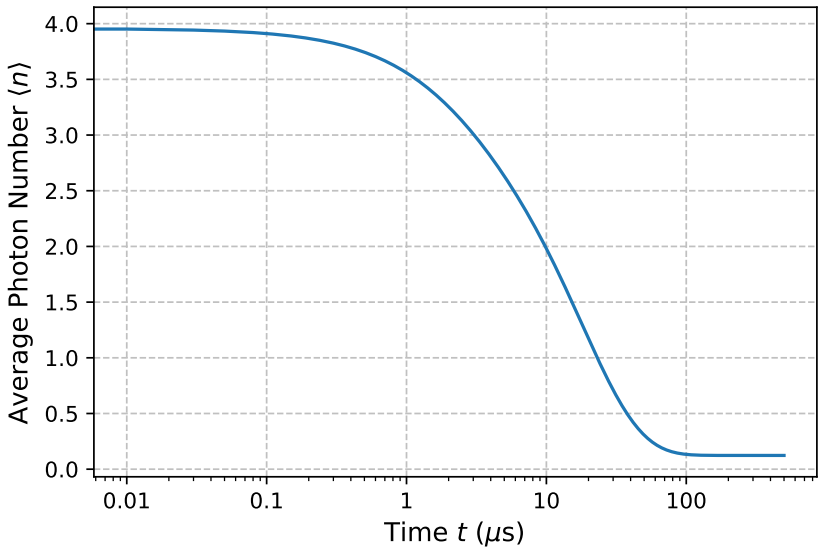

Figure 5.9: Time-dependent evolution of the average photon number $\langle n \rangle$ of the resonator. The initial state of the resonator with a fundamental frequency of $\nu = 18.78$ MHz is assumed to be a thermal state at $T_{\text{env}} = 4$ K. The atoms on resonance, $\Delta = 0$, cross the resonator at a rate $r = 10^6$ s^{-1} and couple to it for a constant interaction time $\bar{\tau} = 50$ ns with a coupling strength $g = 26.66$ MHz.

to know how quickly the system heats up again after the atomic beam is switched out of resonance, which is accounted for by changing the parameter $r = 0$. This is the time during which, in principle, experiments with an initially empty resonator could be performed. In Fig. 5.10 it can be seen that for a time $t \lesssim 5\mu$s the resonator contains less than $\langle n \rangle = 0.5$ photons. This is sufficient to perform gate operations within the context of this experimental setup.

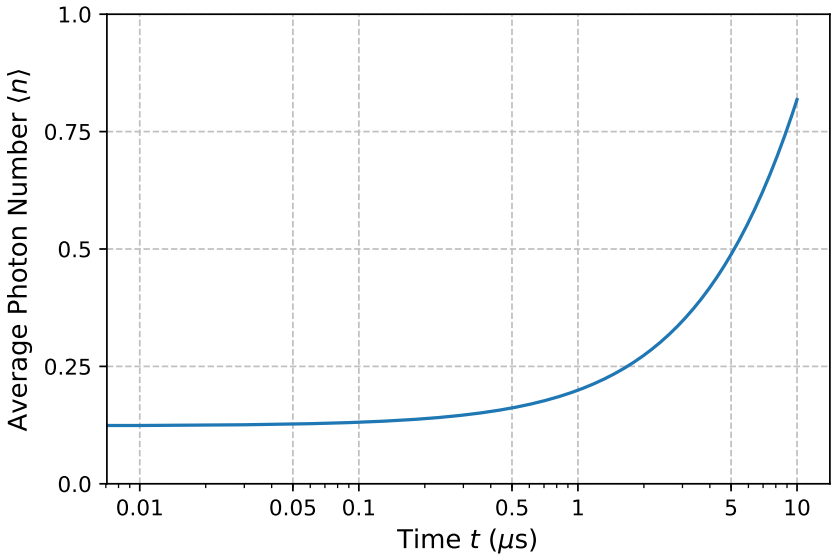

Figure 5.10: Time resolved reheating of the resonator.

It is important to note that the result arrived at in this chapter requires restricting the calculations to at most one atom interacting with the resonator at any time. This is a significant limitation of the cooling process. Once the atomic rate r grows so high that the probability of two or more atoms interacting with the resonator at the same time cannot be neglected, our calculation must be modified.

Chapter 6

Atomic Beam Interaction: Numerical Approach

The analytical approach to investigating the cooling of selected resonator modes using beams of Rydberg atoms presented in Chapter 5 provides and accurate description of the dynamics of the system when there is at most one atom interacting with the resonator. However, this restriction on the number of interacting atoms places a limit on the rate, r, at which atoms can cross the resonator and in turn limits the effective cooling of the microwave resonator's fundamental frequency mode.

To extend the analysis of the proposed hybrid system beyond this limit, we develop a numerical approach in this chapter that allows several atoms to interact with the microwave resonator at the same time, as illustrated in Fig. 6.1, permitting access to a parameter range that leads to much more efficient cooling of the resonator mode.

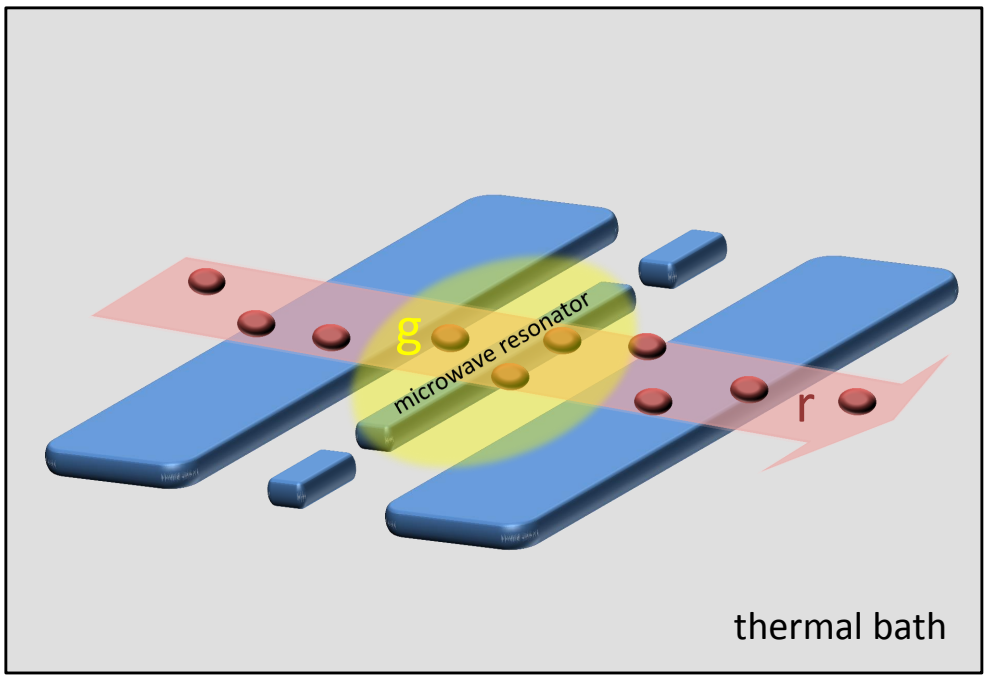

Figure 6.1: A schematic diagram of the experimental setup, allowing for more than one atom to interact with the microwave resonator at any given time t.

6.1 Modeling the Beam of Atoms

In order to numerically model a realistic experimental setting, it is necessary to account for random arrival times of atoms at the microwave resonator. This in turn leads to a random number of atoms interacting with the microwave resonator at any given time. To study the time-evolution in this situation, the dynamics are investigated in very small time steps. After each such time step, Δt, the probabilty of a new number n atoms arriving at the resonator is calculated, as well as the probabilty of any atom that

has been interacting with the resonator during that time step to leave the resonator. A sketch of the algorithm created to model such behavior is shown in Fig. 6.2.

The probability of one atom interacting with the resonator within each time step can be expressed as

$$P(\Delta t) = r \cdot \Delta t, \tag{6.1}$$

where r is the rate of atoms crossing the resonator per unit time, and Δt is the time step size.

In principle this probability $P(\Delta t)$ can be infinitely large, as the time step is arbitrarily chosen. However, over the duration T of an experiment, which covers N time steps, this effect is canceled out if the rate r is uniformly distributed, and therefore constant, during the experiment. This can be seen shown by

$$\begin{aligned} \bar{N}_{atoms} &= \int_0^T r \, dt \\ &= \int_0^{T/N} r \, dt + \int_{T/N}^{2T/N} r \, dt + \ldots + \int_{(N-1)T/N}^{T} r \, dt \\ &= N \underbrace{\int_0^{T/N} r \, dt}_{=P(\Delta t)} \\ &= r \cdot T, \end{aligned} \tag{6.2}$$

where N time steps occur with intervals $\Delta t = T/N$. The probability of an atom interacting with the resonator during each time step is given in Eq. (6.1). Following from this definition of the probability of a single atom arriving at the resonator, we can extend this to the probability of two, three

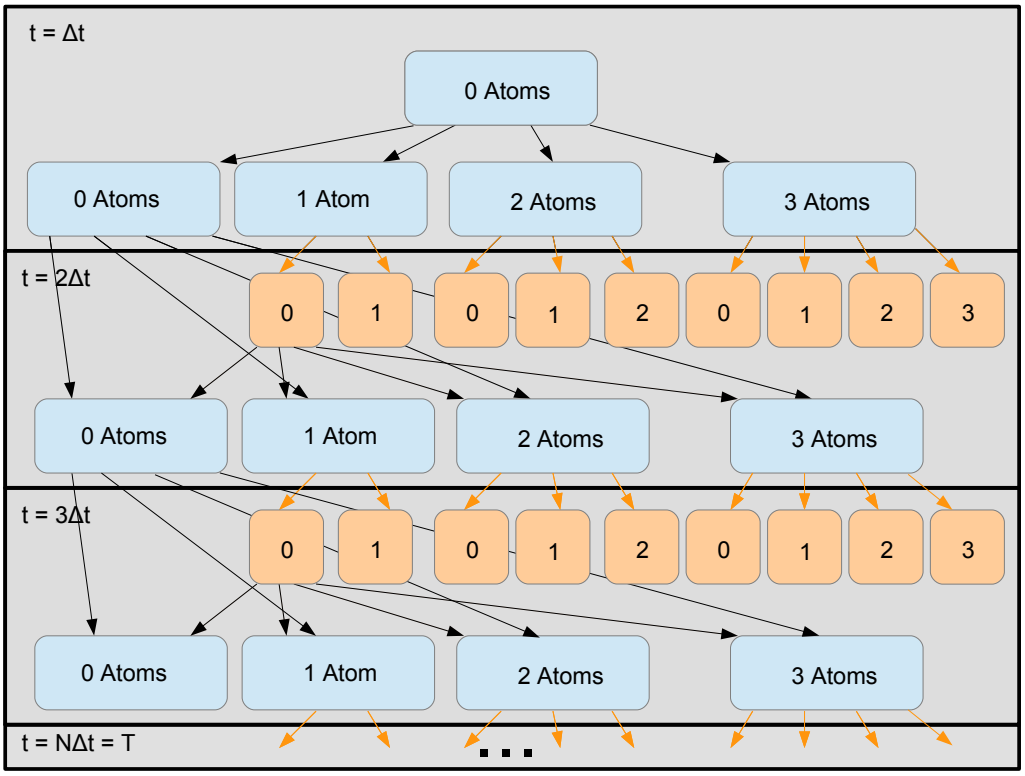

Figure 6.2: The flow chart of the numerical approach. Within each time step Δt the number of atoms leaving the microwave resonator is calculated (orange arrows) after having interacted over a time t_{int}. This depends on how many atoms remain within the resonator, and how many new atoms enter the microwave resonator (black arrows), based on their arrival probability $P_n(\Delta t)$. The black arrows from subsequent orange atom number boxes, have been omitted for clarity of the sketch.

or even n atoms arriving at the same time as

$$P_n(\Delta t) = (r \cdot \Delta t)^n, n \geq 1. \tag{6.3}$$

Therefore we need to estimate the error resulting from the need to introduce a limit on the maximum number of atoms considered to simultaneously interact with the microwave resonator at any given time step to ensure

computational feasibility. To obtain an order of magnitude estimate of the error, we compare the exact probability of zero atoms arriving at the resonator $P_0(\Delta t)$ within a given time step to the probability based upon the above approximation.

1. Exact:

$$\begin{aligned} P_0(\Delta t) &= 1 - \sum_{k=1}^{\infty} (r\Delta t)^k \\ &= \frac{1 - 2r\Delta t}{1 - r\Delta t}. \end{aligned} \tag{6.4}$$

2. Truncation to N atoms:

$$\begin{aligned} P_0(\Delta t) &\approx 1 - \sum_{k=1}^{N} (r\Delta t)^k \\ &= \frac{1 - 2r\Delta t}{1 - r\Delta t} + \epsilon. \end{aligned} \tag{6.5}$$

The sums in Eq.(6.4) and (6.5) are solved as converging geometric series for $r\Delta t < 1$. The error resulting from the truncation that arises from the consideration of at most N atoms interacting with the microwave resonator at any given time can be quantified as

$$\epsilon \approx \frac{(r\Delta t)^N}{1 - r\Delta t}. \tag{6.6}$$

The larger the atomic rate r and/or the time step Δt, the bigger the error will be. On the other hand, the more atoms N that are considered, the more exact the simulation is. For our purposes, an atomic rate of $r = 20$, a time step size of $\Delta t = 0.01$ and a truncation to $N = 5$ atoms leads to an error of $\epsilon \approx 0.04\%$ in reproducing the probability of having no atom arrive at the resonator within a given time step. This low estimate of the error therefore justifies the validity of this approach. A more detailed justification

of this approximation by taking the mean interaction time τ into account and calculating the probabilty of having $N \leq 5$ atoms interacting with the resonator at any given time can be found in Appendix A.

The probability of an atom exiting the resonator, $P_{\text{ex}}(\tau)$, is cumulatively Gaussian distributed, whose mean is given by the average interaction time, $\bar{\tau}$, and therefore calculated based on the time it has so far been interacting with the resonator,

$$P_{\text{ex}}(\tau) = \int_{-\infty}^{\tau} \frac{1}{\sqrt{2\pi\sigma^2}} e^{-\frac{(t-\bar{\tau})^2}{2\sigma^2}}\, dt. \tag{6.7}$$

In the case of a coherent beam of atoms, meaning a constant interaction time for each individual atom, and therefore $\sigma = 0$, the distribution of the interaction time can be modelled by a dirac delta function, which leads to the probability of an atom exiting the resonator to be

$$\begin{aligned} P_{\text{ex}}(\tau) &= \int_{-\infty}^{\tau} \delta(t-\bar{\tau})\, dt \\ &= \begin{cases} 0, & \tau < \bar{\tau} \\ & \\ 1, & \tau > \bar{\tau} \end{cases}. \end{aligned} \tag{6.8}$$

The description of the atom beam statistics in terms of a random distribution is based on Monte Carlo simulations, where one numerically simulates a single random realization, a trajectory, and then in turn averages over a large number of trajectories to get the expectation values of the random processes. This approach intrinsically accounts for the Gaussian distribution of the atoms in the beam and consequently their arrival times at the microwave resonator, as can be seen in Fig. 6.3.

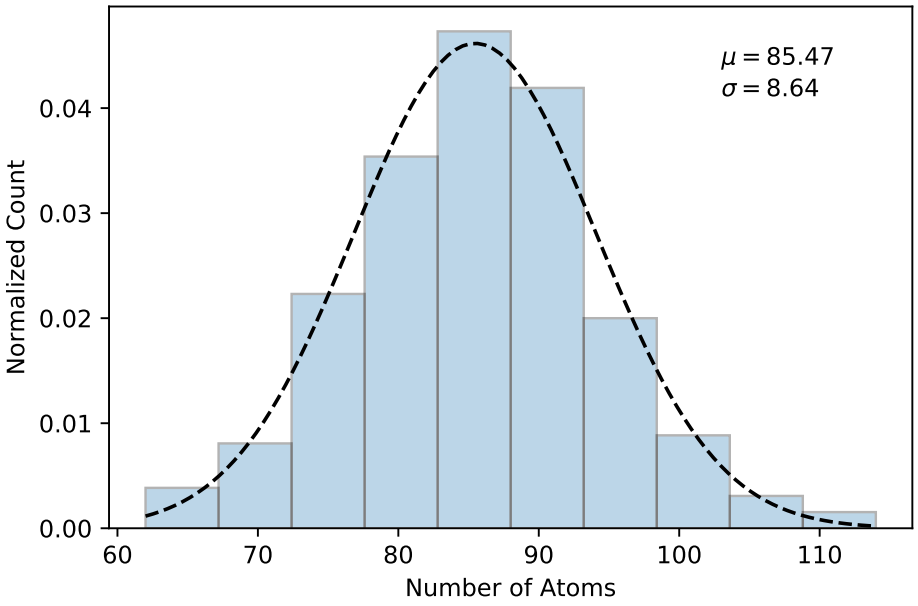

Figure 6.3: The probability distribution representing the number of atoms interacting with a resonator over a time $T = 2$ μs, with an average interaction time of $\bar{\tau} = 10$ ns and a rate of $r = 40$ atoms/μs. The simulation was carried out for 500 trajectories.

6.2 Stochastic Dynamics

The mathematical framework for this approach is based on the theory of quantum dynamical semigroups [3]. We aim to find a formal solution to the quantum master equation

$$\frac{\partial}{\partial t}\rho(t) = \mathcal{L}\rho(t), \tag{6.9}$$

a Markov semigroup which is a completely positive dynamical map ϕ_t that translates an initial density matrix onto a later density matrix within the same Hilbert space with a time parameter $t \geq 0$.

6.2.1 The stochastic process as a series of time steps

Since the Lindblad master equation is a linear superoperator, defined as the time derivative of a density matrix,

$$\mathcal{L}[\rho] = \lim_{\Delta t \to 0} \frac{\phi_{\Delta t}(\rho) - \phi_0(\rho)}{\Delta t}, \tag{6.10}$$

one can use its property

$$\phi_s(\phi_t(\rho)) = \phi_{t+s}(\rho), \tag{6.11}$$

to arrive at a mapping with the formal solution

$$\phi_{t+s}(\rho) = e^{\mathcal{L}s}\phi_t(\rho). \tag{6.12}$$

This means going from one point in time t_0, to a later point $t_1 = t_0 + \Delta t$, the formal solution for the dynamics over the small time step Δt is

$$\rho(t_1) = e^{\mathcal{L}_0 \Delta t}\rho(t_0), \tag{6.13}$$

which one can in turn take as the initial density matrix to get the formal solution after another time step Δt.

$$\begin{aligned} \rho(t_2) &= e^{\mathcal{L}_1 \Delta t}\rho(t_1) \\ &= e^{\mathcal{L}_1 \Delta t}\left(e^{\mathcal{L}_0 \Delta t}\rho(t_0)\right). \end{aligned} \tag{6.14}$$

This method can be applied analogously to any number of time steps until $t_N = N \cdot \Delta t = T$ if we define $t_0 = 0$. Thus, this constitutes a Markov chain of N steps, where given a solution to the density matrix at any time t_0 we can extend the solution to any later time t, by solving the dynamics self-consistently for each individual time step depending on the solution of the quantum master equation during the previous time step.

6.2.2 The dynamics for a constant number of atoms

The dynamics during a single time step is governed by the quantum master equation in the interaction picture,

$$\begin{aligned}\frac{\partial\hat{\rho}}{\partial t} =& i\left[\hat{\rho}, \hat{H}_i^{(N)}\right] + \frac{\sqrt{\gamma_c}}{2}(\bar{n}+1)\left(2\hat{a}\hat{\rho}\hat{a}^\dagger - \hat{a}^\dagger\hat{a}\hat{\rho} - \hat{\rho}\hat{a}^\dagger\hat{a}\right) \\ &+ \frac{\sqrt{\gamma_c}}{2}\bar{n}\left(2\hat{a}^\dagger\hat{\rho}\hat{a} - \hat{a}\hat{a}^\dagger\hat{\rho} - \hat{\rho}\hat{a}\hat{a}^\dagger\right),\end{aligned} \tag{6.15}$$

where the interaction Hamiltonian,

$$\hat{H}_i^{(N)} = g\sum_n^N\left(\hat{a}^\dagger\hat{\sigma}_-^{(n)} + \hat{a}\hat{\sigma}_+^{(n)}\right), \tag{6.16}$$

depends on the number of atoms N interacting with the microwave resonator over that time step Δt. Here we have assumed that over the small interaction time $\tau \ll 1/\gamma_a$ the atoms do not decay, therefore we only consider the dissipation of the microwave resonator. By defining the density matrix in vector form[1], $\vec{\rho}$, the quantum master equation (6.9) with the Liouvillian super operator $\mathcal{L}$ can be rewritten as

$$\begin{aligned}\frac{\partial}{\partial t}\vec{\rho} = ig\sum_n^N&\left(\mathbb{1}\otimes\hat{a}^\dagger\hat{\sigma}_-^{(n)} + \mathbb{1}\otimes\hat{a}\hat{\sigma}_+^{(n)} - \hat{a}^\dagger\hat{\sigma}_-^{(n)}\otimes\mathbb{1} - \hat{a}\hat{\sigma}_+^{(n)}\otimes\mathbb{1}\right)\cdot\vec{\rho} \\ &+\gamma_c(\bar{n}+1)\left(a\otimes a^\dagger - \frac{1}{2}a^\dagger a\otimes\mathbb{1} - \frac{1}{2}\mathbb{1}\otimes a^\dagger a\right)\cdot\vec{\rho} \\ &+\gamma_c\bar{n}\left(a^\dagger\otimes a - \frac{1}{2}aa^\dagger\otimes\mathbb{1} - \frac{1}{2}\mathbb{1}\otimes aa^\dagger\right)\cdot\vec{\rho},\end{aligned} \tag{6.17}$$

where the product between the atomic and the photonic operators is a tensor product of each of their Hilbert spaces, and the photonic operator alone is a tensor product with the identity of $(2N\times 2N)$-dimensions. This

[1] which can be done computationally by the flatten command in several programming languages, including Python's numpy module.

equation of motion for a constant number of atoms N can be formally solved for an initial time evolution $t = 0 \mapsto \Delta t$ as

$$\vec{\rho}(\Delta t) = e^{\mathcal{L}\Delta t}\vec{\rho}(0), \tag{6.18}$$

where $\rho(0)$ is assumed to be the thermal state of the system at a temperature of the coupled bath. By truncating the bosonic Hilbert space of the photon operator a in matrix form, which is reasonable for a finite temperature of the bath where the higher dimension Fock states' occupation probability is negligible, the solution for the density matrix $\vec{\rho}(\Delta t)$ becomes analytically and computationally feasible. Therefore we solve for the dynamics of the microwave resonator over the interaction time τ numerically, integrating the solution over a single time step $\Delta t \ll \tau$, and use the result as the initial density matrix to solve for the subsequent time step. With this method the dynamics during an atom-photon interaction for a number of atoms, n, prepared in their respective ground states, is obtained.

6.2.3 A beam of atoms interacting with the resonator

It is important to note that once an atom leaves the resonator, we no longer consider it part of the system, having carried away its excitation without being measured. This means that any correlations between the system and the departed atom that have built up are being neglected. In order to mathematically describe this process, we take a partial trace of the complete system, and atom(s) still interacting with the resonator, labeled ρ_s, tracing out the departed atoms' degrees of freedom,

$$\rho_s = Tr_a\left\{\rho_{tot}\right\}, \tag{6.19}$$

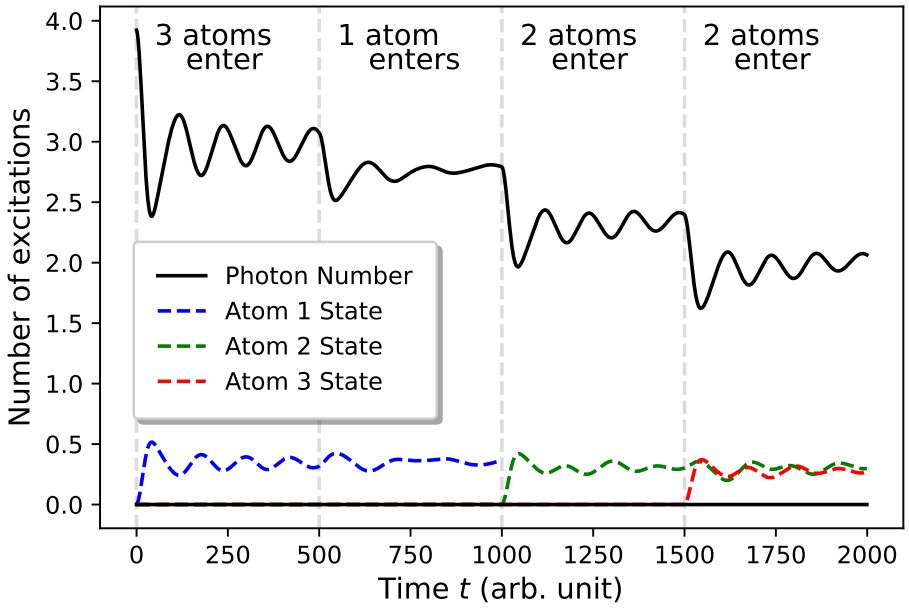

Figure 6.4: Schematic diagram of the average photon occupation number of the microwave resonator with atoms being deterministically monitored for a single realization. The moments atoms enter the resonator are marked by grey, dashed gridlines. Three atoms enter at a time $t = 0$, the state of one of them being displayed by the dashed blue curve. Two atoms leave and one enters at $t = 500$. At a time $t = 1000$, the atom 1 leaves the resonator, and a different atom 2 enters, whose dynamics are displayed by green dashed curves, and two additional atoms are introduced. At $t = 1500$ the same atom remains and its state is displayed, while 2 new atoms enter, one of which is being displayed by the red dashed curve.

of the full density matrix ρ_{tot}. Thus, any new N atoms arriving at the resonator lead to a new initial density matrix

$$\rho_0 = \rho_s \otimes |\psi_a\rangle\langle\psi_a| \otimes |\psi_b\rangle\langle\psi_b| \otimes \cdots \otimes |\psi_N\rangle\langle\psi_N|, \tag{6.20}$$

where the atoms arriving are in the ground state $|\psi_a\rangle = |g\rangle$. Fig. 6.4 shows that at any time during the coherent evolution, which follows a Rabi cycle, the resonator's average number of photons has decreased. Once the atoms leave the microwave resonator after an average interaction time $\bar{\tau}$, which can be estimated from the atom beam's velocity distribution and is experimentally known, the resonator ends up in a thermal state with a lower average number of photons than when the atoms began interacting with the resonator. Therefore, by continuously reintroducing ground state atoms to the system, the resonator mode can be effectively cooled. Since the Rabi frequency for a larger number of atoms has a larger amplitude, this approach leads to a more effective cooling process than when at most one atom interacting with the resonator is considered. At the point where the a new atom is introduced to the microwave resonator, an additional photon is absorbed by the atom within its Rabi cycle, leading to a change in the state of the microwave resonator and lowering the average number of microwave photons. Therefore, a successive introduction of atoms into the resonator leads to an effective cooling of the resonator mode to which they are coupled.

6.2.4 Ensemble average of the trajectories

To quantify the cooling of the microwave resonator mode, the relevant experimental parameters are the average interaction time, $\bar{\tau} = 50$ ns, the interaction strength, $g/(2\pi) = 4.25$ MHz, as well as the dissipation rate of the microwave resonator, $\gamma/(2\pi) = 3$ kHz, which is derived from the res-

onator's Q-factor of $Q = 10^6$ for a fundamental frequency of $\nu = 18.78\,\mathrm{GHz}$. In this process we take into account many realizations of the possible trajectories of a single experimental run. All possible realizations are then averaged at each time step, thus giving a quantifiable time-resolved expectation value that would be observable when running the experiment. The average number of thermal microwave resonator photons, or phonons in a mechanical oscillator, can be expressed as [75]

$$\langle n \rangle_{th} = \frac{1}{e^{\frac{\hbar\omega}{k_B T}} - 1}. \tag{6.21}$$

In the case of a resonance frequency of $\nu = 18.78\,\mathrm{GHz}$, the average number of photons in the environment at a temperature of $T = 4\,\mathrm{K}$ is $\langle n \rangle_{\mathrm{th}} \approx 3.96$. As can be seen from Fig. 6.5, in the case of a sparse beam of atoms, i.e., $r = 1\,\mathrm{MHz}$, the numerical calculations reproduce accurately the behavior obtained with the analytical method. Increasing the rate of atoms crossing the resonator to 15 MHz corresponds to a regime where the analytical method breaks down. The effective cooling of the fundamental resonator mode with a dense beam of Rydberg atoms prepared in the lower of two circular states is illustrated in Fig. 6.6. In this case the probability of more than one atom interacting with the resonator at a time is not negligible anymore but the cooling mechanism is more effective. This is due to the fact that the more atoms cross the resonator per second, more excitations can be carried away. Therefore, a steady state can be reached where the average number of photons has been significantly reduced to as low as $\langle n \rangle_{ss} = 0.006$ within a time of $t \approx 20 - 25\ \mu\mathrm{s}$. The parameters considered in this study are expected to be accessible with current experimental hybrid architectures [80]. In Fig. 6.7 the effect of individual atomic trajectories on

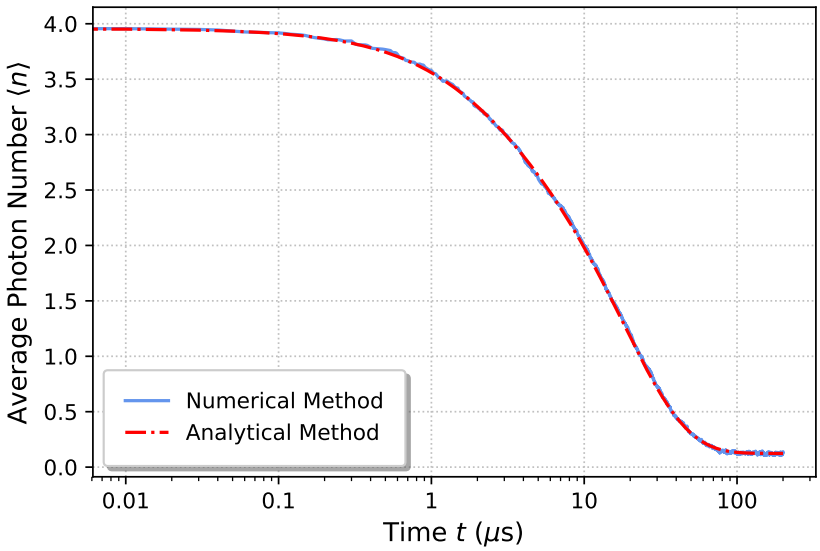

Figure 6.5: Comparison of the analytical and numerical method of treating the coupled atom-resonator system in a parameter regime in which both approaches are valid. The rate of Rydberg atoms crossing the resonator is $r = 10^6$ s^{-1}, the constant interaction time is $\tau = 50$ ns, and the interaction strength is $g/(2\pi) = 4.25$ MHz.

the resonator photon occupation number are plotted and compared to the ensemble average of 100 trajectories. The individual trajectories show the quantum jumps in the average photon number, illustrating the departure of an excited atom, which effectively lowers the average photon number in the resonator.

From the results provided here we conclude that significant gains in resonator cooling efficiency can be achieved by increasing the flux of atoms interacting with the resonator such that more than one interacts at a time. For resonators with dimensions of $10-50$ μm, and typical atom beam den-

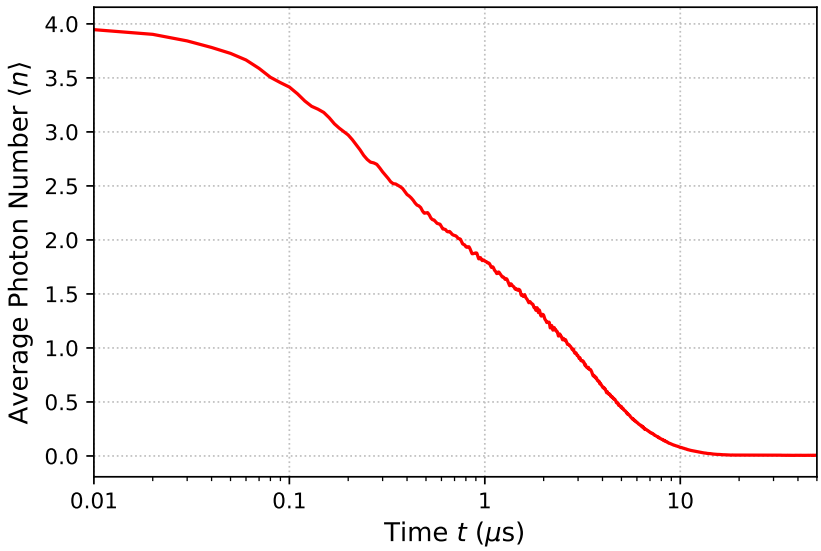

Figure 6.6: The effect of a dense beam of atoms prepared in the lower of two circular Rydberg states on the thermal photon occupation number in the resonator. The rate of Rydberg atoms crossing the resonator is $r = 15$ MHz, the constant interaction time is $\tau = 50$ ns, and the interaction strength is $g/(2\pi) = 4.25$ MHz.

sities of $\sim 10^8$ cm^{-3}, as were measured in Chapter 3, this regime in which a few $(2-5)$ atoms interact with the resonator at any given time is achievable. A similar method of using Rydberg atoms to de-excite coplanar waveguide resonators has recently been published by Sarkany et al. [99], where an ensemble of atoms in the ground state is trapped above the resonator, which extracts photons by continuous optical pumping. The efficiency of both methods is compared in Fig. 6.8 for the same experimental parameters. The cavity mode resononance frequency is $\omega/(2\pi) = 5$ GHz and its quality factor is assumed to be $Q = 10^5$, resulting in a decay rate of

(a) First calculated trajectory.

(b) Second calculated trajectory.

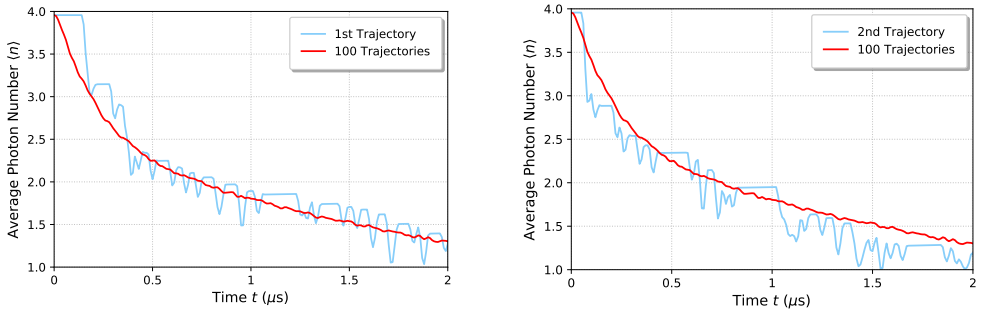

Figure 6.7: Two calculated trajectories for individual atoms compared to the average of 100 simulated trajectories, displaying the quantum jumps in the photon field induced by an atom entering the resonator and being excited.

(a) Method by Sarkany et al. [99]

(b) Numerical atom beam method.

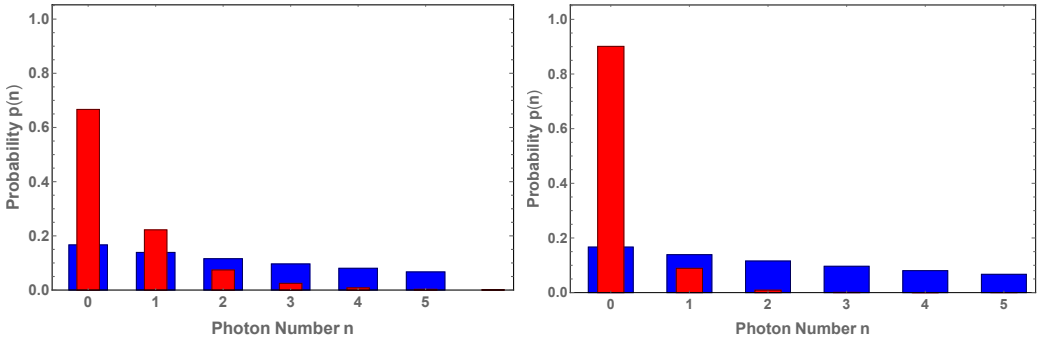

Figure 6.8: Comparison of the photon probability distribution of the method a) studied by Sarkany et al. [99] and b) the method investigated in this chapter with an atomic rate of $r = 145 \cdot 10^6$ s^{-1} and an average interaction time of $\bar{\tau} = 10$ ns. Both concepts lead to a sharp peak around $n = 0$ and a significantly lower average effective photon number in the steady state.

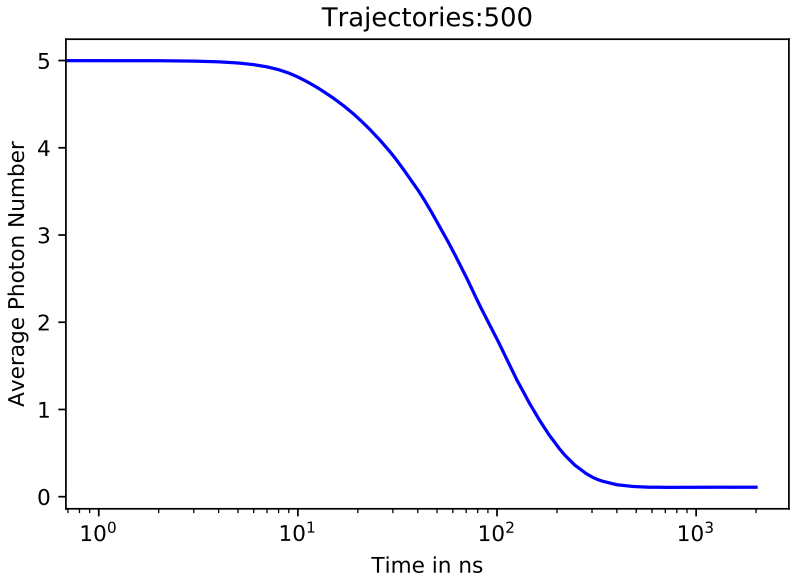

Figure 6.9: Time-dependence of the average resonator photon number. An average steady state photon number of $\langle n \rangle_{ss} \gtrsim 0.1$ can be reached within a time of $t \approx 1\ \mu$s, utilizing approximately 150 Rydberg atoms to effectively cool the resonator.

$\gamma/(2\pi) \approx 50$ kHz. The coupling strength between resonator and atom is $g/(2\pi) = 5$ MHz. Considering these parameters, and assuming an atomic beam rate of $r = 145 \cdot 10^6\ \mathrm{s}^{-1}$ with an average interaction time of $\bar{\tau} = 10$ ns, the average number of photons achievable in the resonator is $\langle n \rangle_{ss} \gtrsim 0.1$, compared to $\langle n \rangle_{ss} = 0.5$ given in [99]. The time-resolved evolution of the average photon number in the resonator is displayed in Fig. 6.9, illustrating the rapid effective cooling. Based on this timescale, the average number of Rydberg atoms crossing the resonator to achieve this cooling effect is estimated to be approximately 150 atoms.

Chapter 7

A Microwave Resonator-Nanomechanical Oscillator–System driven by an Atomic Beam

Recently, one particular focus of hybrid quantum system research has been the proposal of quantum state preparation of an individual system with the help of another quantum system. The methods described and analyzed in Chapters 5 and 6 to cool selected modes of coplanar microwave resonators are in principle quite general. Because of the wide range of Rydberg-Rydberg transition frequencies available in any given atom or molecule they can be implemented over a wide range of resonance frequencies. With this in mind the formalisms developed in Chapter 5 and Chapter 6 are extended in this chapter to cool selected modes of nanome-

chanical resonators. The resonators considered have resonance frequencies in the microwave regime of the electromagnetic spectrum. The types of nanomechanical resonator devices of interest are therefore those based on micrometer membrane [107] or toroidal microresonator technologies [112].

7.1 Derivation of the Hamiltonian

To treat the coupled Rydberg-atom–optomechnaical-resonator system, the starting point considered is represented by the Hamiltonian given and simplified in [19],

$$H = H_0 + H_{\rm ac} + H_{\rm mc} + H_{\rm L}, \tag{7.1}$$

where H_0 are the system Hamiltonians of the atoms, photon and phonon modes involved, $H_{\rm ac}$ is the Hamiltonian describing the coupling between atoms and cavity, $H_{\rm mc}$ represents phonon-photon interaction of the nanomechanical resonator and the cavity, and $H_{\rm L}$ is the laser drive of the pump mode of the cavity.

The Hamiltonian (7.1) for the combined Rydberg-atom–optomechanical-oscillator can be expressed in detail as

$$H_0 = \omega_m b^\dagger b + \omega_0 a^\dagger a + \frac{\omega_a}{2}\sum_i \sigma_z^{(i)} + \omega_p a_p^\dagger a_p, \tag{7.2}$$

$$H_{\rm ac} = \sum_i g_i \left(a\sigma_+^{(i)} + a^\dagger \sigma_-^{(i)}\right), \tag{7.3}$$

$$H_{\rm mc} = g_m (b + b^\dagger)(a^\dagger a + a_p^\dagger a_p - a^\dagger a_p - a_p^\dagger a), \tag{7.4}$$

$$H_{\rm L} = \Omega_p e^{-i\omega_L t} a_p^\dagger + \Omega_p^* e^{i\omega_L t} a_p. \tag{7.5}$$

Here, a two mode cavity system with frequencies ω_0 and ω_p mediates an excitation transfer between a moving membrane, toroidal microresonator

or patterned nanobeam (i.e. nanomechanical oscillator) and the atom(s). In order to enhance the radiation pressure coupling g_0 between the mechanical oscillator and the resonator, a laser with frequency ω_L and Rabi-frequency Ω_p continuously pumps the cavity. This laser-pump frequency ω_L is strongly detuned from the atomic transition frequency ω_a, which is close to or on resonance, respectively, with the second cavity mode ω_0. However, we are ignoring the dipole-dipole interaction between the atoms itself. Transforming these expressions into a frame of reference rotating with respect to the laser drive by applying the unitary transformation $U = exp\left[-i\omega_L t\left(a^\dagger a + a_p^\dagger a_p + \sum_i \frac{\sigma_z^{(i)}}{2}\right)\right]$, the time-dependence in the driving term is removed via the application of a lemma following from the BCH formula,

$$e^{sX} Y e^{-sX} = Y + s[X\ ,\ Y], \tag{7.6}$$

if $[X\ ,\ [X\ ,\ Y]] = [Y\ ,\ [X\ ,\ Y]] = 0$.

We consider the regime of a strong laser pump of the auxiliary cavity mode, $\Omega_p \gg g_m$, i.e., the coupling of photons of this auxiliary cavity mode to mechanical resonator phonons is weak. Here the pump mode of the cavity is close to a coherent steady state α apart from small quantum fluctuations $\langle \delta a_p^\dagger \delta a_p \rangle \ll |\alpha|^2$, stemming from nonlinearities introduced by the nanomechanical resonator [48]. This allows for the replacement of the operator $a_p \rightarrow \alpha + \delta a_p$, and leads to a linearization of the radiation pressure coupling in H_{mc}. The modified equilibrium position of the nanomechanical oscillator can be expressed as $b \rightarrow \beta + b$. First the zero point energy is shifted, which can be done because a global phase shift does not affect the dynamics of the system. Applying the displacement operator $D(\alpha) = \exp(\alpha a^\dagger - \alpha^* a)$

to the Hamiltonian leads to a unitary transformation of the form

$$D(\alpha)aD(\alpha) = a + \alpha. \tag{7.7}$$

Therefore choosing appropriate values for the displacements

$$\alpha = \sqrt{-\frac{\omega_m}{g_m}\beta}, \tag{7.8}$$

$$(\beta + \beta^*) = -\frac{\Omega_p + \Delta_p}{g_m}, \tag{7.9}$$

and including only enhanced optomechanical interaction strengths of order $|g\alpha|$ and $|g\alpha|^2$ eliminates the first oder terms in $b^{(\dagger)}$ and $\delta a_p^{(\dagger)}$. Hence, we obtain

$$\begin{aligned} H &= \Big(\Delta_0 + g_m(\beta + \beta^*)\Big)a^\dagger a - \Omega_p \delta a_p^\dagger \delta a_p + \omega_m b^\dagger b \\ &\quad + \frac{\Delta_a}{2}\sum_i \sigma_z^{(i)} + H_{al} + g_m(b + b^\dagger)(\alpha^* \delta a_p + \alpha \delta a_p^\dagger) \\ &\quad - g_m(b + b^\dagger)(\alpha^* a + \alpha a^\dagger) - g_m(\beta + \beta^*)(\alpha^* a + \alpha a^\dagger). \end{aligned} \tag{7.10}$$

Further transforming the Hamiltonian into a frame of reference rotating with respect to $(\Omega_p \delta a_p^\dagger \delta a_p + \omega_m b^\dagger b)$ and assuming $|g_m \alpha| \ll |\Omega_p - \omega_m|$, which is self-consistenlty fulfilled due to the strong pump laser drive and a small single photon-phonon interaction strength, leads to fast oscillating terms in the coupling strength associated with the $b^{(\dagger)}\delta a_p$ interactions. These fast oscillating terms can be neglected under the rotating wave approximation (RWA) [4], and doing this leads to the result that

$$\begin{aligned} H &\approx \tilde{\Delta}_0 a^\dagger a + \tilde{\Delta}_p \delta a_p^\dagger \delta a_p + \omega_m b^\dagger b + \frac{\Delta_a}{2}\sum_i \sigma_z^{(i)} + H_{al} \\ &\quad - g_m(b + b^\dagger)(\alpha^* a + \alpha a^\dagger) - g_m(\beta + \beta^*)(\alpha^* a + \alpha a^\dagger). \end{aligned} \tag{7.11}$$

The $\delta a_p^\dagger \delta a_p$-terms are completely decoupled from the rest of the system, and are therefore ignored in the following by performing a partial trace of

the density matrix with respect to the degrees of freedom of the photons with frequency of the driving field. Thus, the influence on the dynamics of the entire system will simply be a global phase-shift. Applying another displacement operator unitary transformation, $U = exp(\theta a - \theta a^\dagger)$, eliminates the linear terms in $a^{(\dagger)}$ for an appropriate choice of $\theta = \frac{g_m(\beta+\beta^*)\alpha}{\tilde{\Delta}_0}$. It also does not affect H_{al} because prior to applying the RWA it can be written as $H_{al} = ig_{ac}(\sigma_+ + \sigma_-)(a - a^\dagger)$, which commutes with the unitary transformation. The resulting linear terms in the $b^{(\dagger)}$-operators can be absorbed into their displacement again. This is accomplished analogously to the procedure above by adjusting the term for the pump mode laser intensity in Eq. (7.8),

$$|\alpha|^2 \to 2\theta - \frac{\omega_m}{g_m}\beta. \tag{7.12}$$

By assuming $|\alpha g_m| \ll |\tilde{\Delta}_0 + \omega_m|$, whereas $|\tilde{\Delta}_0 - \omega_m|$ is of the same order of magnitude as $|\alpha g_m|$, we can apply a further RWA where we can neglect the rapidly oscillating counter-rotating terms ba and $b^\dagger a^\dagger$, and then transform back, to obtain

$$H \approx \tilde{\Delta}_0 a^\dagger a + \omega_m b^\dagger b + \frac{\Delta_a}{2}\sum_i \sigma_z^{(i)} + G(a^\dagger b + a b^\dagger) + \sum_i g_i\left(a\sigma_+^{(i)} + a^\dagger \sigma_-^{(i)}\right), \tag{7.13}$$

where the photon-enhanced radiation pressure coupling strength is redefined as $G = -g_m\alpha$. Because $\alpha \propto \sqrt{N_p}$, and assumed to be real-valued for convenience but without loss of generality, this means that the interaction strength between the nanomechanical oscillator and the cavity is proportional to the intensity of the pump laser.

In the calculations and figures in the Chapters 7.2 and 7.3 we assume the following parameters, unless otherwise stated, in terms of the nanomechanical oscillator frequency: a frequency of the microwave resonator of

$\omega_c/\omega_m = 2$, a single-photon optomechanical coupling strength of $g_m/\omega_m = 2.5 \cdot 10^{-4}$, that together with a laser-drive generating $n_d = 1.6 \cdot 10^5$ photons enables a light-enhanced coupling strength of $G/\omega_m = 0.1$, a Rydberg atom transition frequency of $\omega_a/\omega_m \approx 2$, and atom-resonator coupling strength $g/\omega_m = 0.1$. Achievable experimental parameters for the individual quantum systems fall into the same orders of magnitude, as can be seen in Table 1.2, when a patterned Si nanobeam [25] is considered as the nanomechanical oscillator. However, a hybrid architecture of a combination of these three individual quantum systems with the same parameters as considered here has not yet been developed. The study in this Chapter therefore serves as a proof of principle.

In the following we aim to diagonalize the photon-phonon–subsystem by moving to a joint polariton-picture, which allows for the theoretical framework developed in Chapter 5 and Chapter 6 to be applied to the coupling of this subsystem to an atomic beam.

7.2 Microwave Resonator-Mechanical Oscillator–Subsystem

To study the photon-phonon–subsystem comprised of an optical cavity and a nanomechanical resonator, the Hamiltonian $H = H_{\mathrm{mc}} + H_{\mathrm{ac}}$ where

$$H_{\mathrm{mc}} = \tilde{\Delta}_0 a^\dagger a + \omega_m b^\dagger b + G(a^\dagger b + a b^\dagger), \tag{7.14}$$

can be exactly diagonalized within a new basis set of polariton excitations because the total particle number $N = a^\dagger a + b^\dagger b$ is conserved for this

subsystem:

$$[H_{\mathrm{cm}}\ ,\ a^\dagger a + b^\dagger b] = 0 \tag{7.15}$$

where $[a^{(\dagger)}, a^\dagger a] = (-)a^{(\dagger)}$ and $[b^{(\dagger)}, b^\dagger a] = (-)b^{(\dagger)}$. This means that the eigenvalues of the Hamiltonian H_{cm} can be obtained in terms of Bogoliubov modes via the canonical transformation

$$\begin{pmatrix} a \\ b \end{pmatrix} = \begin{pmatrix} \cos\phi & \sin\phi \\ -\sin\phi & \cos\phi \end{pmatrix} \begin{pmatrix} \alpha \\ \beta \end{pmatrix}. \tag{7.16}$$

The diagonalized Hamiltonian expressed in terms of the new modes is therefore

$$\begin{pmatrix} a^\dagger & b^\dagger \end{pmatrix} \begin{pmatrix} \tilde{\Delta}_0 & G \\ G & \omega_m \end{pmatrix} \begin{pmatrix} a \\ b \end{pmatrix} \stackrel{!}{=} \begin{pmatrix} \alpha^\dagger & \beta^\dagger \end{pmatrix} \begin{pmatrix} \omega_\alpha & 0 \\ 0 & \omega_\beta \end{pmatrix} \begin{pmatrix} \alpha \\ \beta \end{pmatrix}, \tag{7.17}$$

where we need to solve the equation system following from

$$\begin{pmatrix} \cos\phi & -\sin\phi \\ \sin\phi & \cos\phi \end{pmatrix} \begin{pmatrix} \tilde{\Delta}_0 & G \\ G & \omega_m \end{pmatrix} \begin{pmatrix} \cos\phi & \sin\phi \\ -\sin\phi & \cos\phi \end{pmatrix} = \begin{pmatrix} \omega_\alpha & 0 \\ 0 & \omega_\beta \end{pmatrix}. \tag{7.18}$$

This equation system has four different sets of solutions. For convinience the set for which both $\sin\phi, \cos\phi > 0$ is chosen for the canonical transformation. We define the detuning $\Delta = \omega_m - \tilde{\Delta}_0$, Rabi frequency $\Omega = \sqrt{\Delta^2 + 4G^2}$ and average polariton energy $E_0 = (\tilde{\Delta}_0 + \omega_m)/2$ to simplify the

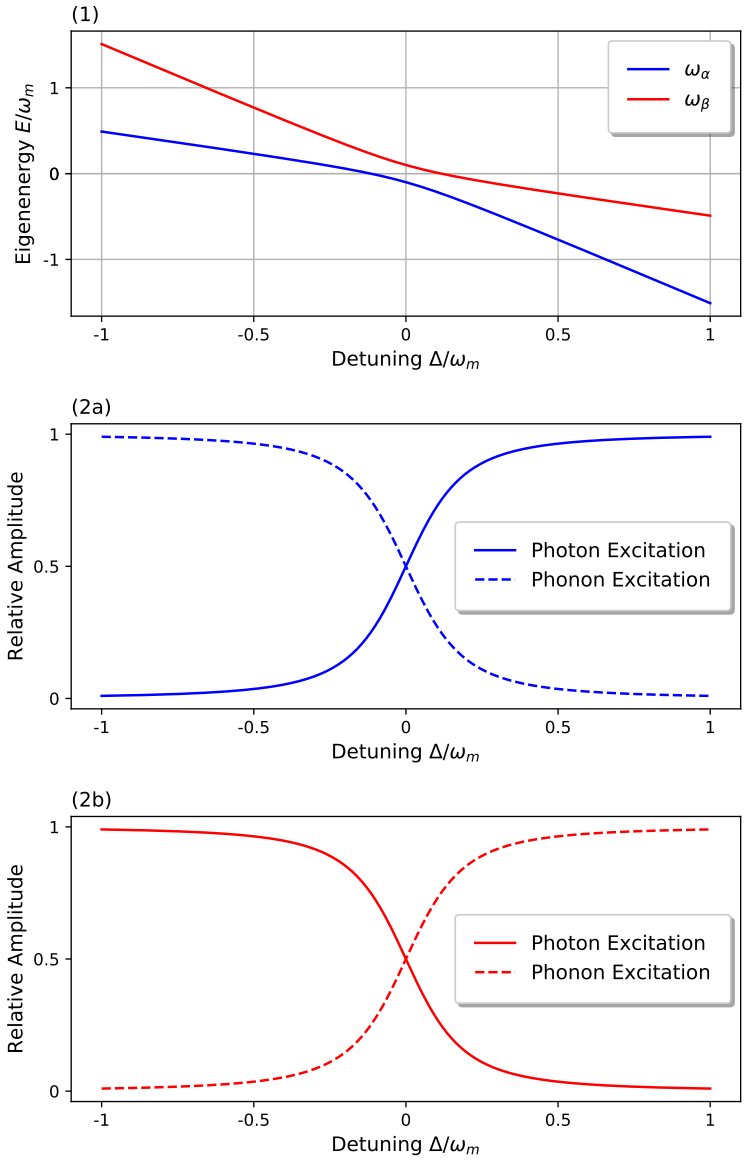

Figure 7.1: (1) The dependence of the eigenenergies of both polariton-modes is displayed when the detuning between the microwave resonator and the laser drive $\tilde{\Delta}_0$ is decreased from $2\,\omega_m$ to $0\,\omega_m$ by varying the laser drive frequency. (2a) and (2b) show the relative amplitudes of the photonic and phononic excitation.

expressions to

$$\cos\phi = \sqrt{\frac{\Omega+\Delta}{2\Omega}}, \tag{7.19}$$

$$\sin\phi = \sqrt{\frac{\Omega-\Delta}{2\Omega}}, \tag{7.20}$$

$$\omega_\alpha = E_0 - \frac{\Omega}{2}, \tag{7.21}$$

$$\omega_\beta = E_0 + \frac{\Omega}{2}, \tag{7.22}$$

where the polaritons are a combination of photons and phonons.

7.3 Microwave Resonator-Mechanical Oscillator-Atom–System

Rewriting the full Hamiltonian in Eq. (7.13) in terms of the Bogoliubov-polariton modes, and considering for the sake of simplicity the special case of only one atom interacting with the resonator,

$$H = \omega_\alpha\alpha^\dagger\alpha+\omega_\beta\beta^\dagger\beta+\frac{\Delta_a}{2}\sigma_z+g\cos\phi\left(\alpha\sigma_+ + \alpha^\dagger\sigma_-\right)+g\sin\phi\left(\beta\sigma_+ + \beta^\dagger\sigma_-\right) \tag{7.23}$$

It can be seen in Fig. 7.1 that for each atomic (de-)excitation one polariton-mode is (created) annihilated, but with a different composition of photon- and phonon-parts. A completely symmetric state would be reached for $\Delta = 0$, because in that case $\sin\phi = \cos\phi$.

The commutator between the total excitation number (polariton number and atomic excitation) and the Hamiltonian is

$$[\alpha^\dagger\alpha + \beta^\dagger\beta + \frac{\sigma_z}{2}\ ,\ H] = 0. \tag{7.24}$$

Because the particle number is conserved, the full Hamiltonian can be diagonalized within this 3-particle-excitation subspace. One point to note in doing this is the fact that this new quasiparticle, a three-particle-polariton, is a mixture of two bosonic polaritons and a fermion. Therefore it is first necessary to transform the problem into an interaction picture according to

$$\hat{H}_i = \hat{U}_{rf}(\hat{H} - \hat{H}_0)\hat{U}_{rf}^{\dagger}, \tag{7.25}$$

with a rotating frame at the detuning of the atomic frequency,

$$\begin{aligned} \hat{U}_{rf} &= \exp\left[i\Delta_a t\hat{H}_0\right] \\ &= \exp\left[i\Delta_a t\left(\hat{\alpha}^{\dagger}\hat{\alpha} + \hat{\beta}^{\dagger}\hat{\beta} + \frac{\hat{\sigma}_z}{2}\right)\right]. \end{aligned} \tag{7.26}$$

Following this, the interaction Hamiltonian can be written in matrix form as

$$\hat{H}_i = \begin{pmatrix} \alpha^{\dagger} & \beta^{\dagger} & \sigma_+ \end{pmatrix} \begin{pmatrix} \Delta_\alpha & 0 & g\cos\phi \\ 0 & \Delta_\beta & g\sin\phi \\ g\cos\phi & g\sin\phi & 0 \end{pmatrix} \begin{pmatrix} \alpha \\ \beta \\ \sigma_- \end{pmatrix}, \tag{7.27}$$

where the detunings $\Delta_{\alpha,\beta} = \omega_{\alpha,\beta} - \Delta_a$ represent the frequency difference between the polariton modes $\alpha^{(\dagger)}$, $\beta^{(\dagger)}$ of the microwave resonator-mechanical oscillator subsystem and the detuning of the atomic transition frequency from the frequency of the pump laser. The eigenvalues of this Hamiltonian can be readily calculated and exhibit an avoided crossing for the parameters fulfilling all approximations, as seen in Fig. (7.2). By changing to a basis corresponding to the 3-particle-excitation modes $\hat{x}, \hat{y}, \hat{z}$, which is done

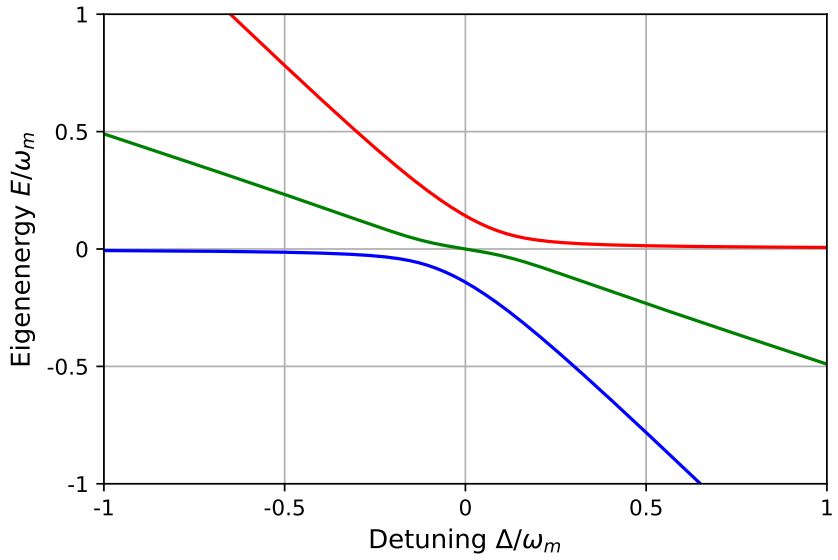

Figure 7.2: The first 3 eigenenergies of the Hamiltonian H_i depending on the detuning between the microwave resonator detuning and the mechanical oscillator $\Delta = \tilde{\Delta}_0 - \omega_m$. The detuning between the microwave resonator and the laser drive $\tilde{\Delta}_0$ is decreased from $2\,\omega_m$ to $0\,\omega_m$.

via the canonical transformation

$$\begin{pmatrix} \hat{\alpha} \\ \hat{\beta} \\ \hat{\sigma}_- \end{pmatrix} = \hat{R} \begin{pmatrix} \hat{x} \\ \hat{y} \\ \hat{z}, \end{pmatrix} \tag{7.28}$$

the Hamiltonian can be rewritten. As a result, the eigenvalues of the polariton-modes are numerically calculated from

$$\begin{pmatrix} \omega_x & 0 & 0 \\ 0 & \omega_y & 0 \\ 0 & 0 & \omega_z \end{pmatrix} = \hat{T}^{\dagger} \begin{pmatrix} \Delta_\alpha & 0 & g\cos\phi \\ 0 & \Delta_\beta & g\sin\phi \\ g\cos\phi & g\sin\phi & 0 \end{pmatrix} \hat{T}. \tag{7.29}$$

The results for $\omega_{(x,y,z)}$ give the eigenenergies of the Hamiltonian and therefore its resonance modes. The transformation matrix $\hat{T}$, consisting of the eigenvectors of the Hamiltonian, gives information about their polaritonic composition, revealing if these energies are mostly dominated by atomic, phononic or photonic excitations. The rotation matrix mixing the three particle types is given by the eigenvectors of the Hamiltonian H_i that have been previously plotted in Fig. 7.2. The composition of the quasiparticles representing the eigenenergies is displayed in Fig. 7.3. It can be seen that the first two three-particle-polaritons, graphs (a) and (b), are an antisymmetric mixture of atomic excitation and either α-polariton, the blue curve (a), or β-polariton, which is the red curve (b). The third quasiparticle, displayed by the green curve (c), shows a transition from being dominantly a β-polariton, to mostly atomic excitation at zero detuning between the polaritons, $\Delta = 0$, This information is crucial as it dictates the parameter regime in which the polariton modes are mostly phononic. In order to engineer a cooling mechanism for the phononic mode of the mechanical oscillator via a beam of atoms, in the next section we exploit the interaction between the static microwave resonator-mechanical oscillator-subsystem and the atoms prepared in the lower circular Rydberg state to de-excite

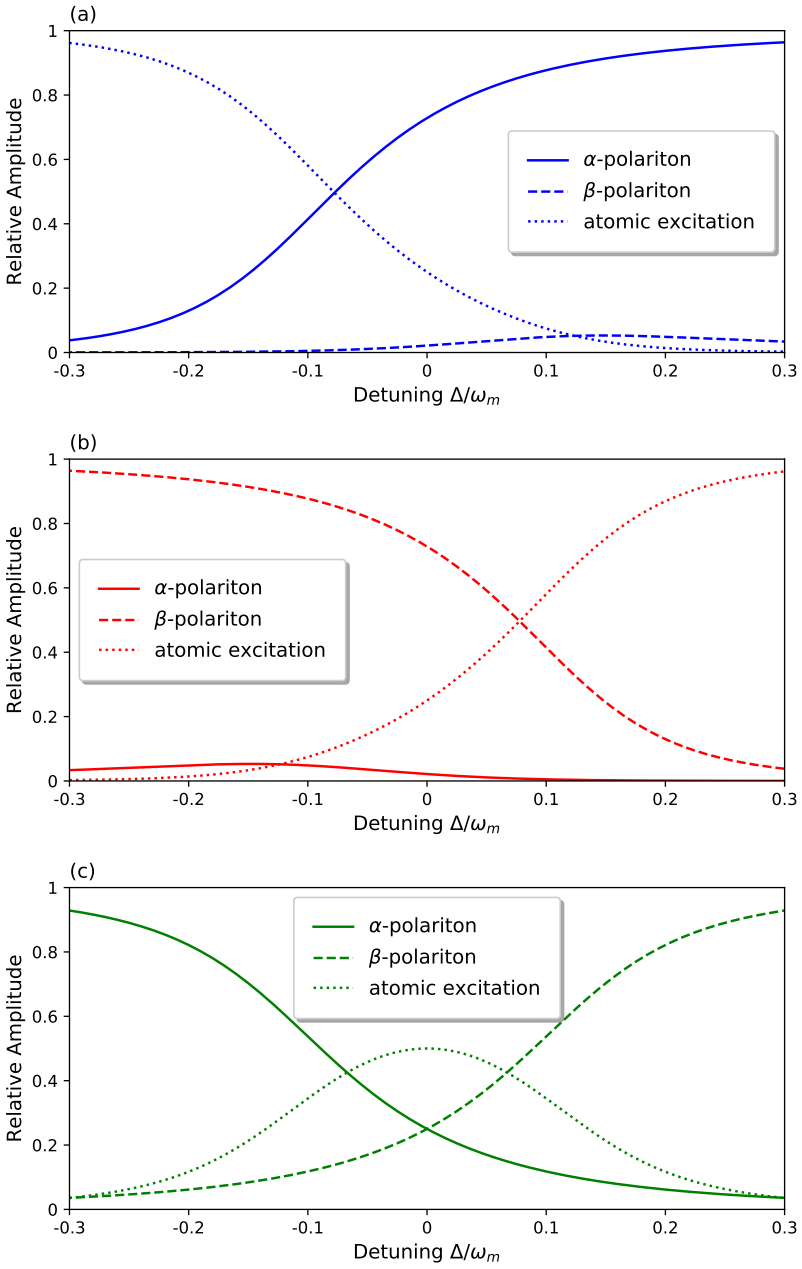

Figure 7.3: The quasiparticle-composition of the eigenenergies (a) ω_x, (b) ω_y and (c) ω_z in Equ. (7.29) of the interaction Hamiltonian, H_i, that are plotted in Fig. 7.2.

such a mainly phononic polariton mode.

7.4 The Atomic Beam as an engineered environment

The Hamiltonian of the complete atom-polariton system can be split into two parts, one with and one without the atomic interaction:

$$\begin{aligned} H &= H_0 + H_{\mathrm{i}}, && (7.30)\\ H_0 &= \omega_\alpha \alpha^\dagger \alpha + \omega_\beta \beta^\dagger \beta + \frac{\omega_a}{2}\sigma_z, && (7.31)\\ H_{\mathrm{i}} &= g\cos\phi\left(\alpha\sigma_+ + \alpha^\dagger\sigma_-\right) + g\sin\phi\left(\beta\sigma_+ + \beta^\dagger\sigma_-\right). && (7.32) \end{aligned}$$

A necessary prerequisite to apply the theoretical framework established in Chapter 5 to mathematically describe a switchable interaction is that the commutator between the system Hamiltonian and the interaction Hamiltonian vanishes. This commuter is calulcated to be

$$[H_0, H_{\mathrm{i}}] = g\cos\phi(\omega_\alpha - \omega_a)(\alpha^\dagger\sigma_- - \alpha\sigma_+) + g\sin\phi(\omega_\beta - \omega_a)(\beta^\dagger\sigma_- - \beta\sigma_+). \quad (7.33)$$

If it is assumed that the atomic transition frequency is resonanct with one of the two polariton modes, then

- Either $\omega_\alpha - \omega_a = 0$

$$[H_0, H_{\mathrm{i}}] = g\sqrt{\frac{\Omega^2 - \Omega\Delta}{2}}(\beta^\dagger\sigma_- - \beta\sigma_+). \quad (7.34)$$

  If $\Delta \approx 0$, it follows that $[H_0, H_{\mathrm{i}}] \approx \frac{gG}{\sqrt{2}}(\beta^\dagger\sigma_- - \beta\sigma_+)$. Therefore, an upper limit can be given in the regime $\Delta \geq 0$ for the commutator

$$[H_0, H_{\mathrm{i}}] \leq \frac{gG}{\sqrt{2}}(\beta^\dagger\sigma_- - \beta\sigma_+). \quad (7.35)$$

- Alternatively, for $\omega_\beta - \omega_a = 0$ and $\Delta \leq 0$ a limit is analogously obtained to be

$$[H_0, H_i] \leq \frac{gG}{\sqrt{2}}(\alpha\sigma_+ - \alpha^\dagger\sigma_-). \tag{7.36}$$

From this it can be seen that the sign of the detuning determines which polariton mode is close to resonance with the atomic transition frequency. Following this, an upper/lower limit can be obtained for the commutator between the full Hamiltonian and the atomic Hamiltonian. In order to determine which regime to consider to most effectively cool the phonon-mode, the combination of the three polariton types in Fig.(7.3) has to be investigated. This can be done by plotting both regimes considered, the eigenenergies of the interaction Hamiltonian within these regimes, and the composition of the excitations of the polariton types following from the eigenvectors of this calculation. These eigenvectors then need to be additionally rotated around the atomic-excitation axis with a 3D rotation matrix, according to their polariton-rotation when diagonalizing the mechanical oscillator-resonator subsystem. The result is the mix of photon-, phonon- and atom-excitations of the eigenstates of this interaction Hamiltonian. Whichever eigenenergy contains the highest proportion of phonon- and atom-excitations then has to be cooled by removing a quasiparticle, which is achieved by removing the atomic excitation of the polariton via the beam of atoms. This is going to establish the regime of experimental parameters leading to the most effective cooling procedure of the mechanical oscillator mode.

Assuming a sufficiently small coarse grained time scale, Δt, so that

$$\sqrt{gGn_{(\alpha,\beta)}}\Delta t \ll 1, \tag{7.37}$$

the commutator in Eq. (7.33) is negligible and the time evolution operator can be approximated as

$$\begin{aligned} U &= e^{-i\Delta t H} \\ &= e^{-i\Delta t H_0} e^{-i\Delta t H_a} e^{O^2(\Delta t \sqrt{gG})} \dots \\ &\approx e^{-i\Delta t H_0} e^{-i\Delta t H_a}. \end{aligned} \tag{7.38}$$

Thus, the formalism introduced in Chapter 5 can be applied. On a sufficiently small coarse grained time-scale the time-evolution of the density-matrix of the whole system without an atom present can be written as

$$\hat{\rho}_0(t + \Delta t) = e^{-i\hat{H}_0(\Delta t)} \hat{\rho}(t) e^{i\hat{H}_0(\Delta t)}, \tag{7.39}$$

and with an atom present as

$$\hat{\rho}_1(t + \Delta t) = e^{(-i\hat{H}_0\Delta t)} \left[e^{(-i\hat{H}_a\tau)} \hat{\rho}(t) e^{(i\hat{H}_a\tau)} \right] e^{(i\hat{H}_0\Delta t)}, \tag{7.40}$$

where τ is the interaction time of a single atom with the mechanical oscillator-resonator–system. By combining these two equations, considering the rate of ground state atoms r and excited state atoms R crossing the resonator per second and transforming to an interaction picture with respect to H_0, we arrive at an equation determining the density matrix at time $t + \Delta t$ given the density matrix at time t, which can be expressed as

$$\begin{aligned} \hat{\rho}_{\text{tot}}(t + \Delta t) &= \hat{\rho}_{\text{tot}}(t) \cdot (1 - r\Delta t - R\Delta t) + r\Delta t \int d\tau P_g(\tau)\, e^{-i\hat{\mathcal{H}}_a\tau/\hbar} \hat{\rho}_{\text{tot}}(t) e^{i\hat{\mathcal{H}}_a\tau/\hbar} \\ &\quad + R\Delta t \int d\tau P_e(\tau)\, e^{-i\hat{\mathcal{H}}_a\tau/\hbar} \hat{\rho}_{\text{tot}}(t) e^{i\hat{\mathcal{H}}_a\tau/\hbar}, \end{aligned} \tag{7.41}$$

where τ is the interaction time of a single atom with the microwave resonator-mechanical oscillator system and $P_{g,e}(\tau)$ is the distribution of interaction times for the ground and excited state, respectively. Before an

atom prepared in the lower circular Rydberg state interacts with the system the total density matrix can be factorized into a density matrix describing the state of the system, $\hat{\rho}_{\rm cm}$ and a density matrix $|g\rangle\langle g|$ describing the pure state of the atom at arrival, as $\hat{\rho}_{\rm tot} = \hat{\rho}_{\rm cm} \otimes |g\rangle\langle g|$. In the case of an atom prepared in the excited circular state, the full density matrix factorizes as $\hat{\rho}_{tot} = \hat{\rho}_{cm} \otimes |e\rangle\langle e|$ before the interaction. Hence, it is necessary to investigate the effect of the atomic interaction Hamiltonian on the ground and excited states, respectively, of a two level system (i.e. atom in a circular Rydberg state). In the case of atoms prepared in the lower circular state,

$$e^{(-ig\hat{H}_a\tau)}|g\rangle = \sum_k \frac{(-i\tau g)^k \hat{H}_a^k}{k!}|g\rangle, \tag{7.42}$$

with

$$H_a = \left(\cos\phi\alpha + \sin\phi\beta\right)\sigma_+ + \left(\cos\phi\alpha^\dagger + \sin\phi\beta^\dagger\right)\sigma_-, \tag{7.43}$$

$$H_a^2 = \cos\phi\sin\phi(\alpha^\dagger\beta + \alpha\beta^\dagger) + \cos^2\phi\alpha^\dagger\alpha + \sin^2\phi\beta^\dagger\beta + |e\rangle\langle e|, \tag{7.44}$$

where the substitution $\hat{H}_a \rightarrow g\hat{H}_a$ has been made and the interaction strength between atom and photon-field g has been taken out of the atomic interaction Hamiltonian. The exponential series in Eq. (7.42) is extended up to second order in $g\bar{\tau} \ll 1$, where $\bar{\tau}$ is the average interaction time of an atom with the system. This approximation is fulfilled in the weak-coupling regime where the perturbation of the system due to the interaction with the atom is small. Evaluating the exponentials to second order and taking the partial trace with respect to the atomic degrees of freedom, $\hat{\rho}_{\rm cm}(t) = Tr_{\rm a}\{\hat{\rho}_{\rm tot}(t)\}$, we arrive at an equation giving the change of the reduced density matrix of the system due to an interaction with a beam of atoms (with at most one atom interacting with the system during each time

step Δt). Averaging over the distribution, assuming here for simplicity that we can replace these terms by the average interaction time $\tau \to \bar{\tau}$, we can rewrite the equation of motion for the reduced density matrix so that it closely resembles the form of the Lindblad quantum master equation, i.e.,

$$\begin{aligned}
\left.\frac{\partial \hat{\rho}_{cm}(t)}{\partial t}\right|_{atom} = &+ \frac{rg^2\tau^2\cos^2\phi}{2}\Big(2\alpha\hat{\rho}_{cm}(t)\alpha^\dagger - \hat{\rho}_{cm}(t)\alpha^\dagger\alpha - \alpha^\dagger\alpha\hat{\rho}_{cm}(t)\Big) \\
&+ \frac{rg^2\tau^2\sin^2\phi}{2}\Big(2\beta\hat{\rho}_{cm}(t)\beta^\dagger - \hat{\rho}_{cm}(t)\beta^\dagger\beta - \beta^\dagger\beta\hat{\rho}_{cm}(t)\Big) \\
&+ \frac{rg^2\tau^2\sin\phi\cos\phi}{2}\Big(2\alpha\hat{\rho}_{cm}(t)\beta^\dagger - \hat{\rho}_{cm}(t)\alpha\beta^\dagger - \alpha\beta^\dagger\hat{\rho}_{cm}(t)\Big) \\
&+ \frac{rg^2\tau^2\sin\phi\cos\phi}{2}\Big(2\beta\hat{\rho}_{cm}(t)\alpha^\dagger - \hat{\rho}_{cm}(t)\alpha^\dagger\beta - \alpha^\dagger\beta\hat{\rho}_{cm}(t)\Big) \\
&+ \frac{Rg^2\tau^2\cos^2\phi}{2}\Big(2\alpha^\dagger\hat{\rho}_{cm}(t)\alpha - \hat{\rho}_{cm}(t)\alpha\alpha^\dagger - \alpha\alpha^\dagger\hat{\rho}_{cm}(t)\Big) \\
&+ \frac{Rg^2\tau^2\sin^2\phi}{2}\Big(2\beta^\dagger\hat{\rho}_{cm}(t)\beta - \hat{\rho}_{cm}(t)\beta\beta^\dagger - \beta\beta^\dagger\hat{\rho}_{cm}(t)\Big) \\
&+ \frac{Rg^2\tau^2\sin\phi\cos\phi}{2}\Big(2\alpha^\dagger\hat{\rho}_{cm}(t)\beta - \hat{\rho}_{cm}(t)\alpha^\dagger\beta - \alpha^\dagger\beta\hat{\rho}_{cm}(t)\Big) \\
&+ \frac{Rg^2\tau^2\sin\phi\cos\phi}{2}\Big(2\beta^\dagger\hat{\rho}_{cm}(t)\alpha - \hat{\rho}_{cm}(t)\alpha\beta^\dagger - \alpha\beta^\dagger\hat{\rho}_{cm}(t)\Big).
\end{aligned} \tag{7.45}$$

In the context of open quantum systems, the effect of the atom on the system is treated here as an interaction with the environment. The result is a quantum master equation in Lindblad form resulting from the interaction with a continuous beam of atoms. This can be linearly combined with the coherent evolution of the closed system, H_0, given by the van Neumann equation, where the partial trace has been taken over the atomic degrees of freedom. In doing this the ω_z-part turns into a constant value which can be absorbed by a shift of the zero-point energy. This leads to a master

equation of the form

$$\frac{d}{dt}\hat{\rho}_{cm}(t) = -i\left[H_0, \hat{\rho}_{cm}(t)\right] + \left.\frac{\partial\hat{\rho}_{cm}(t)}{\partial t}\right|_{atom}. \tag{7.46}$$

An additional possibility is considering other environments for the microwave resonator or mechanical oscillator, such as for example interacting with the thermal state of the environment [21].

7.4.1 Steady State of the system interacting with an atomic beam

As a first step in applying this formalism to the microwave resonator-mechanical oscillator system interacting with an atomic beam, we investigate the average polariton numbers that can be calculated. Naturally, with the master equation derived above, and assuming that the mechanical oscillator and microwave resonator are otherwise closed systems, we calculate the time-evolution of average values of interest, $\langle\hat{\alpha}^{(\dagger)}\rangle, \langle\hat{\beta}^{(\dagger)}\rangle$ and especially

$$\frac{d}{dt}\langle\hat{n}_\alpha\rangle = \frac{d}{dt}\langle\hat{\alpha}^\dagger\hat{\alpha}\rangle = \frac{d}{dt}Tr\left\{\alpha^\dagger\hat{\alpha}\hat{\rho}_{cm}(t)\right\} = Tr\left\{\alpha^\dagger\hat{\alpha}\frac{d}{dt}\hat{\rho}_{cm}(t)\right\}. \tag{7.47}$$

This can be done in a straight-forward manner by evaluating the expression with the time-derivative of the reduced density matrix, exploiting the cyclic property of the trace operator.

The set of equations of motion are therefore

$$\begin{aligned}\frac{d}{dt}\langle\hat{\alpha}^\dagger\hat{\alpha}\rangle &= g^2\tau^2\cos^2\phi(R-r)\langle\alpha^\dagger\alpha\rangle \\ &\quad+\frac{g^2\tau^2\sin\phi\cos\phi}{2}(R-r)\Big(\langle\alpha^\dagger\beta\rangle+\langle\alpha\beta^\dagger\rangle\Big) \\ &\quad+Rg^2\tau^2\cos^2\phi, \end{aligned} \tag{7.48}$$

$$\begin{aligned}\frac{d}{dt}\langle\hat{\beta}^\dagger\hat{\beta}\rangle &= g^2\tau^2\sin^2\phi(R-r)\langle\beta^\dagger\beta\rangle \\ &\quad+\frac{g^2\tau^2\sin\phi\cos\phi}{2}(R-r)\Big(\langle\alpha^\dagger\beta\rangle+\langle\alpha\beta^\dagger\rangle\Big) \\ &\quad+Rg^2\tau^2\sin^2\phi, \end{aligned} \tag{7.49}$$

$$\begin{aligned}\frac{d}{dt}\langle\hat{\alpha}^\dagger\hat{\beta}\rangle &= \Big(\frac{(R-r)g^2\tau^2}{2}+i(\Delta_\alpha-\Delta_\beta)\Big)\langle\alpha^\dagger\hat{\beta}\rangle \\ &\quad+\frac{(R-r)g^2\tau^2\sin\phi\cos\phi}{2}\Big(\langle\alpha^\dagger\alpha\rangle+\langle\beta^\dagger\beta\rangle\Big) \\ &\quad+Rg^2\tau^2\sin\phi\cos\phi, \end{aligned} \tag{7.50}$$

$$\begin{aligned}\frac{d}{dt}\langle\hat{\alpha}\hat{\beta}^\dagger\rangle &= \Big(\frac{(R-r)g^2\tau^2}{2}-i(\Delta_\alpha-\Delta_\beta)\Big)\langle\alpha\hat{\beta}^\dagger\rangle \\ &\quad+\frac{(R-r)g^2\tau^2\sin\phi\cos\phi}{2}\Big(\langle\alpha^\dagger\alpha\rangle+\langle\beta^\dagger\beta\rangle\Big) \\ &\quad+Rg^2\tau^2\sin\phi\cos\phi. \end{aligned} \tag{7.51}$$

Here, the two competing processes of atoms prepared in the higher circular Rydberg state introducing excitations into the system and atoms prepared in the lower circular state extracting excitations lead to a detailed balance for a non-equilibrium steady state number of polaritons. We calculate the steady state of the system, $\frac{d}{dt}\langle O\rangle \stackrel{!}{=} 0$, because of $\frac{d}{dt}\hat{\rho} \stackrel{!}{=} 0$. The steady state is reached after a time $t \to \infty$. For the microwave resonator-mechanical

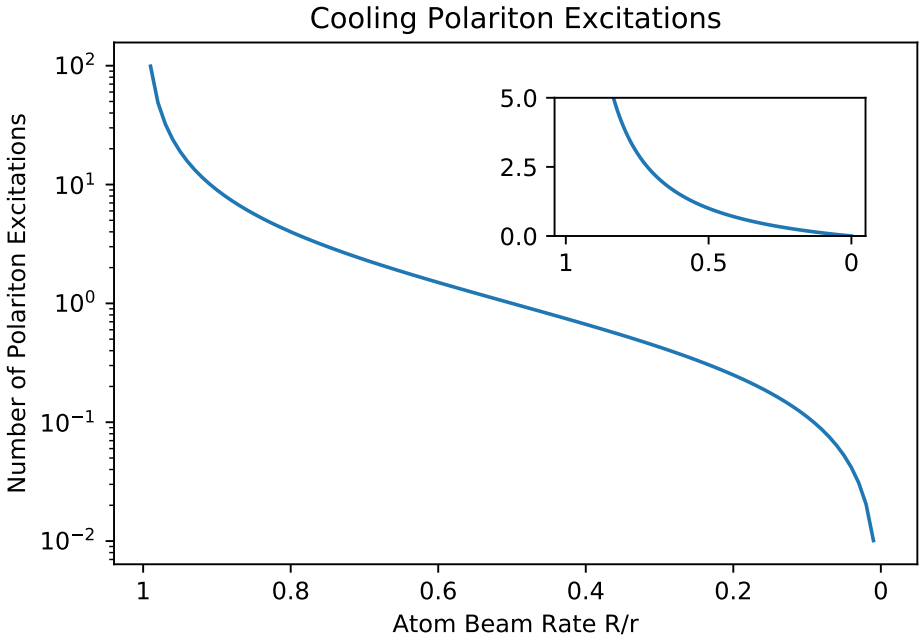

Figure 7.4: The effective cooling process for the polariton excitations $\langle \alpha^\dagger \alpha \rangle_{ss} + \langle \beta^\dagger \beta \rangle_{ss}$. Note that the x-axis is inversed in order to illustrate the effect for an increase in the rate of atoms prepared in the lower circular Rydberg state. The inset shows the same calculation with a linear y-axis.

oscillator system coupled to a reservoir of atoms via an atomic beam, we obtain for $\Delta_\alpha \neq \Delta_\beta$,

$$\langle \alpha^\dagger \alpha \rangle_{ss} = \langle \beta^\dagger \beta \rangle_{ss} = \frac{R}{r - R}. \tag{7.52}$$

In this case, the steady state does not contain any buildup of correlations between the different types of polariton because $\langle \alpha^\dagger \beta \rangle_{ss} = 0$. The number of polaritons in the steady state thermalizes with respect to the ratio of ground state and excited state atoms interacting with the microwave resonator-mechanical oscillator subsystem. From this one can immediately see that for an atomic beam where $R = 0$ atoms are prepared in the excited state, a

steady state of the system is eventually reached which contains neither α- nor β-polaritons. This therefore represents a possible way to effectively cool the nanomechanical oscillator. This result is not surprising considering we did not include the possibility of thermal heating due to the finite temperature of the environment.

7.4.2 Considering a Thermal Environment

To account for the coupling to a thermal environment it is assumed that the time of flight of the Rydberg atoms is short compared to their coherence times. Therefore they arrive at the cavity in their initially prepared state. The cavity and mechanical resonator however experience thermal heating due to their environment. We must therefore investigate how their individual dissipation rates affect the polariton states within the framework of the Lindblad master equation. The dissipator for the microwave resonator can be expressed as

$$D_{\mathrm{r}}[\rho] = \frac{\gamma_{\mathrm{r}}}{2}(N_{\mathrm{r}}+1)\left(2a\rho a^{\dagger} - a^{\dagger}a\rho - \rho a^{\dagger}a\right) + \frac{\gamma_{\mathrm{r}}}{2}N_{\mathrm{r}}\left(2a^{\dagger}\rho a - aa^{\dagger}\rho - \rho aa^{\dagger}\right), \quad (7.53)$$

where the operators $a^{(\dagger)}$ are the photon annihilation (creation) operators in the original Fock basis, γ_{r} is the dissipation rate of the resonator following from its quality factor Q_{r} and N_{r} is the number of photons in the resonator at thermal equilibrium with the environment at a temperature $T = 4$ K. Analogously, the dissipator for the mechanical oscillator is

$$D_{\mathrm{m}}[\rho] = \frac{\gamma_{\mathrm{m}}}{2}(N_{\mathrm{m}}+1)\left(2b\rho b^{\dagger} - b^{\dagger}b\rho - \rho b^{\dagger}b\right) + \frac{\gamma_{\mathrm{m}}}{2}N_{\mathrm{m}}\left(2b^{\dagger}\rho b - bb^{\dagger}\rho - \rho bb^{\dagger}\right). \quad (7.54)$$

These dissipators are expressed in terms of the polariton operators α and β. We can summarize these terms as the internal dissipator $D_{\mathrm{i}}[\rho] = D_{\mathrm{r}}[\rho] +$

$D_{\rm m}[\rho]$ such that

$$
\begin{aligned}
D_i[\rho] \quad &= \Big(\frac{\gamma_{\rm m}}{2}(N_{\rm m}+1)\sin^2\phi + \frac{\gamma_{\rm r}}{2}(N_{\rm r}+1)\cos^2\phi\Big)\Big(2\alpha\rho\alpha^\dagger - \alpha^\dagger\alpha\rho - \rho\alpha^\dagger\alpha\Big) \\
&+\Big(\frac{\gamma_{\rm m}}{2}N_{\rm m}\sin^2\phi + \frac{\gamma_{\rm r}}{2}N_{\rm r}\cos^2\phi\Big)\Big(2\alpha^\dagger\rho\alpha - \alpha\alpha^\dagger\rho - \rho\alpha\alpha^\dagger\Big) \\
&+\Big(\frac{\gamma_{\rm m}}{2}(N_{\rm m}+1)\cos^2\phi + \frac{\gamma_{\rm r}}{2}(N_{\rm r}+1)\sin^2\phi\Big)\Big(2\beta\rho\beta^\dagger - \beta^\dagger\beta\rho - \rho\beta^\dagger\beta\Big) \\
&+\Big(\frac{\gamma_{\rm m}}{2}N_{\rm m}\cos^2\phi + \frac{\gamma_{\rm r}}{2}N_{\rm r}\sin^2\phi\Big)\Big(2\beta^\dagger\rho\beta - \beta\beta^\dagger\rho - \rho\beta\beta^\dagger\Big) \\
&+\sin\phi\cos\phi\Big(\gamma_{\rm r}(N_{\rm r}+1) - \gamma_{\rm m}(N_{\rm m}+1)\Big)\Big(\alpha\rho\beta^\dagger + \beta\rho\alpha^\dagger\Big) \\
&+\sin\phi\cos\phi\Big(\gamma_{\rm r}N_{\rm r} - \gamma_{\rm m}N_{\rm m}\Big)\Big(\alpha^\dagger\rho\beta + \beta^\dagger\rho\alpha\Big) \qquad (7.55) \\
&-\sin\phi\cos\phi\Big(\gamma_{\rm r}(N_{\rm r}+\frac{1}{2}) - \gamma_{\rm m}(N_{\rm m}+\frac{1}{2})\Big)\Big(\alpha^\dagger\beta\rho + \rho\alpha^\dagger\beta + \alpha\beta^\dagger\rho + \rho\alpha\beta^\dagger\Big).
\end{aligned}
$$

The average thermal number of microwave resonator-photons and mechanical oscillator-phonons in the system can be expressed as

$$
\langle n\rangle_{\rm th} = \frac{1}{e^{\frac{\hbar\omega_{\rm r,m}}{k_BT}} - 1}. \qquad (7.56)
$$

Together with the dissipator resulting from the atomic interaction,

$$
\begin{aligned}
D_{\rm at}[\rho] \quad = \quad &\frac{rg^2\tau^2\cos^2\phi}{2}\Big(2\alpha\hat{\rho}\alpha^\dagger - \hat{\rho}\alpha^\dagger\alpha - \alpha^\dagger\alpha\hat{\rho}\Big) \\
&+\frac{Rg^2\tau^2\cos^2\phi}{2}\Big(2\alpha^\dagger\hat{\rho}\alpha - \hat{\rho}\alpha\alpha^\dagger - \alpha\alpha^\dagger\hat{\rho}\Big) \\
&+\frac{rg^2\tau^2\sin^2\phi}{2}\Big(2\beta\hat{\rho}\beta^\dagger - \hat{\rho}\beta^\dagger\beta - \beta^\dagger\beta\hat{\rho}\Big) \\
&+\frac{Rg^2\tau^2\sin^2\phi}{2}\Big(2\beta^\dagger\hat{\rho}\beta - \hat{\rho}\beta\beta^\dagger - \beta\beta^\dagger\hat{\rho}\Big) \\
&+rg^2\tau^2\sin\phi\cos\phi\Big(\alpha\hat{\rho}\beta^\dagger + \beta\hat{\rho}\alpha^\dagger\Big) \\
&+Rg^2\tau^2\sin\phi\cos\phi\Big(\alpha^\dagger\hat{\rho}\beta + \beta^\dagger\hat{\rho}\alpha\Big) \\
&-\frac{(r+R)g^2\tau^2\sin\phi\cos\phi}{2}\Big(\alpha^\dagger\beta\hat{\rho} + \hat{\rho}\alpha^\dagger\beta + \alpha\beta^\dagger\hat{\rho} + \hat{\rho}\alpha\beta^\dagger\Big),
\end{aligned} \qquad (7.57)
$$

which exhibits a symmetric structure. This leads to competing processes, the thermal heating of the system due to the environment and the cooling effect of Rydberg atoms prepared in the circular ground state absorbing excitations from the system and carrying them away.

Together with the fully diagonalized Hamiltonian for the system in the polariton basis, $H_0 = \omega_\alpha \alpha^\dagger \alpha + \omega_\beta \beta^\dagger \beta$, we can evaluate the equations of motion for the average polariton-numbers, which are described by the master equation

$$\dot{\rho} = i[\rho, H_0] + D_{\mathrm{i}}[\rho] + D_{\mathrm{at}}[\rho], \tag{7.58}$$

leading to the following set of equations of motion

$$\begin{aligned}
\frac{d}{dt}\langle \alpha^\dagger \hat{\alpha} \rangle &= \Big(\gamma_{\mathrm{m}} N_{\mathrm{m}} \sin^2\phi + \gamma_{\mathrm{r}} N_{\mathrm{r}} \cos^2\phi + R g^2 \tau^2 \cos^2\phi \Big) \\
&- \Big(\gamma_{\mathrm{m}} \sin^2\phi + \gamma_{\mathrm{r}} \cos^2\phi + (r-R) g^2 \tau^2 \cos^2\phi \Big) \langle \alpha^\dagger \alpha \rangle \\
&+ \sin\phi \cos\phi \Big(\frac{\gamma_{\mathrm{m}}}{2} - \frac{\gamma_{\mathrm{r}}}{2} + \frac{(R-r) g^2 \tau^2}{2} \Big) \Big(\langle \alpha^\dagger \beta \rangle + \langle \hat{\alpha} \beta^\dagger \rangle \Big),
\end{aligned} \tag{7.59}$$

$$\begin{aligned}
\frac{d}{dt}\langle \beta^\dagger \hat{\beta} \rangle &= \Big(\gamma_{\mathrm{m}} N_{\mathrm{m}} \cos^2\phi + \gamma_{\mathrm{r}} N_{\mathrm{r}} \sin^2\phi + R g^2 \tau^2 \sin^2\phi \Big) \\
&- \Big(\gamma_{\mathrm{m}} \cos^2\phi + \gamma_{\mathrm{r}} \sin^2\phi + (r-R) g^2 \tau^2 \sin^2\phi \Big) \langle \beta^\dagger \beta \rangle \\
&+ \sin\phi \cos\phi \Big(\frac{\gamma_{\mathrm{m}}}{2} - \frac{\gamma_{\mathrm{r}}}{2} + \frac{(R-r) g^2 \tau^2}{2} \Big) \Big(\langle \alpha^\dagger \beta \rangle + \langle \alpha \beta^\dagger \rangle \Big),
\end{aligned} \tag{7.60}$$

$$\begin{aligned}
\frac{d}{dt}\langle \hat{\alpha}^\dagger \hat{\beta} \rangle &= \Big(\frac{(R-r) g^2 \tau^2 - \gamma_{\mathrm{r}} - \gamma_{\mathrm{m}}}{2} + i(\omega_\alpha - \omega_\beta) \Big) \langle \hat{\alpha}^\dagger \beta \rangle \\
&+ \sin\phi \cos\phi \frac{(R-r) g^2 \tau^2 - \gamma_{\mathrm{r}} + \gamma_{\mathrm{m}}}{2} \Big(\langle \alpha^\dagger \hat{\alpha} \rangle + \langle \hat{\beta}^\dagger \beta \rangle \Big) \\
&+ \sin\phi \cos\phi \Big(\gamma_{\mathrm{r}} N_{\mathrm{r}} - \gamma_{\mathrm{m}} N_{\mathrm{m}} + R g^2 \tau^2 \Big)
\end{aligned} \tag{7.61}$$

$$= \Big(\frac{d}{dt} \langle \hat{\alpha} \hat{\beta}^\dagger \rangle \Big)^\dagger, \tag{7.62}$$

where it can be seen that the interaction between the two different types of polaritons can be driven, and possibly controlled, by the rate of incoming atoms prepared in the higher circular Rydberg state, R, and lower circular Rydberg state, r.

Evaluating this set of equations of motion in the steady state condition, $\frac{d}{dt}\langle\hat{A}\rangle_{\mathrm{ss}} \stackrel{!}{=} 0$, assuming the microwave resonator has been prepared in its vacuum state, $N_{\mathrm{r}} \approx 0$, as has been shown in Chapter 6, and assuming the Rydberg atoms have been prepared in the lower circular state, $R = 0$, leads to the steady-state solutions. An analytical solution can be obtained. However, the solution is too convoluted to be given here and therefore only the dependence of the analytical steady state solution of the average polariton number on the flux of atoms has been plotted in Fig. 7.5. The parameter set for the simulation is $\gamma_{\mathrm{m}}/\omega_{\mathrm{m}} = 0.01$, $\gamma_{\mathrm{r}}/\omega_{\mathrm{m}} = 0.05$, $g/\omega_{\mathrm{m}} = 10$, $G/\omega_{\mathrm{m}} = -15\tau = 0.05\omega_{\mathrm{m}}$, $\tilde{\Delta}_0/\omega_{\mathrm{m}} = -5$, and $N_{\mathrm{m}} = 40$. A reduction of the average polariton number can be observed, up to $\langle n_\alpha\rangle_{\mathrm{ss}} \approx 0.20$ and $\langle n_\alpha\rangle_{\mathrm{ss}} \approx 0.45$, respectively. The simulation carried out here serves as a proof of principle that optomechanical polariton modes can be emptied with an engineered reservoir of a beam of Rydberg atoms.

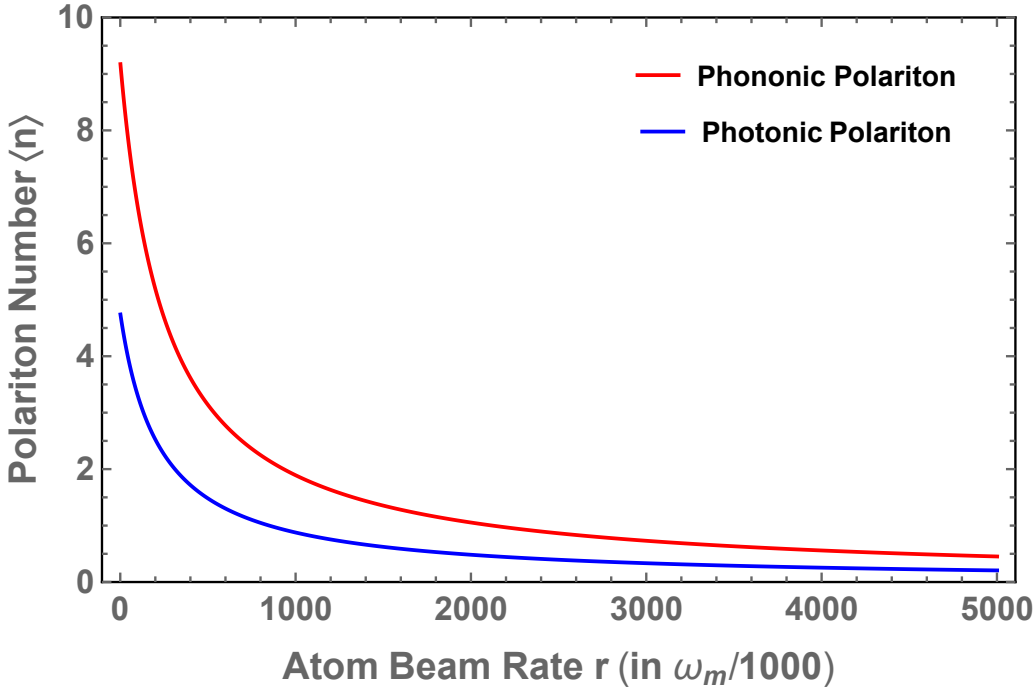

Figure 7.5: The dependence of the two polariton branches on the rate of the atomic beam,r, for $N_{\mathrm{m}} = 40$. Because $\gamma_{\mathrm{r}}/\gamma_{\mathrm{m}} = 5$, the average polariton numbers of the initial, thermal state are $\langle \alpha^{\dagger}\alpha \rangle_{\mathrm{th}} \approx 4.74$ (mainly photonic mode) and $\langle \beta^{\dagger}\beta \rangle_{\mathrm{th}} \approx 9.17$ (mainly phononic mode).

Chapter 8

Conclusions

In this thesis, first the behavior of strongly polarized ensembles of Rydberg atoms has been studied. Electrostatic dipole-dipole interactions between Rydberg atoms were investigated to realistically model the energy shifts within an atomic ensemble. The results of the calculation were compared to experimental data, yielding good qualitative agreement. This combination of experiments and calculations allowed the demonstration of a macroscopic screening of electrical noise that arose as a result of the local polarization of the Rydberg atoms.

Following this, the possibility to observe trapping states of a superconducting microwave resonator, and the implementation of quantum state preparation has been shown by varying controllable experimental parameters such as the flux of atoms, their velocity and spatial distribution, or the detuning of the atomic transition frequency from the fundamental frequency of the resonator. These results have demonstrated, for example, that it is possible to measure the velocity distribution as well as the spatial distribution of a gas-phase ensemble of Rydberg atoms by monitoring the

state of the transmission line resonator interacting with the atomic beam. However, this formalism is limited to diffuse atomic beams with at most one atom interacting with the transmission line resonator at any time.

A numerical method was then developed to show that in a realistic experimental setting the average number of thermal photons of the resonator, $\langle n \rangle_{\text{th}} \approx 4$, can be significantly reduced to $\langle n \rangle_{\text{ss}} = 0.006$ with a dense beam of atoms prepared in circular Rydberg states. This result paves the way for highly efficient single-photon experiments in hybrid quantum information processing. This numerical formalism, applied in order to simulate a dense beam of Rydberg atoms under realistic experimental conditions, allows for the measurement of correlations between the microwave resonator Fock states and a chosen number of atoms. This could lead to the realization of Schrödinger cat or squeezed states in the resonator once the optimal experimental parameters for the preparation of such quantum states have been identified.

Finally, an analytical formalism has been derived to engineer a quantum reservoir of atoms coupled to an optomechanical system. Through this work, it has been shown that it is possible to empty optomechanical polariton modes with a beam of atoms. However, a more in-depth investigation needs to be carried out in order to realize the potential of this method.

As a proposed next step in the research presented here, the application of the numerical formalism derived to describe the photon-phonon system could be extended to entangle specific states of the mechanical oscillator and microwave resonator, offering a route to study the implementation of protocols for quantum state transfer between photons and phonons me-

diated by Rydberg atoms. Additionally, a formalism could be derived for QND-measurements of the optomechanical system using Rydberg atoms. Another direction of interest is to include effects of electric dipole-dipole interactions between Rydberg atoms in the formalism developed to describe the coupling of a dense atomic beam to a microwave resonator. In general it is foreseeable to adapt and apply this numerical formalism to various hybrid quantum systems where the interaction with an atomic beam is continuously switched on and off due to the presence, or absence, of an atom. This atom does not have to be a pure two-level system, but could also be, e.g., a three-level lambda system. Extending the formalism in this way might open new possibilities for quantum state preparation, quantum computation and quantum communication with different hybrid quantum systems that are coupled to beams of atoms.

Bibliography

[1] M. Abdi, M. Pernpeintner, R. Gross, H. Huebl, and M. J. Hartmann. Quantum state engineering with circuit electromechanical three-body interactions. Physical Review Letters, 114(17):173602, 2015.

[2] K. Afrousheh, P. Bohlouli-Zanjani, D. Vagale, A. Mugford, M. Fedorov, and J. D. D. Martin. Spectroscopic observation of resonant electric dipole-dipole interactions between cold Rydberg atoms. Physical Review Letters, 93:233001, Nov 2004.

[3] R. Alicki. Invitation to quantum dynamical semigroups. In Dynamics of Dissipation, pages 239–264. Springer, 2002.

[4] L. Allen and J. H. Eberly. Optical resonance and two-level atoms, volume 28. Courier Corporation, 1987.

[5] D. Anderson, A. Schwarzkopf, R. Sapiro, and G. Raithel. Production and trapping of cold circular rydberg atoms. Physical Review A, 88(3):031401, 2013.

[6] W. R. Anderson, J. R. Veale, and T. F. Gallagher. Resonant dipole-dipole energy transfer in a nearly frozen Rydberg gas. Physical Review Letters, 80:249–252, Jan 1998.

[7] N. Bar-Gill, L. M. Pham, A. Jarmola, D. Budker, and R. L. Walsworth. Solid-state electronic spin coherence time approaching one second. Nature Communications, 4:1743, 2013.

[8] M. Beck, J. Isaacs, D. Booth, J. Pritchard, M. Saffman, and R. McDermott. Optimized coplanar waveguide resonators for a superconductor–atom interface. Applied Physics Letters, 109(9):092602, 2016.

[9] L. Béguin, A. Vernier, R. Chicireanu, T. Lahaye, and A. Browaeys. Direct measurement of the van der Waals interaction between two Rydberg atoms. Physical Review Letters, 110(26):263201, 2013.

[10] V. Bendkowsky, B. Butscher, J. Nipper, J. P. Shaffer, R. Löw, and T. Pfau. Observation of ultralong-range Rydberg molecules. Nature, 458(7241):1005, 2009.

[11] H. A. Bethe and E. E. Salpeter. Quantum mechanics of one-and two-electron atoms. Springer Science & Business Media, 2012.

[12] A. Blais, R.-S. Huang, A. Wallraff, S. M. Girvin, and R. J. Schoelkopf. Cavity quantum electrodynamics for superconducting electrical circuits: An architecture for quantum computation. Physical Review A, 69(6):062320, 2004.

[13] J. Bochmann, A. Vainsencher, D. D. Awschalom, and A. N. Cleland. Nanomechanical coupling between microwave and optical photons. Nature Physics, 9(11):712–716, 2013.

[14] D. Booth, S. Rittenhouse, J. Yang, H. Sadeghpour, and J. Shaffer. Production of trilobite Rydberg molecule dimers with kilo-Debye permanent electric dipole moments. Science, 348(6230):99–102, 2015.

[15] S. Bose, K. Jacobs, and P. Knight. Preparation of nonclassical states in cavities with a moving mirror. Physical Review A, 56(5):4175, 1997.

[16] R. Brecha, G. Raithel, C. Wagner, and H. Walther. Circular Rydberg states with very large n. Optics Communications, 102(3-4):257–264, 1993.

[17] I. N. Bronstein, J. Hromkovic, B. Luderer, H.-R. Schwarz, J. Blath, A. Schied, S. Dempe, G. Wanka, and S. Gottwald. Taschenbuch der Mathematik, volume 1. Springer-Verlag, 2012.

[18] M. Brune, F. Schmidt-Kaler, A. Maali, J. Dreyer, E. Hagley, J. Raimond, and S. Haroche. Quantum rabi oscillation: A direct test of field quantization in a cavity. Physical Review Letters, 76(11):1800, 1996.

[19] A. Carmele, B. Vogell, K. Stannigel, and P. Zoller. Opto-nanomechanics strongly coupled to a rydberg superatom: coherent versus incoherent dynamics. New Journal of Physics, 16(6):063042, 2014.

[20] H. Carmichael. An open systems approach to quantum optics: Lectures presented at the Université Libre de Bruxelles, October 28 to November 4, 1991, volume 18. Springer Science & Business Media, 1993.

[21] H. J. Carmichael. Statistical methods in quantum optics 1: Master equations and Fokker-Planck equations (Theoretical and Mathematical Physics), 2003.

[22] C. Carr, R. Ritter, C. Wade, C. S. Adams, and K. J. Weatherill. Nonequilibrium phase transition in a dilute Rydberg ensemble. Physical Review Letters, 111(11):113901, 2013.

[23] L. D. Carr, D. DeMille, R. V. Krems, and J. Ye. Cold and ultracold molecules: Science, technology and applications. New Journal of Physics, 11(5):055049, 2009.

[24] F. Casas, A. Murua, and M. Nadinic. Efficient computation of the Zassenhaus formula. Computer Physics Communications, 183(11):2386–2391, 2012.

[25] J. Chan, T. M. Alegre, A. H. Safavi-Naeini, J. T. Hill, A. Krause, S. Gröblacher, M. Aspelmeyer, and O. Painter. Laser cooling of a nanomechanical oscillator into its quantum ground state. Nature, 478(7367):89, 2011.

[26] M. Cheret, F. Roussel, T. Bolzinger, G. Spiess, J. Hare, and M. Gross. Barium circular atoms prepared by the crossed-field method. EPL (Europhysics Letters), 9(3):231, 1989.

[27] J. Cirac, P. Zoller, H. Kimble, and H. Mabuchi. Quantum state transfer and entanglement distribution among distant nodes in a quantum network. Physical Review Letters, 78(16):3221, 1997.

[28] C. Cohen-Tannoudji, B. Diu, and F. Laloe. Quantum mechanics, volume 2. Quantum Mechanics, Volume 2, by Claude Cohen-Tannoudji, Bernard Diu, Frank Laloe, pp. 626. ISBN 0-471-16435-6. Wiley-VCH, June 1986., page 626, 1986.

[29] D. Delande and J. Gay. A new method for producing circular Rydberg states. EPL (Europhysics Letters), 5(4):303, 1988.

[30] A. Deller, A. Alonso, B. Cooper, S. Hogan, and D. Cassidy. lectrostatically guided Rydberg positronium. Physical Review Letters, 117(7):073202, 2016.

[31] M. H. Devoret et al. Quantum fluctuations in electrical circuits. Les Houches, Session LXIII, 7(8), 1995.

[32] G. W. Drake. High precision theory of atomic helium. Physica Scripta, 1999(T83):83, 1999.

[33] A. Einstein. Strahlungsemission und -absorption nach der Quantentheorie. Deutsche Physikalische Gesellschaft, 18:318–323, 1916.

[34] S. M. Farooqi, D. Tong, S. Krishnan, J. Stanojevic, Y. Zhang, J. Ensher, A. Estrin, C. Boisseau, R. Côté, E. Eyler, et al. Long-range molecular resonances in a cold Rydberg gas. Physical Review Letters, 91(18):183002, 2003.

[35] T. Förster. Zwischenmolekulare Energiewanderung und Fluoreszenz. Annalen der Physik, 437(1-2):55–75, 1948.

[36] T. F. Gallagher. Rydberg atoms, volume 3. Cambridge University Press, 2005.

[37] T. F. Gallagher and P. Pillet. Dipole–dipole interactions of Rydberg atoms. Advances in Atomic, Molecular, and Optical Physics, 56:161–218, 2008.

[38] B. T. Gard, K. Jacobs, R. McDermott, and M. Saffman. Microwave-to-optical frequency conversion using a cesium atom coupled to a superconducting resonator. Physical Review A, 96(1):013833, 2017.

[39] C. Gardiner and P. Zoller. Quantum noise: A handbook of Markovian and non-Markovian quantum stochastic methods with applications to quantum optics, volume 56. Springer Science & Business Media, 2004.

[40] J. Gibbard and T. Softley. Resonant charge transfer of hydrogen Rydberg atoms incident at a metallic sphere. Journal of Physics B: Atomic, Molecular and Optical Physics, 49(11):114004, 2016.

[41] S. M. Girvin. Circuit QED: Superconducting qubits coupled to microwave photons. Proceedings of the 2011 Les Houches Summer School, 2011.

[42] M. Göppl, A. Fragner, M. Baur, R. Bianchetti, S. Filipp, J. Fink, P. Leek, G. Puebla, L. Steffen, and A. Wallraff. Coplanar waveguide res-

onators for circuit quantum electrodynamics. Journal of Applied Physics, 104(11):113904, 2008.

[43] C. H. Greene, A. Dickinson, and H. Sadeghpour. Creation of polar and nonpolar ultra-long-range Rydberg molecules. Physical Review Letters, 85(12):2458, 2000.

[44] D. J. Griffiths and D. F. Schroeter. Introduction to quantum mechanics. Cambridge University Press, 2018.

[45] H. G. Grimm and A. Sommerfeld. Über den. zusammenhang des abschlusses der elektronengruppen im atom mit den chemischen valenzzahlen. Zeitschrift für Physik, 36(1):36–59, 1926.

[46] T. Halfmann, J. Koensgen, and K. Bergmann. A source for a high-intensity pulsed beam of metastable helium atoms. Measurement Science and Technology, 11(10):1510, 2000.

[47] S. Haroche. Nobel lecture: Controlling photons in a box and exploring the quantum to classical boundary. Reviews of Modern Physics, 85(3):1083, 2013.

[48] M. J. Hartmann. Polariton crystallization in driven arrays of lossy nonlinear resonators. Physical Review Letters, 104(11):113601, 2010.

[49] C. Hermann-Avigliano, R. C. Teixeira, T. Nguyen, T. Cantat-Moltrecht, G. Nogues, I. Dotsenko, S. Gleyzes, J. Raimond, S. Haroche, and M. Brune. Long coherence times for rydberg qubits on a superconducting atom chip. Physical Review A, 90(4):040502, 2014.

[50] S. Hill, C. Haich, Z. Zhou, P. Nordlander, and F. Dunning. Ionization of xenon Rydberg atoms at a metal surface. Physical Review Letters, 85(25):5444, 2000.

[51] S. Hogan, J. Agner, F. Merkt, T. Thiele, S. Filipp, and A. Wallraff. Driving Rydberg-Rydberg transitions from a coplanar microwave waveguide. Physical review letters, 108(6):063004, 2012.

[52] S. Hogan and F. Merkt. Demonstration of three-dimensional electrostatic trapping of state-selected Rydberg atoms. Physical Review Letters, 100(4):043001, 2008.

[53] S. D. Hogan. Cold atoms and molecules by zeeman deceleration and rydberg-stark deceleration. 2012.

[54] S. D. Hogan. Rydberg-Stark deceleration of atoms and molecules. EPJ Techniques and Instrumentation, 3(1):2, 2016.

[55] S. D. Hogan, C. Seiler, and F. Merkt. Rydberg-state-enabled deceleration and trapping of cold molecules. Physical Review Letters, 103(12):123001, 2009.

[56] I.-C. Hoi, C. M. Wilson, G. Johansson, T. Palomaki, B. Peropadre, and P. Delsing. Demonstration of a single-photon router in the microwave regime. Phys. Rev. Lett., 107:073601, Aug 2011.

[57] C. Hood, T. Lynn, A. Doherty, A. Parkins, and H. Kimble. The atom-cavity microscope: Single atoms bound in orbit by single photons. Science, 287(5457):1447–1453, 2000.

[58] A. A. Houck, H. E. Türeci, and J. Koch. On-chip quantum simulation with superconducting circuits. Nature Physics, 8(4):292–299, 2012.

[59] R. G. Hulet, E. S. Hilfer, and D. Kleppner. Inhibited spontaneous emission by a Rydberg atom. Physical review letters, 55(20):2137, 1985.

[60] R. G. Hulet and D. Kleppner. Rydberg atoms in" circular" states. Physical Review Letters, 51(16):1430, 1983.

[61] D. Jaksch, J. Cirac, P. Zoller, S. Rolston, R. Côté, and M. Lukin. Fast quantum gates for neutral atoms. Physical Review Letters, 85(10):2208, 2000.

[62] E. T. Jaynes and F. W. Cummings. Comparison of quantum and semiclassical radiation theories with application to the beam maser. Proceedings of the IEEE, 51(1):89–109, 1963.

[63] P. Kharel, Y. Chu, M. Power, W. H. Renninger, R. J. Schoelkopf, and P. T. Rakich. Ultra-high-q phononic resonators on-chip at cryogenic temperatures. APL Photonics, 3(6):066101, 2018.

[64] J. Koch, A. A. Houck, K. Le Hur, and S. Girvin. Time-reversal-symmetry breaking in circuit-QED-based photon lattices. Physical Review A, 82(4):043811, 2010.

[65] G. Kurizki, P. Bertet, Y. Kubo, K. Mølmer, D. Petrosyan, P. Rabl, and J. Schmiedmayer. Quantum technologies with hybrid systems. Proceedings of the National Academy of Sciences, page 201419326, 2015.

[66] P. Lancuba and S. Hogan. Guiding Rydberg atoms above surface-based transmission lines. Physical Review A, 88(4):043427, 2013.

[67] P. Lancuba and S. Hogan. Transmission-line decelerators for atoms in high Rydberg states. Physical Review A, 90(5):053420, 2014.

[68] P. Lancuba and S. Hogan. Electrostatic trapping and in situ detection of rydberg atoms above chip-based transmission lines. Journal of Physics B: Atomic, Molecular and Optical Physics, 49(7):074006, 2016.

[69] J. Liang, M. Gross, P. Goy, and S. Haroche. Circular Rydberg-state spectroscopy. Physical Review A, 33(6):4437, 1986.

[70] G. Lloyd, S. Procter, and T. Softley. Ionization of hydrogen Rydberg molecules at a metal surface. Physical Review Letters, 95(13):133202, 2005.

[71] D. M. Lubman, C. T. Rettner, and R. N. Zare. How isolated are molecules in a molecular beam? The Journal of Physical Chemistry, 86(7):1129–1135, 1982.

[72] M. D. Lukin, M. Fleischhauer, R. Cote, L. M. Duan, D. , J. I. Cirac, and P. Zoller. Dipole blockade and quantum information processing in mesoscopic atomic ensembles. Phys. Rev. Lett., 87:037901, Jun 2001.

[73] R. Lutwak, J. Holley, P. P. Chang, S. Paine, D. Kleppner, and T. Ducas. Circular states of atomic hydrogen. Physical Review A, 56(2):1443, 1997.

[74] S. Mancini, V. Man'ko, and P. Tombesi. Ponderomotive control of quantum macroscopic coherence. Physical Review A, 55(4):3042, 1997.

[75] L. Mandel. Photon occupation numbers in black body radiation. JOSA, 69(7):1038–1039, 1979.

[76] R. Manenti, A. F. Kockum, A. Patterson, T. Behrle, J. Rahamim, G. Tancredi, F. Nori, and P. J. Leek. Circuit quantum acoustodynamics with surface acoustic waves. Nature communications, 8(1):975, 2017.

[77] P. Meystre, G. Rempe, and H. Walther. Very-low-temperature behavior of a micromaser. Optics Letters, 13(12):1078–1080, 1988.

[78] S. A. Miller, D. A. Anderson, and G. Raithel. Radio-frequency-modulated Rydberg states in a vapor cell. New Journal of Physics, 18(5):053017, 2016.

[79] D. Møller, L. B. Madsen, and K. Mølmer. Quantum gates and multiparticle entanglement by Rydberg excitation blockade and adiabatic passage. Physical Review Letters, 100(17):170504, 2008.

[80] A. Morgan, V. Zhelyazkova, and S. Hogan. Preparation of circular rydberg states in helium with $n \geq 70$ using a modified version of the crossed-fields method. Physical Review A, 98(4):043416, 2018.

[81] T. Niemczyk, F. Deppe, H. Huebl, E. Menzel, F. Hocke, M. Schwarz, J. Garcia-Ripoll, D. Zueco, T. Hümmer, E. Solano, et al. Circuit quan-

tum electrodynamics in the ultrastrong-coupling regime. Nature Physics, 6(10):772, 2010.

[82] A. Nussenzweig, J. Hare, A. Steinberg, L. Moi, M. Gross, and S. Haroche. A continuous beam of circular Rydberg atoms for fundamental tests and applications in metrology. EPL (Europhysics Letters), 14(8):755, 1991.

[83] H. Paik, D. Schuster, L. S. Bishop, G. Kirchmair, G. Catelani, A. Sears, B. Johnson, M. Reagor, L. Frunzio, L. Glazman, et al. Observation of high coherence in josephson junction qubits measured in a three-dimensional circuit qed architecture. Physical Review Letters, 107(24):240501, 2011.

[84] W. K. Panofsky and M. Phillips. Classical electricity and magnetism. Courier Corporation, 2005.

[85] H. Park, T. Gallagher, and P. Pillet. Microwave pump-probe spectroscopy of the dipole-dipole interaction in a cold Rydberg gas. Physical Review A, 93(5):052501, 2016.

[86] H. Park, P. Tanner, B. Claessens, E. Shuman, and T. Gallagher. Dipole-dipole broadening of Rb n s- n p microwave transitions. Physical Review A, 84(2):022704, 2011.

[87] W. Pauli. Über das Wasserstoffspektrum vom Standpunkt der neuen Quantenmechanik. Z. Phys, 36:336–363, 1926.

[88] D. Petrosyan, G. Bensky, G. Kurizki, I. Mazets, J. Majer, and J. Schmiedmayer. Reversible state transfer between superconducting qubits and atomic ensembles. Physical Review A, 79(4):040304, 2009.

[89] D. Petrosyan and M. Fleischhauer. Quantum information processing with single photons and atomic ensembles in microwave coplanar waveguide resonators. Physical review letters, 100(17):170501, 2008.

[90] J. R. Petta, A. C. Johnson, J. M. Taylor, E. A. Laird, A. Yacoby, M. D. Lukin, C. M. Marcus, M. P. Hanson, and A. C. Gossard. Coherent manipulation of coupled electron spins in semiconductor quantum dots. Science, 309(5744):2180–2184, 2005.

[91] C. Picken, R. Legaie, K. McDonnell, and J. Pritchard. Entanglement of neutral-atom qubits with long ground-Rydberg coherence times. arXiv preprint arXiv:1808.04755, 2018.

[92] S. Pielawa, L. Davidovich, D. Vitali, and G. Morigi. Engineering atomic quantum reservoirs for photons. Phys. Rev. A, 81:043802, Apr 2010.

[93] M. Planck. Über das Gesetz der Energieverteilung im Normalspektrum. Annalen der Physik, 309(3):553–563, 1901.

[94] P. Rabl, D. DeMille, J. M. Doyle, M. D. Lukin, R. Schoelkopf, and P. Zoller. Hybrid quantum processors: Molecular ensembles as quantum memory for solid state circuits. Physical Review Letters, 97(3):033003, 2006.

[95] J. Raimond, G. Vitrant, and S. Haroche. Spectral line broadening due to the interaction between very excited atoms:'The dense Rydberg gas'. Journal of Physics B: Atomic and Molecular Physics, 14(21):L655, 1981.

[96] S. Rips and M. J. Hartmann. Quantum information processing with nanomechanical qubits. Physical Review Letters, 110(12):120503, 2013.

[97] M. Saffman. Quantum computing with atomic qubits and Rydberg interactions: progress and challenges. Journal of Physics B: Atomic, Molecular and Optical Physics, 49(20):202001, 2016.

[98] M. Saffman, T. G. Walker, and K. Mølmer. Quantum information with Rydberg atoms. Rev. Mod. Phys., 82:2313–2363, Aug 2010.

[99] L. Sárkány, J. Fortágh, and D. Petrosyan. Faithful state transfer between two-level systems via an actively cooled finite-temperature cavity. Physical Review A, 97(3):032341, 2018.

[100] D. Schuster, A. Sears, E. Ginossar, L. DiCarlo, L. Frunzio, J. Morton, H. Wu, G. Briggs, B. Buckley, D. Awschalom, and R. Schoelkopf. High-cooperativity coupling of electron-spin ensembles to superconducting cavities. Physical Review Letters, 105(14):140501, 2010.

[101] C. Seiler, J. A. Agner, P. Pillet, and F. Merkt. Radiative and collisional processes in translationally cold samples of hydrogen Rydberg atoms studied in an electrostatic trap. Journal of Physics B: Atomic, Molecular and Optical Physics, 49(9):094006, 2016.

[102] R. E. Smalley, L. Wharton, and D. H. Levy. Molecular optical spectroscopy with supersonic beams and jets. Accounts of Chemical Research, 10(4):139–145, 1977.

[103] K. Smith, F. Kellert, R. Rundel, F. Dunning, and R. Stebbings. Discrete energy transfer in collisions of Xe (nf) Rydberg atoms with N H 3 molecules. Physical Review Letters, 40(21):1362, 1978.

[104] H. P. Specht, C. Nölleke, A. Reiserer, M. Uphoff, E. Figueroa, S. Ritter, and G. Rempe. A single-atom quantum memory. Nature, 473(7346):190–193, 2011.

[105] H. Spohn. An algebraic condition for the approach to equilibrium of an open n-level system. Letters in Mathematical Physics, 2(1):33–38, 1977.

[106] R. C. Teixeira, C. Hermann-Avigliano, T. L. Nguyen, T. Cantat-Moltrecht, J.-M. Raimond, S. Haroche, S. Gleyzes, and M. Brune. Microwaves probe dipole blockade and van der Waals forces in a cold Rydberg gas. Physical Review Letters, 115(1):013001, 2015.

[107] J. Teufel, T. Donner, D. Li, J. Harlow, M. Allman, K. Cicak, A. Sirois, J. D. Whittaker, K. Lehnert, and R. W. Simmonds. Sideband cooling of micromechanical motion to the quantum ground state. Nature, 475(7356):359, 2011.

[108] N. Thaicharoen, L. Gonçalves, and G. Raithel. Atom-pair kinetics with strong electric-dipole interactions. Physical Review Letters, 116(21):213002, 2016.

[109] T. Thiele, S. Filipp, J. A. Agner, H. Schmutz, J. Deiglmayr, M. Stammeier, P. Allmendinger, F. Merkt, and A. Wallraff. Manipulating rydberg atoms close to surfaces at cryogenic temperatures. Physical Review A, 90(1):013414, 2014.

[110] P. Treutlein, D. Hunger, S. Camerer, T. W. Hänsch, and J. Reichel. Bose-einstein condensate coupled to a nanomechanical resonator on an atom chip. Physical Review Letters, 99(14):140403, 2007.

[111] B. T. Varcoe, S. Brattke, M. Weidinger, and H. Walther. Preparing pure photon number states of the radiation field. Nature, 403(6771):743–746, 2000.

[112] E. Verhagen, S. Deléglise, S. Weis, A. Schliesser, and T. J. Kippenberg. Quantum-coherent coupling of a mechanical oscillator to an optical cavity mode. Nature, 482(7383):63, 2012.

[113] D. Vion, A. Aassime, A. Cottet, P. Joyez, H. Pothier, C. Urbina, D. Esteve, and M. H. Devoret. Manipulating the quantum state of an electrical circuit. Science, 296(5569):886–889, 2002.

[114] E. Vliegen, H. J. Wörner, T. Softley, and F. Merkt. Nonhydrogenic effects in the deceleration of Rydberg atoms in inhomogeneous electric fields. Physical Review Letters, 92(3):033005, 2004.

[115] A. Wallraff, D. I. Schuster, A. Blais, L. Frunzio, R.-S. Huang, J. Majer, S. Kumar, S. M. Girvin, and R. J. Schoelkopf. Strong coupling of a single photon to a superconducting qubit using circuit quantum electrodynamics. Nature, 431(7005):162, 2004.

[116] D. F. Walls and G. J. Milburn. Quantum optics. Springer Science & Business Media, 2007.

[117] L. Wang, H. Zhang, L. Zhang, C. Li, Y. Yang, J. Zhao, G. Raithel, and S. Jia. Dipolar Rydberg-atom gas prepared by adiabatic passage through an avoided crossing. New Journal of Physics, 17(6):063011, 2015.

[118] T. Wilk, A. Gaëtan, C. Evellin, J. Wolters, Y. Miroshnychenko, P. Grangier, and A. Browaeys. Entanglement of two individual neutral atoms using Rydberg blockade. Physical Review Letters, 104(1):010502, 2010.

[119] D. J. Wineland. Nobel lecture: Superposition, entanglement, and raising schrödinger's cat. Reviews of Modern Physics, 85(3):1103, 2013.

[120] H. Wu, R. E. George, J. H. Wesenberg, K. Mølmer, D. I. Schuster, R. J. Schoelkopf, K. M. Itoh, A. Ardavan, J. J. Morton, and G. A. D. Briggs. Storage of multiple coherent microwave excitations in an electron spin ensemble. Physical Review Letters, 105(14):140503, 2010.

[121] Z.-L. Xiang, S. Ashhab, J. You, and F. Nori. Hybrid quantum circuits: Superconducting circuits interacting with other quantum systems. Reviews of Modern Physics, 85(2):623, 2013.

[122] Z.-L. Xiang, S. Ashhab, J. Q. You, and F. Nori. Hybrid quantum circuits: Superconducting circuits interacting with other quantum systems. Rev. Mod. Phys., 85:623–653, Apr 2013.

[123] Y. Yamakita, S. Procter, A. Goodgame, T. Softley, and F. Merkt. Deflection and deceleration of hydrogen Rydberg molecules in inhomogeneous electric fields. The Journal of Chemical Physics, 121(3):1419–1431, 2004.

[124] J. You and F. Nori. Quantum information processing with superconducting qubits in a microwave field. Physical Review B, 68(6):064509, 2003.

[125] V. Zhelyazkova and S. Hogan. Probing interactions between Rydberg atoms with large electric dipole moments in amplitude-modulated electric fields. Physical Review A, 92(1):011402, 2015.

[126] V. Zhelyazkova and S. Hogan. Rydberg–Stark states in oscillating electric fields. Molecular Physics, 113(24):3979–3991, 2015.

[127] V. Zhelyazkova and S. Hogan. Preparation of circular Rydberg states in helium using the crossed-fields method. Physical Review A, 94(2):023415, 2016.

[128] V. Zhelyazkova, R. Jirschik, and S. Hogan. Mean-field energy-level shifts and dielectric properties of strongly polarized Rydberg gases. Physical Review A, 94(5):053418, 2016.

Appendix A

Probability of N Atoms interacting with the Resonator

In this appendix a validation for the truncation of the numerical approach in Chapter 6 to at most five atoms interacting with the resonator at any time is provided. This is done by calulcating the probability of six or more atoms interacting with the resonator at the same time and showing that this probability is negligible within the context of the experimental parameters discussed.

As has been shown in Eq. (6.4), the probabilty of zero atoms entering the resonator can be calculated as

$$p_0 = \frac{1 - 2r\Delta t}{1 - r\Delta t}. \tag{A.1}$$

For any number of atoms $n \geq 1$ arriving at the resonator within the same time step, Δt, one can write

$$p_n = (r\Delta t)^n. \tag{A.2}$$

Considering a time interval on the order of the interaction time, $\tau = k\Delta t$, any permutation of n atoms that interact with the resonator during the interaction time must be calculated. Therefore, the probabilty of zero atoms interacting with the resonator over the time interval τ is

$$\begin{aligned} P_0(\tau) &= (p_0)^{\tau/\Delta t} \\ &= \left(\frac{1 - 2r\Delta t}{1 - r\Delta t}\right)^k . \end{aligned} \tag{A.3}$$

The probability of one atom interacting with the resonator during the time interval can be expressed as

$$\begin{aligned} P_1(k\Delta t) &= \binom{k}{1} (p_0)^{k-1} p_1 \\ &= k\left(\frac{1 - 2r\Delta t}{1 - r\Delta t}\right)^{k-1} r\Delta t, \end{aligned} \tag{A.4}$$

where the binomial coefficient prefactor accounts for the combinatorics, i.e., the k different time steps in which the atom may enter the resonator. In order to calculate the probabilities of more than one atom interacting with the resonator at any given time, the binomial distribution must be extended to a multinomial distribution. This is due to the fact that, for example, in the case of n atoms, the probabilities of

- all n atoms beginning to cross the resonator during the same time step,
- $(n - 1)$ atoms arriving during one time step and one atom arriving during a different time step
- $(n - 2)$ atoms arriving during one time step and either (i) two atoms arrive as a pair during a different time step, or (ii) one atom each arrives at another different time step

- $(n-3)$ atoms arriving during one time step and all combinations of the three other atoms arriving during other time steps
- continuing via $(n-4)$, $(n-5)$, ... that must be extended to all the atoms arriving each during a different time step one by one

must all be accounted for.
For one realization of these cases, the probability of n atoms being multinomially distributed can be calculated as

$$P_n(\text{one} - \text{realization}) = \frac{(i+j+l+\cdots+z)!}{i!\,j!\,l!\,\ldots z!}(p_0)^i(p_1)^j(p_2)^l\ldots(p_n)^z. \quad \text{(A.5)}$$

Here i is the number of time steps during which no atom enters the resonator, j is the number of time steps with one atom entering, m with two atoms entering and so forth, with

$$i+j+l+\cdots+z = \frac{\tau}{\Delta t} \quad \text{(A.6)}$$

summing up to the number of time steps the time interval, i.e., the interaction time, is split into. There exists a restriction for the possible values each number of time steps can take on. For example, the maximum number of time steps during which a single atom enters the resonator is $j \leq n$. The maximum number of time steps during which two atoms enter is $l \leq n/2$. For three atoms entering, the limit is $m \leq n/3$. The limits for four and more atoms entering are calculated in similar fashion. The number of time steps during which no atom enters is then self-consistently obtained from Eq. (A.6) to be

$$i = \frac{\tau}{\Delta t} - (j+l+\cdots+z)\,. \quad \text{(A.7)}$$

The probabilities for all possible, unordered combinations of $i, j, \ldots z \in \mathbb{N}$ for a given number of atoms, n, are calculated in this manner and then added. The result obtained in this way is the probability, $P_n(\tau)$, of n atoms interacting with the resonator at the same time within the time interval of the interaction time, τ.

Therefore the probabilities of having $2, 3, 4$ or 5 atoms interact with the resonator at the same time over k time steps are expressed as

$$P_2(\tau) = \frac{k(k-1)}{2} (p_0)^{k-2} (p_1)^2 + k (p_0)^{k-1} p_2, \tag{A.8}$$

$$\begin{aligned} P_3(\tau) = & \frac{k(k-1)(k-2)}{6} (p_0)^{k-3} (p_1)^3 + k(k-1) (p_0)^{k-2} p_1 p_2 \\ & + k (p_0)^{k-1} p_3, \end{aligned} \tag{A.9}$$

$$\begin{aligned} P_4(\tau) = & \frac{k(k-1)(k-2)(k-3)}{24} (p_0)^{k-4} (p_1)^4 + \frac{k(k-1)(k-2)}{2} (p_0)^{k-3} (p_1)^2 p_2 \\ & + k(k-1) (p_0)^{k-2} p_1 p_3 + \frac{k(k-1)}{2} (p_0)^{k-2} (p_2)^2 + k (p_0)^{k-1} p_4, \end{aligned} \tag{A.10}$$

$$\begin{aligned} P_5(\tau) = & \frac{k(k-1)(k-2)(k-3)(k-4)}{120} (p_0)^{k-5} (p_1)^5 \\ & + \frac{k(k-1)(k-2)(k-3)}{6} (p_0)^{k-4} (p_1)^3 p_2 + \frac{k(k-1)(k-2)}{2} (p_0)^{k-3} (p_1)^2 p_3 \\ & + \frac{k(k-1)(k-2)}{2} (p_0)^{k-3} p_1 (p_2)^2 + k(k-1) (p_0)^{k-2} p_2 p_3 \\ & + k(k-1) (p_0)^{k-2} p_1 p_4 + k (p_0)^{k-1} p_5. \end{aligned} \tag{A.11}$$

Assuming coarse-grained timescale in the numerical simulation with a step size of $\Delta t = \tau/100$ and hence $k = 100$, and a value for the product of interaction time and atomic rate of $r\tau = 1.0$, the probability of more than

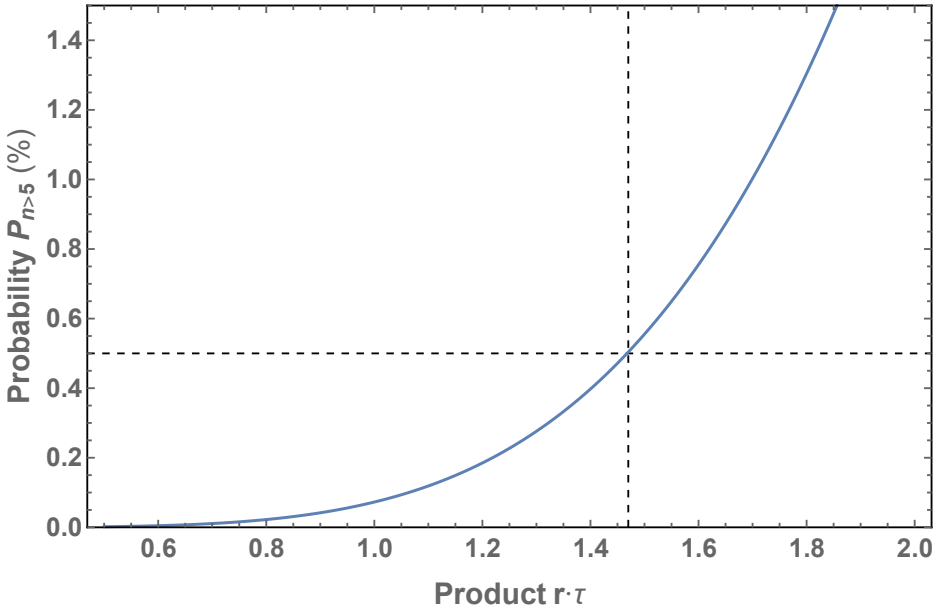

Figure A.1: The dependence of the probability of more than five atoms interacting with the resonator at the same time on the product of $r \cdot \tau$. The dashed lines indicate the maximum value of the product $r \cdot \tau$ for which the error is $\epsilon \leq 0.5\%$.

five atoms interacting with the resonator at the same time is

$$P_{n>5} = 1 - P_{n\leq 5}, \tag{A.12}$$

where

$$P_{n\leq 5} = \sum_{n=0}^{5} P_n(\tau). \tag{A.13}$$

This leads to the result that

$$P_{n>5} \approx 0.07\% \tag{A.14}$$

and validates the assumption to consider at most $n = 5$ atoms interacting with the resonator at any given time. It becomes clear that the validity of the truncation depends on the maximum atomic rate, r, and on the interaction

time, $\tau = k\Delta t$. The dependence of the error of the approximation on the atomic rate, r, is plotted in Fig. A.1, and can be seen to be below $\epsilon \lesssim 0.5\%$ for $r\tau \lesssim 1.45$, which in theory is the limit for the atom rate of this specific numerical truncation. For a chosen interaction time of $\tau = 50$ ns, the maximum atomic rate is calculated to be $r = 29$ MHz, and for an interaction time of $\tau = 10$ ns, the maximum atomic would then be $r = 145$ MHz. Hence, the parameters for the calculations carried out in Chapter 6 are all within this limit.